Development of Titanium Diboride Wettable Cathodes for Aluminium Electrolysis by Suspension Plasma Spray

Alexandre Bily

A Thesis

In the Department

Of

Mechanical, Industrial and Aerospace Engineering

Presented in Partial Fulfilment of the Requirements

For the Degree of

Doctor of Philosophy (Mechanical Engineering) at

Concordia University

Montréal, Québec,

Canada

May 2023

Signature

CONCORDIA UNIVERSITY

School of Graduate Studies

This is to certify that the thesis prepared

By: *Alexandre Bily*

Entitled: *Development of Titanium Diboride Wettable Cathodes for Aluminium Electrolysis by Suspension Plasma Spray*

Date of examination: 04/05/2023
And submitted in partial fulfilment of the requirements for the degree of

Doctor of Philosophy (Mechanical Engineering)

Complies with the regulations of the University and meets the accepted standards with respect to originality and quality.

Signed by the final Examining Committee:

_____

Dr. Xiao Huang

_____

Dr. Rolf Wuthrich

_____

Dr. Mehdi Hojjati

_____

Dr. Martin Pugh

_____*Thesis Co-supervisor*

Dr. Christian Moreau

_____*Thesis Co-Supervisor*

Dr. Ali Dolatabadi

Approved by: _____

Dr. Muthukumaran Packirisamy, Graduate Program Director

04/05/2023 _____

Dr.Mourad Debbabi, Dean

Gina Cody School of Engineering and Computer Science

Abstract

Development of Titanium Diboride Wettable Cathodes for Aluminium Electrolysis by Suspension Plasma Spray

Alexandre Bily, PhD

Concordia University, 2023

Aluminium is one of the most widely used materials across the world. Its elaboration process, based on the Hall-Héroult electrolysis process, has an energetic efficiency too low for such an important industry. In this research work, we worked upon the elaboration of wettable cathodes, meaning cathodes with a high molten aluminium wettability, in order to decrease the energetic cost of the process, as well as its environmental impact. These cathodes are based on a titanium diboride coating. In our studies, and for the very first time in history, these coatings were elaborated by suspension plasma spray.

High quality coatings with a very low degree of oxidation were produced by suspension plasma spraying coupled with a gas shroud to protect the in-flight particles from oxidation. Such an approach made it possible to significantly improve the deposited coatings as compared to the coatings from the literature deposited with atmospheric plasma spraying. Then, parametric studies led progressively to an increase in the percentage of molten particles, and, consecutively, an increase in the coatings' density. This increased density came along with augmented thermomechanical strains, leading to fracture and delamination. A multilayer approach, as well as a refined control of the cooling of the samples after deposition, allowed for the mitigation of the stresses and led to dense un-oxidized coatings. These coatings have shown a very high aluminium wettability, better than the one of the cathodes currently in use today.

Acknowledgments

I would like to start by thanking my fellow students, as well as the research professionals and technicians I worked with, for their precious help and advice during the time of my PhD: Fadhel, Mazen, Gilles, Saeed, Étienne, Vahid, Saeed, Ali.

Thank you to my supervisors for working with me during these past five years, for their help and continuous support. Thank you, Dr. Moreau. Thank you, Dr. Dolatabadi.

I also want to thank my Nearu family. Martial art helped me to be steady in my work, and to keep a healthy lifestyle, especially during the pandemic. Thank you Babak, Ali, Alireza, Avia, Fedra, Reza, Amir, Nihatha.

I want to especially thank my closest friends and my flatmates, for welcoming me in Québec, making it my home, and helping me go through the ups and downs involved in research: Nico, Sophie, Sylvie, Robin, Louise, Émile, Gauvin, Sandrine, Camille, Gabriel, Médérick, Bastien, Olivier, Andy, Alex, Sam, Anabelle, Beau-lac, Chevy.

Thanks also to my friends who already had their PhD and helped me keep going during the hardships one encounters in such an adventure: Zélie, Pauline

Finally, I want to thank my family and especially, my parents. I know you don't understand fully what I have been doing during all those years, and you wished I had finished my years of university earlier, but I also know you have a certain pride in your son becoming a doctor. And it fills my soul with joy.

Table of contents

List of Figures

List of Tables

List of Abbreviations and symbols

Abbreviation	*Meaning (unit)*
1SLD, 2SLD	1-Step Laser Deposition, 2-Step Laser Deposition
ACD	Anode-Cathode Distance
AHF	Ability of Heating Factor
APS	Atmospheric Plasma Spray
BSE	Back-Scattered Electrons
CR	Cryolite Ratio
DE	Deposition Efficiency
DMF	Difficulty of Melting Factor
GHG	Green House Gases
MHD	MagnetoHydroDynamics
PVP	PolyVinylPyrrolidone
SEM	Scanning Electron Microscopy
SPS	Suspension Plasma Spray
TEC	Thermal Expansion Coefficient
VPS	Vacuum Plasma Spray
XPS	X-ray PhotoSpectroscopy
XRD	X-Ray Diffractometer

Chapter 1 Introduction

1.1. Introduction

From our kitchens to the final frontier, aluminium is present at every stage of human technology. As such, it is one of the most widely used metals in the world. However, it was not always the case: until 1887, aluminium was a precious metal, used only for jewellery or high-end technologies. This is due to the stability of alumina and the difficulty to reduce it into aluminium. Ironically, this passivating alumina layer is one of the reasons why aluminium is widely used today. In 1887, the American Hall [1] and the French Héroult [2] independently invented the process that carries their names and is still the backbone of the production of aluminium today.

After this discovery, aluminium became increasingly used, decade after decade. Today, aluminium production is still growing rapidly, with China being the top producer and having the most recent facilities overall. Canada is the fourth-largest producer, with 11 aluminium smelters and one refinery, most of them located in Québec, in the Saguenay-Lac-Saint-Jean, Montérégie, Côte-Nord, Centre-du-Québec and Capitale-Nationale regions, the rest in British Columbia [3]. It is one of the main industries in those regions, providing directly more than 7,500 jobs [4] in Québec, over 9,000 across Canada, and indirectly supporting more than 30,000 jobs nationwide.

In the past decades, as well as in the future ones, environmental issues are becoming the core socio-political concern of the planet. If humanity is to survive and thrive, it must significantly reduce its greenhouse gas emissions. The speeches at international conventions such as the various United Nations Climate Change conferences, as well as the mass demonstrations and societal changes unfolding, are signs of this evolution. However, it must also manifest itself through technological changes, reducing the environmental impact of industrial processes. Aluminium production was responsible for 1% of worldwide greenhouse gas emissions at the beginning of the millennium. It may not seem like much, but it represents hundreds of megatons of CO_2. All these environmental concerns should also be linked to the growth of the industry. Since China's entry into the aluminium market in 1999, global aluminium production has been constantly increasing, as shown in Figure 1-1 below.

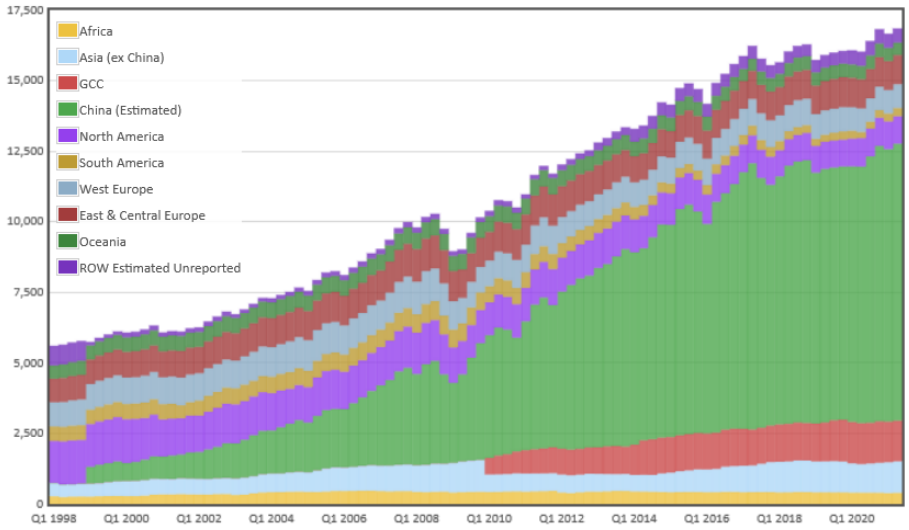

Figure 1-1 World aluminium production from 1998 to 2021, in metric kT of aluminium [3].

This global aluminium production mainly consists of four significant steps:

- Mining of the bauxite ore

Bauxite is the richest alumina-containing ore and is the primary source for extracting aluminium worldwide. It typically has an orange shade, as shown in Figure 1-2. Bauxite is formed through the weathering of soil, caused by heavy precipitation and temperature changes, resulting in a higher concentration of iron hydroxide and aluminium hydroxide. It is mostly found in regions with a tropical climate or regions that previously had a tropical climate. Depending on the original rocks from which it is derived, bauxite can be classified as lateritic or karstic ore [5]. The main bauxite mines in the world are located in Australia, China, Brazil, Indonesia, and Guinea. Since Canada does not have any bauxite mines, most of the bauxite ore is transported to its smelters via cargo ships which are a common sight in Saguenay, where five smelters and a refinery are located.

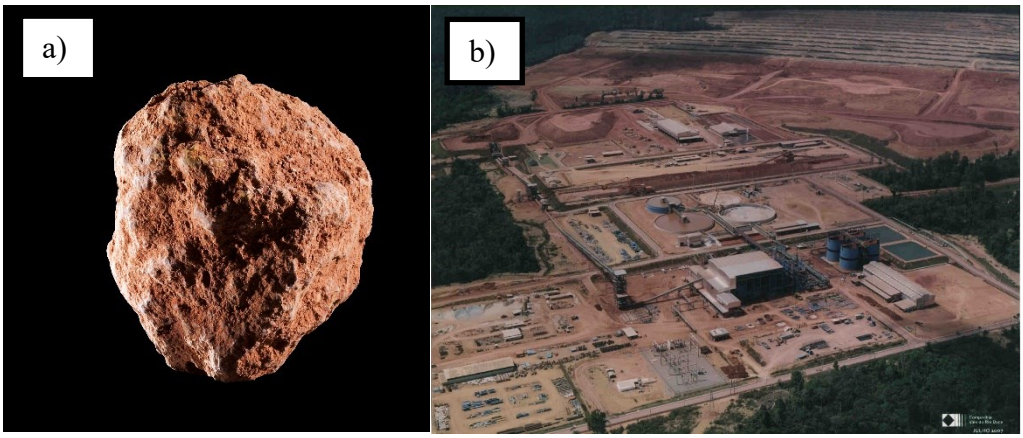

Figure 1-2 Bauxite ore (a) and Bauxite mine in Paragominas, Brazil (b) [3].

- The Bayer process

After mining, bauxite ore needs to be crushed and dissolved to extract alumina and remove other minerals. The ore is typically crushed in two steps, first by a jaw crusher and then by an impact crusher. It can then be further ground through milling.

Once the ore is prepared, it undergoes the Bayer process to refine the alumina. After grinding the bauxite, a caustic soda solution is added to dissolve the minerals in a pressure vessel at 200 °C. The other main minerals removed in this step, the secondary minerals of bauxite, include silica, iron oxide, titania, and calcium oxide. The amount of each mineral depends on the ore's environment, with significant differences between karstic and lateritic bauxite (lateritic bauxite being more suitable for mining). The dissolution reactions involved are as follows:

$Al_2O_3 + 2\ NaOH \rightarrow 2\ NaAlO_2 + H_2O$ and $2\ NaOH + SiO_2 \rightarrow Na_2SiO_3 + H_2O$

The mixture then undergoes a desludging process to remove impurities and the leftover NaOH, resulting in a mixture called red sludge. Proper storage of the red sludge is essential as it is a chemical waste that can harm the environment, as shown in Figure 1-3. Filtration and evaporation steps are performed to purify the mixture, followed by a calcination step to transform the aluminium hydroxides into alumina. Stationary calciners, such as circulating fluidized beds, gas suspension calciners, or fluid flash calciners, are commonly used for this purpose.

Figure 1-3 Bauxite residue disposal area in Aughinish, Ireland [3].

- The Hall-Héroult Process

Once alumina has been refined, it is crushed and dissolved into a solution of cryolite, which serves as the electrolyte in an electrolysis cell. As mentioned earlier, alumina is highly stable, requiring a significant amount of energy for the reaction to occur. The main mechanism is described in Figure 1-4 below. The main reactions occurring at each electrode are as follows:

Anode: $C_{(s)} + 2O^{2-}_{(aq)} \rightarrow CO_{2(g)} + 4e^-$ and $C_{(s)} + O^{2-}_{(aq)} \rightarrow CO_{(g)} + 2e^-$

Cathode: $Al^{3+}_{(l)} + 3e^- \rightarrow Al_{(l)}$

To minimize energy loss through heat dissipation, the cell is surrounded by several layers of refractory bricks. The choice of the electrolyte is designed to reduce the melting point of alumina from 2000 °C to 950-980°C, thereby lowering the operation temperature of the cell. The electrolyte is mostly composed of cryolite (Na_3AlF_6) mixed with various fluorides such as AlF_3, CaF_2, MgF_2, LiF, KF [6]. This temperature is kept at a minimum to reduce energy loss through heat dissipation. Additionally, the cryolite solidifies on the edges, sides, and top of the cell, further aiding in reducing energy loss by acting as an insulating layer.

Secondary reactions occur at both the anode and cathode, leading to the formation of gases more detrimental to the environment than carbon dioxide, such as carbon monoxide (CO) and perfluorocarbons (CF_4 and C_2F_6). The amount of greenhouse gases emitted through these reactions depends on various factors, including cell voltage, design, alumina content in the bath and moisture of the alumina.

The core step in refining alumina into aluminium in this entire process is electrolysis, known as the Hall-Héroult process. The Hall-Héroult process is the electrolysis of alumina into aluminium. It was discovered in 1887 by the British scientist Hall and the French scientist Héroult and remains the backbone of aluminium production to this day.

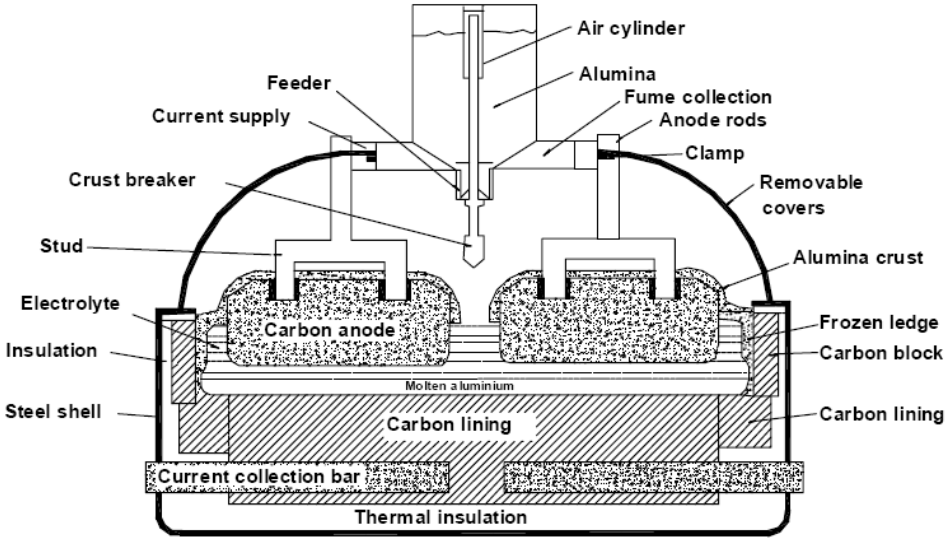

Figure 1-4 Schematic of a typical Hall-Héroult cell for electrolytic smelting of aluminium [7].

The prepared alumina powder is continuously injected from the top into the cell using a feeder, and the rate of supply of alumina must be accurately controlled to maintain optimal reaction conditions. The anode consists of a prebaked consumable graphite rod, while the cathode is the carbon-lined bottom of the cell. The electrolyte is specifically designed to lower the operating temperature of the cell by reducing the melting point of aluminum to a range close to 960 °C. It is composed mainly of cryolite which has a solidifying temperature slightly above this range, causing the top and edges of the electrolyte to freeze. The cell is surrounded

by several layers of insulation to reduce heat loss during operation. At the anode, gases such as CO_2 and CO are formed, while molten aluminium is produced at the cathode and then extracted from the cell. The extraction point is one of the main areas of cathode erosion due to edge effects. The typical Hall-Héroult reduction pot or cell shown in Figure 1-4 is a rectangular steel structure measuring 10 meters long, 3.5 meters wide, and 1.5 meters deep [8].

As the industry grows, greenhouse gas emissions become increasingly impactful, highlighting the importance of addressing these issues and their economic impacts [9]. Furthermore, the efficiency of the aluminium fabrication process itself can be improved. It is essential to differentiate between two types of efficiencies in the Hall-Héroult process. Current efficiency corresponds to the ratio between the actual amount of metal produced by electrolysis and the theoretical amount predicted by Faraday's laws of electrolysis. In modern cells, current efficiency ranges from 90% to 95%. On the other hand, energy efficiency corresponds to the ratio between the energy used for metal production and the total energy consumed. In modern cells, the process requires 13-14 kWh per kilogram of aluminium, as detailed in Figure 2-1 in the following chapter, with approximately 50% of this energy dissipated as heat, resulting in an energy efficiency of around 50%.

Due to the extreme stability of alumina, electrolysis requires a high amount of energy. Additionally, several factors contribute to low energy efficiency, typically ranging from 50% to 55%. One of these factors is the electronic loss in the electrolyte due to the anode-cathode distance. The pool of molten aluminium at the bottom of the cell, in the range of 3-25 cm, represents a significant portion of this cathode-anode distance and is regularly siphoned out of the cell into external crucibles. One of the main approaches to reduce this distance is the development of so-called wettable cathodes, which have a high affinity for molten aluminium. The currently used carbon-lining cathodes do not have good wetting properties with aluminium, exhibiting a high contact angle above 50°. Higher wetting properties would result in a more stable state with lower energy for the cathode-molten aluminum system. By using a cathode with high molten aluminium wettability, the required thickness for the pool of molten aluminium could be reduced by 50% without increasing degradation mechanisms of the cathode, such as sodium penetration and aluminium carbide formation.

1.2. Project Motivations

As illustrated in Figure 1-5, based on the process description, the main environmental impacts [10] [11] [12] [13] can be listed as follows:

1. Transport: This refers to the environmental cost associated with transporting the raw materials
2. Thermal Energy: The dissipation of thermal energy during the process due to heat

3. Ancillary Materials: The treatment of red sludge to prevent chemical pollution
4. Direct Process: CO_2 emissions from consumable anodes, which need replacement every two weeks to a month
5. Electricity: The environmental impact of the electricity source used for the process. For instance, countries like Australia, mostly relying on coal, have a higher impact compared to Canada, which uses hydroelectricity. [14]

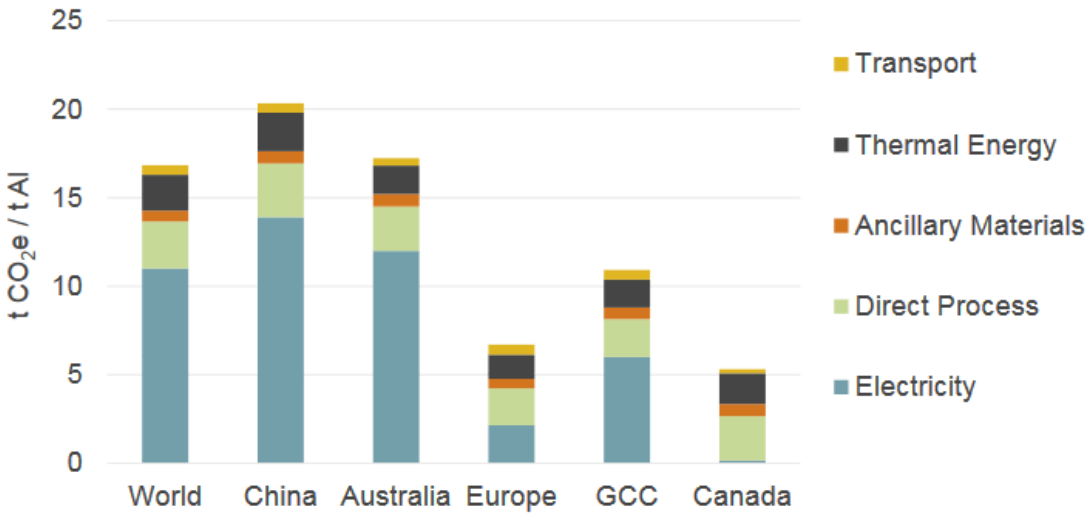

Figure 1-5 Carbon footprint of primary aluminium, for various parts of the world and with attributed causes of CO_2 production [3].

The first issue can be addressed by establishing smelters and refineries on the site, close to the bauxite mines. In many cases, this means there is a need to install new facilities and develop the power grid in concordance, as such factories are highly demanding energy-wise. This plan would demand a very long-term approach to be put in place.

The second issue, the thermal dissipation, can be dealt with by improvements in the insulation of the process, as well as in its efficiency. With a more energetically efficient process, there will be less heat dissipation.

The third issue requires a strict control of the chemical waste, and a significant improvement in the research associated with the treatment of such wastes, to avoid the criminal act of dumping those wastes in protected natural reserves, as has been the case in other industries for similar wastes in the past decades.

The fourth issue can be addressed by replacing the consumable anode by an inert anode. With the currently used consumable anodes, the production of one ton of aluminium metal consumes 437 kg of carbon anodes [11]. Furthermore, that would reduce the risks associated with replacing the anode on a biweekly basis. The replacement of the anodes is a risky operation for the workers when the old anode is being removed. Indeed, if a drop of water falls into the cryolite, it leads to an explosive reaction, which won't damage the cell severely,

but might wound the workers. As such, reducing the frequency at which those electrodes are replaced will improve the working conditions of the workers at the smelter. Inert anodes have been the object of intensive research as discussed in [15] and [16]. For example, it has been proposed to manufacture inert metallic anodes protected by a CoO-NiO coating, deposited by an electrochemical process or by thermal spraying, either HVOF or plasma spraying [17] [18]. On this front, a big step is already on its way [19], with the construction by Elysis, a joint venture of Alcoa and Rio Tinto, of a factory to produce and commercialize inert anodes and the according cells with a possibility to retrofit them in previous smelters [20], which should arrive on the market in 2024, leading to a great reduction in greenhouse gas emissions, and improved productivity.

The fifth issue is intricately connected with the fourth one. Indeed, replacing consumable anodes with inert ones comes with a requirement to redesign the cell with vertical anodes and cathodes. However, in the current generation of smelters, there is a need to keep a pool of molten aluminium of 4 cm to 6 cm to increase the life of the cathode, as detailed in Literature ReviewChapter 2. Without such a pool, the current passing through the molten metal creates magnetohydrodynamic currents, which can expose the cathode directly to the electrolyte. This leads to penetration of fluoride into the graphite-lining cathodes which leads to deformation and cracks, which is one of the main deterioration mechanisms of the cathodes. One way to address this issue is to reduce the surface energy between the molten aluminium and the cathode's surface, which means to increase the aluminium wettability of the cathode. By increasing the aluminium wettability of the cathode, one can decrease the minimum thickness of this aluminium pool, therefore reducing the anode to cathode distance meaning that the cell can run on a smaller power for the same output of molten aluminium. This fact is also very interesting as the currently developed inert anodes frequently require higher voltages compared to the inert ones to produce the same amount of aluminium. By combining inert anodes and wettable cathodes, these two factors would cancel each other [21]. Other ways to improve the cells are to redesign it, such as using perforated electrodes or multi-electrodes approach [22] [23].

The focus of this work is on developing of those wettable cathodes using Suspension Plasma Spray to deposit Titanium Diboride on graphite and assessing the quality of these coated wettable cathodes. The choice of materials and techniques is explained in detail in Chapter 2 and Chapter 3.

1.3. Objectives of the work

Stemming from industrial requirements and state-of-the-art technology, the main objectives of the research described in this thesis are as follows:

The primary objective is the development of mechanically stable unoxidized titanium diboride coatings with the capability to wet aluminium using suspension plasma spray. These coatings must be designed to be impermeable to molten aluminium, enabling their testing in an electrolysis cell.

A secondary objective is to enhance the coating quality in terms of composition by employing techniques to minimize oxidation to a level that does not adversely affect the application.

Another secondary objective is to investigate the relationship between the microstructure of the coatings and their wettability properties. This investigation aims to develop a process that allows for easy control and repair of wettable cathodes.

A third secondary objective is to assess the feasibility of treating the TiB_2 coatings with a high-power laser to achieve complete densification. Such post-treatment of coatings is becoming increasingly available on an industrial scale as high-power lasers are more commonly used in the growing additive manufacturing industry.

1.4. Thesis structure

This thesis is presented in six chapters. The first chapter provides a general introduction to the thesis and explains the problem addressed and the project's objectives.

In the second chapter, an extensive literature review is presented, covering in-depth knowledge of primary aluminium production and the Hall-Héroult process. It highlights the current issues with carbon-lining cathodes that are currently used. The chapter then delves into wettable cathodes, their production methods, material selection, and the challenges associated with their development. It particularly focuses on the plasma spray process for creating wettable cathodes, reviews prior work on plasma sprayed TiB_2 coatings, and discusses the current limitations of this approach.

Chapter 3 provides a more detailed outline of the experimental setup and methodology used in the project. It covers the starting materials, experimental parameters, and characterization tools employed. The chapter explains the planning of the experiments and the procedures followed to obtain the results represented in the subsequent chapters.

Chapter 4 contains the bulk of the results obtained. It begins with the initial steps of the feasibility study. As TiB_2 had never been deposited by Suspension Plasma Spray before, the first goal was to achieve this and deposit mechanically stable TiB_2 coatings. The chapter provides an overview of this process. Additionally, it addresses the issue of oxidation by using a gas shroud to protect in-flight particles from oxidation. Furthermore, the chapter explores the influence of plasma composition, power, feed rate and suspension load on the density of the coatings. Finally, the chapter considers the physical processes during the

elaboration, leading to a study on a porous / dense multilayer approach to address the fracture issue arising from the densification process.

Chapter 5 covers a post-treatment of the coatings, 2-Step Laser Deposition, using a Laser to remelt the top layers of the plasma-sprayed TiB_2 coatings to achieve densification. This preliminary study sets a precedent for further research, and while the results displayed in the chapter are promising, they also reveal some mechanical issues and challenges of repeatability.

In chapter 6, the conclusions of the thesis are drawn and summarized. The main contributions of this work are detailed, and prospects for further progress are suggested, with the list of potential research directions.

Chapter 2 Literature Review

2.1. Current Cathodes in the Hall-Héroult Process

Over the past 136 years, the Hall-Héroult process has remained both familiar and completely new. Its main principles and elements have endured, but through more than a century of research and development, these components have evolved significantly, resulting in a more efficient and robust process [24].

2.1.1. History and Development

As depicted in the graph below (Figure 2-1), the average energy consumption of aluminium smelters has significantly decreased over the past four decades worldwide. One of the driving factors behind this trend has been the evolution of cathode technology. The lower consumption in Chinese smelters can be attributed to their more recent installations as well as improvements correlated to the scale of these new installations and the increases in publications and research in the field of aluminium.

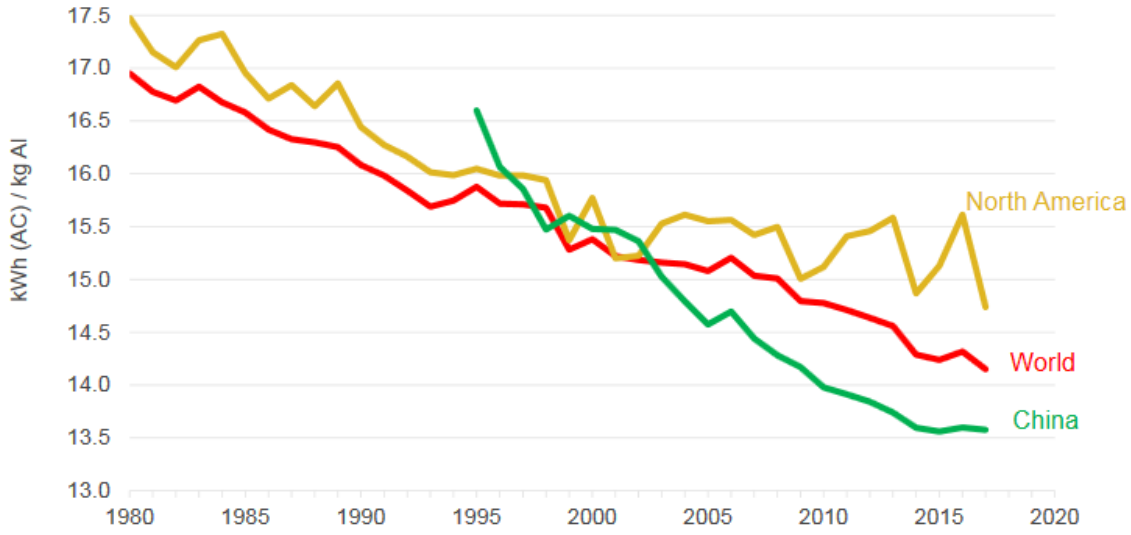

Figure 2-1 Evolution of Hall-Héroult industrial cell electrolytic energy intensity 1980-2018 [25].

The generations of cathodes currently in use in the industry are primarily carbon-lining cathodes. They are produced by mixing dry carbon aggregates such as anthracite, graphite, or petroleum coke with a binder, typically coal tar pitch. These graphite-based cathodes are mechanically stable at the high temperatures required for their operation [26]. A significant technological advancement in recent decades has been the transition from anthracitic cathodes to semi-graphitic, graphitic, and eventually graphitized cathodes, reducing the electrical

resistivity of the cathode by five times [27]. The key difference between these generations of cathodes lies in the high temperature treatment at 3000 °C for graphitized cathodes, compared to 1000 °C for the previous anthracitic generation. The overall trend in cathode development has been aimed at decreasing their resistivity, achieved through increasing the graphite-to-anthracite ratio, enhancing the carbon planes' order through heat treatments [27], and utilizing the Joule effect in a graphitizing furnace to heat the cathode blocks. Other techniques are also being explored to further increase the cathodes' lifespan, such as introducing lithium into the surface layer of the graphite lining to form intercalated compounds, which act as a diffusion barrier [28]. Initially, this led to a loss in wear resistance, but it was eventually overcome.

Combining these technological improvements with automation [29] [30] and increased cell size and amperage, we arrived at today's generation of cathodes. As the cathode forms the bottom of the cell, its replacement requires the disassembly of the entire cell, making the cathode life a determining factor in the cell's lifespan, which can be up to 2000 days [31].

2.1.2. Issues with current cathodes and wear mechanisms

Figure 2-2 illustrates the various voltage drops occurring across the cell, highlighting the areas where most of the energy is wasted and does not directly contribute to the electrochemical reaction. As shown in the figure below, there is a voltage drop at the cathode due to its resistivity, which is 0.45 V, accounting for 9.8% of the total cell voltage. It is crucial to prevent this from increasing, which means maintaining the electrical conductivity of the cathode. The main components of this energy consumption are the reaction, the bath, and the polarization. The potential drop corresponding to the reaction is minimal, with a value of 1.2 V at 960 °C. The polarization accounts for the need to overcome energy barriers, such as the accumulation of gases at the anode, and is around 0.6 V, or 13% of the total voltage. However, the electrolyte bath is the primary energy consumer, with the molten aluminium pad and the size of the bath dissipating a significant amount of energy in the form of heat, resulting in a voltage drop of 1.75 V, or 38%. This value is directly related to the Anode-Cathode Distance (ACD), where a shorter ACD means a shorter electronic pathway from the anode to the cathode. Most of this energy loss is dissipated as heat, resulting in an energy efficiency of only 50%. Improving the energetic efficiency of the cell involves decreasing the ACD.

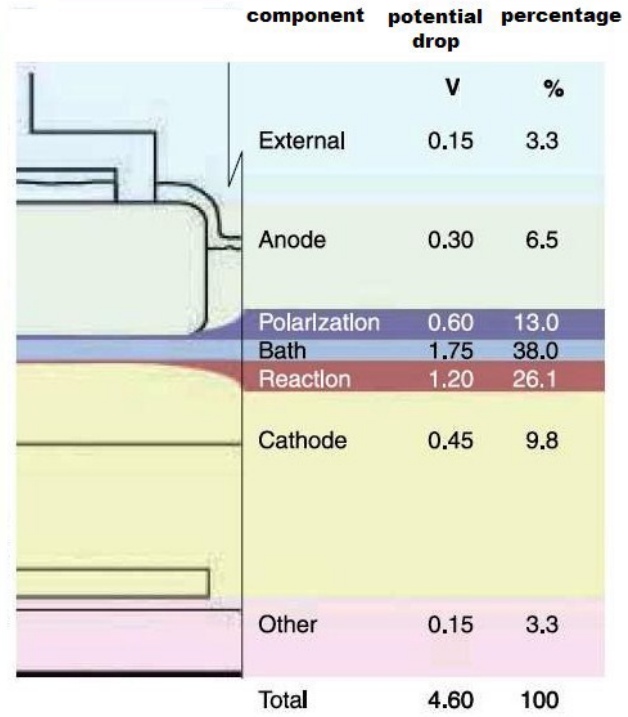

Figure 2-2 Voltage distribution in a Hall- Héroult cell [32].

The nominal values for the ACD are related to the wear mechanisms of the cathode and Magneto-Hydrodynamics (MHD) effects. The two current wear mechanisms for the cathode are:

- The formation of aluminium carbide through this reaction:
  $4Al + 3\ C \rightarrow Al_4C_3$
  The molten aluminium reacts with the carbon in the cathode lining, leading to the formation of aluminium carbide, which causes debonding and accelerated mechanical fractures [33].
- The penetration of the electrolyte
  $Al_{(l)} + 3NaF_{(\text{in electrolytes})} \rightarrow 3\ Na_{(\text{in cathode})} + AlF_{3(\text{in electrolytes})}$
  The electrolyte is generally composed of a ratio of NaF/AlF_3, referred to as the Cryolite Ratio (CR) in reference to Na_3AlF_6. This CR value typically ranges between two and three in the industry [6]. The sodium present in the electrolyte reacts with the molten aluminium on top of the cathode, infiltrating the carbon cathode, as indicated in the chemical reaction above.

As the penetration of sodium into the carbon cathode increases, it leads to mechanical failures due to swelling and crack propagation. The area where these phenomena are most severe is the region where the crust of the cryolite must be broken to remove the aluminium from the Hall-Héroult cell. This creates sharp roughness and turbulence in the electrolyte, thereby increasing the number of secondary reactions in the region and building up of stresses. To limit the penetration of the electrolyte into the cathode, the pool of molten aluminium is kept between 20 cm and 25 cm. This prevents MHD effects from causing waves that could lead to

direct contact between the cryolite and the cathode, which would increase the activity of the reaction. Consequently, the pool of molten aluminium acts as the effective cathode in the process, and the ACD distance being at this point the distance between the anode and the aluminium pad.

As a high current runs through the pad of liquid aluminium, magnetic forces induce movement and waves in the liquid metal [34]. Addressing these MHD effects is crucial to decrease the ACD [35]. To prevent these waves from causing a shortcut by putting the anode in contact with metallic aluminium, the ACD is generally maintained at 4-5 cm. Due to this ACD, an ohmic drop occurs, and the voltage applied to the cell has to be increased accordingly, as detailed in Figure 2-2.

By replacing the carbon lining cathodes with new materials that have increased aluminium wettability, the ACD could be halved to 2-2,5 cm, and the thickness of the pool of molten aluminium could be reduced as well. This would lead to a significant reduction in the voltage drop in the bath, thereby increasing the energetic efficiency of the process.

2.2. Wettable Cathodes

Along with inert anodes and the redesigning of Hall-Héroult cells, research and development efforts to further improve the efficiency of aluminium smelting have focused on developing more robust cathodes and cathodes with improved wettability, with the main goal of developing a wettable drained cathode cell. The concept of such a cell is to continuously drain the molten aluminium while maintaining a thin layer on the cathode, which would act as the real cathode and prevent direct contact between the cathode and the cryolite.

2.2.1. Physics of Wettability

Wettability is a generalization of the more familiar concept of hydrophilic/hydrophobic behaviours of materials to any liquid. It describes the affinity between a solid and a specific liquid. In the case of water, it is called hydrophilic if there is a high affinity and hydrophobic if there is a low affinity. But what does this affinity mean? As is often the case in physics, it boils down to the state of lower energy.

In Figure 2-3a below, a droplet of liquid is deposited on a solid surface. The contact angle θ, the parameter of wettability, is related to the surface tensions γ_{LA} (Liquid/Atmosphere), γ_{SL} (Solid/Liquid) and γ_{SA} (Solid/Atmosphere) via Young's equation [36]: $\cos\theta = \frac{\gamma_{SA}-\gamma_{SL}}{\gamma_{LA}}$. Thereby, for an ideal liquid on a smooth surface, the contact angle of a liquid depends on the various surface tensions involved and as thus on the surface chemistry of the materials involved (the solid, the liquid, and the atmosphere considered). But another important factor that influences wettability is the microstructure and nanostructure of the solid. The topography of the solid can result in two different wetting regimes. In Figure 2-3b, the homogeneous regime, or Wenzel regime [37] is represented, where the liquid/solid interface is continuous, and Young's equation is simply modified by a rugosity factor r: $\cos\theta_c = r \cdot \cos\theta$. In this regime, the wetting behaviour is enhanced: a wetting liquid will spread even

more, and a non-wetting liquid will spread even less on the rougher solid. In Figure 2-3c, the heterogeneous regime, or Cassie-Baxter regime [38], is represented, where the liquid/solid interface is not continuous: typically, capillary forces maintain pockets of air within the profile of the solid interface with significant roughness. In this case, the fraction ϕ_{LA} of the total contact area between liquid and atmosphere must be considered, and Young's equation is modified as such: $\cos\theta_c = r \cdot \cos\theta - \varphi_{LA} \cdot (1 + \mathrm{r} \cdot \cos\theta)$. In this regime, the pockets of air will reduce the wettability of the liquid in all cases, for both wettable and non-wettable solids. In our research, as we are looking for high wettability, we aim to reach a Wenzel regime, not a Cassie-Baxter one. To conclude, we can say that both the surface chemistry and the surface morphology are key parameters determining the static and dynamic wettability of a material by a liquid.

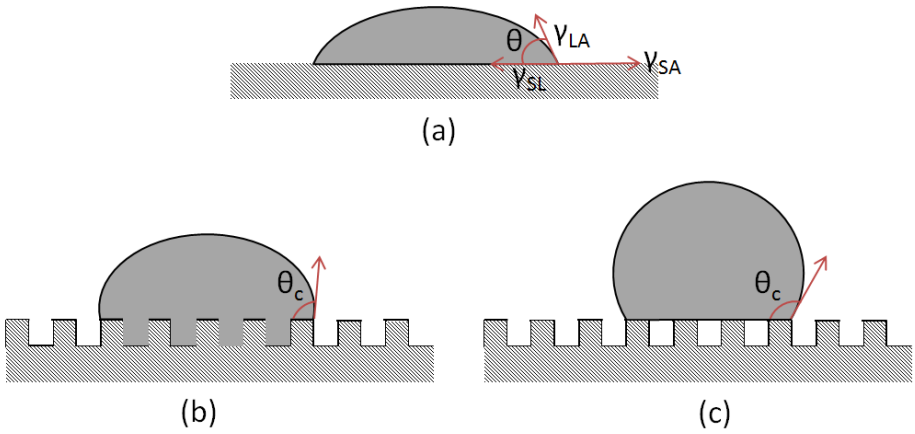

Figure 2-3 Schematic of (a) a wettable surface, (b) Wenzel wetting regime and (c) Cassie-Baxter wetting regime.

2.2.2. Criteria for Wettable Cathodes

To develop wettable cathodes, the selection of materials is limited due to the specific criteria that must be met. In addition to high aluminium wettability, cathode materials must also possess high electrical conductivity to function effectively in the harsh and corrosive environment of the Hall-Héroult cell [39]. The ideal cathode material should have low solubility with molten aluminium at 960 °C, good resistance to penetration by sodium and corrosion by molten electrolytes, adequate mechanical strength to withstand thermal and chemically induced cracking, resistance to erosion, and reliable electrical contact with current collectors.

Considering these stringent requirements, only a few materials meet the criteria including borides and carbides such as TiB_2, ZrB_2, TiC, B_4C, SiC, and ZrC [40], as illustrated in Table 2-1 below. Among these options, TiB_2 emerges as the main candidate due to its favorable characteristics and compromises. Notably, titanium diboride is relatively cost-effective compared to other materials in the list, while possessing lower electrical resistivity than TiC or ZrC and lower solubility in molten aluminium [41] [42]. The lower solubility is

advantageous as it increases the cathode's lifespan. Over the past decades, significant research has been conducted on wettable cathodes based on titanium diboride [43], utilizing various production techniques such as sintering, electroplating, physical vapor deposition (PVD), and thermal spray processes [44] [45].

Compound*	Melting T °C	Density g.cm^{-3}	Electrical resistivity 25°C µΩcm	Electrical resistivity 1000°C µΩcm	Thermal conductivity Wm^{-1}K^{-1}	TEC K^{-1} 10^{8}	Elastic modulus 25°C GPa
TiB_2	2850-2980	4.52	9-15	60	24-59	4.6	253-550
ZrB_2	3000-3040	6.09-6.17	7-16.6	74	24	5.9	343-491
MoB_2	2100-2140	7.8-8.1	20-40				
B_4C	2450	2.52	2000-70000	High	29	4.5	448
TiC	3067-3250	4.92-4.95	51-250	119	17-21	5.5-7.74	269-462
WC	2600-2780	15.7-15.8	17-22	106-118	29-121	4.5	669-710
Si_3N_4	1870-1885	2.37-3.19	10^{19}	High		2.5	
AlN	2400 decomp.	3.25	High	High	30	5.6	345
BN	3000 decomp.	2.25-2.27	$1.7 \cdot 10^{18}$	High	15	7.5	
TiN	2950	5.39-5.44	21.7-53.9	130	17	9.35	
Graphite**	3500 subl.		570-1170			7.8	6.4-13.7

*: Commercial polycrystalline guide

**: Not RHM, but included for comparison

Table 2-1 Physical properties of some Refractory Hard Metals RHM [46].

2.3. Titanium diboride

2.3.1. Properties

Titanium diboride possesses the required properties [47] to be utilized as a material for a wettable cathode, as indicated in Table 2-2 below.

TiB_2 demonstrates excellent aluminium wettability, as observed in the literature [48]. Moreover, it exhibits electrical resistivity on par with the currently used cathodes , with a value of 3.4 µΩ.m at 1000K for dense polycrystalline TiB_2 [49] compared to 15 µΩ.m at 1000K for a graphitic cathode [27]. Its crystallographic structure is hexagonal close-packed, belonging to the space group P6/mmm with the following unit cell parameters: a=b=3.028 Å, c=3.228 Å, α=β=90°, γ=120°, resulting in a density of 4.52 g.cm^{-3}. The atomic structure of titanium diboride is the reason for its favorable properties, including excellent wear resistance, making it widely used for such applications [50], and high chemical resistance. Additionally, the strong covalent bonding between titanium and boron atoms contributes to its high melting point of 2980 °C. The TiB_2 phase exists over a stoichiometry range of 65.5- 67.0 at%B at ambient temperature, becoming smaller as the temperature increases, and it melts congruently, which is essential for the research being conducted here, as the process involves melting TiB_2 and re-solidifying it afterwards. For reference, the entire Ti-B binary phase diagram is shown in Figure 2-4 below.

Property	Temperature (°C)						
	20	500	1000	1200	1500	2000	u_r[a]
Bulk modulus (GPa)	240	234	228				24
Compressive strength (GPa)	1.8						?
Creep rate[b] (10^9 s^{-1})					0.005	3.1	20
Density[c] (g/cm^3)	4.5	4.449	4.389	4.363	4.322	4.248	0.07
Elastic modulus (GPa)	565	550	534				5
Flexural strength (MPa)	400	429	459	471	489		25
Fracture toughness (MPa $\cdot m^{1/2}$)	6.2						15
Friction coefficient[d]	0.9	0.9	0.6				15
Hardness (GPa)[e]	25	11	4.6				12
Lattice parameter[c] a/Å	3.029	3.039	3.052	3.057	3.066	3.082	0.03
Lattice parameter[c] c/ Å	3.229	3.244	3.262	3.269	3.281	3.303	0.04
Poisson's ratio	0.108	0.108	0.108				70
Shear modulus (GPa)	255	248	241				5
Sound velocity, longitudinal[f] (km/s)	11.4	11.3	11.2				5
Sound velocity, shear[f] (km/s)	7.53	7.47	7.40				3
Specific heat ($J \cdot kg^{-1} \cdot K^{-1}$)	617	1073	1186	1228	1291	1396	1.5
Thermal conductivity ($W \cdot m^{-1} \cdot K^{-1}$)	96	81	78.1	77.8			6
Thermal diffusivity ($cm^2 \cdot s^{-1}$)	0.30	0.17	0.149	0.147			6
Thermal expansion[c,g] α_a (10^{-6} K^{-1})	6.4	7.0	7.7	7.9	8.3	8.9	7
Thermal expansion[c,g] α_c (10^{-6} K^{-1})	9.2	9.8	10.4	10.6	11.0	11.6	5
Thermal expansion[g] α_m (10^{-6} K^{-1})	7.4	7.9	8.6	8.8	9.2	9.8	6
Wear coefficient[d] (10^{-3})	1.7						24
Weibull modulus[h]	11						?

[a] Relative standard uncertainty (%); ? means insufficient information to determine u_r

[b] Flexure creep rate at 100 MPa, ρ=4.29 g/cm^3, g=18 µm

[c] Single crystal

[d] ρ=4.32 g/cm^3, g=2µm, v_s/P_c=0.2 $m \cdot s^{-1} \cdot MPa^{-1}$

[e] Vickers hardness, load=5N

[f] $v_{shear}=(G/\rho)^{1/2}$; $v_{longitudinal}=((4/3)G/\rho+B/\rho)^{1/2}$

[g] Coefficient of thermal expansion $\alpha_x=(1/x_0)(x-x_0)/(T-T_0)$, x=a or c, cumulative from the reference state at 20°C (corresponding to T_0=293K); $\alpha_m=(2\alpha_a+\alpha_c)/3$

[h] Three reported values, 8, 11, and 29

Table 2-2 Mutually consistent trend values for properties of polycrystalline TiB_2 deduced from the collection of observed particular values for specimens having mass fraction of TiB_2 98%, rho = 4.5±0.1 $g.cm^{-3}$ and g= 9±1 µm, except as noted [47].

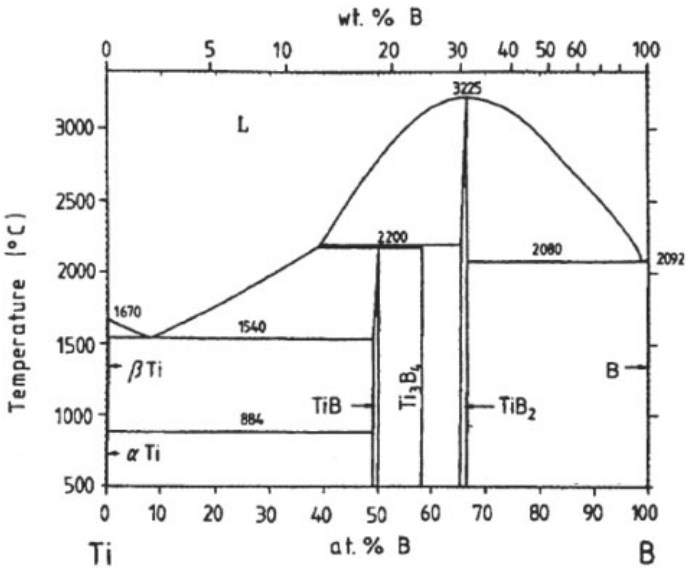

Figure 2-4 Binary Ti – B phase diagram [50].

2.3.2. Elaboration

Titanium diboride is produced using several high-temperature methods [51] [52] [53], and the chosen method determines the size distribution and morphology of the TiB_2 powder. Most of the properties we seek in titanium diboride – such as wear resistance and chemical stability - arise from the material's strong covalent bonds. However, it is precisely this strong covalent bond that makes the material challenging to produce and shape. One of the primary reaction routes to produce titanium diboride is the borothermic reaction:

$$2\ TiO_2 + B_4C + 3\ C \rightarrow 2\ TiB_2 + 4\ CO$$

However, this route does not allow for the development of nanocrystalline powder and obtaining powder with a size distribution in the 1-10 µm range is also challenging. Various other routes have been researched to obtain such fine powders, including the Self-propagating High-temperature Synthesis (SHS) process, mechanical alloying [54], and other reactions. In the specific case of using titanium diboride powder for suspension plasma spraying, the powder size distribution is in the micrometre to sub-micrometre range [55]. In our case, the manufacturers who provided the TiB_2 powder used the mechano-chemical reaction method. In this method, the powder is placed in a high-energy ball mill, and the powder is broken down to a smaller size distribution by the impact and shearing of the grinding ball. Compared to the SHS and carbothermal reduction methods, mechano-chemical reaction has the advantages of having a lower synthesis temperature and a relatively lower cost [56].

2.4. TiB_2-based cathodes

2.4.1. Sintering

Bulk TiB_2 cathodes were one of the earliest historical approaches [57] to establish wettable cathodes for aluminium electrolysis. A variety of sintering techniques have been used, including hot, cold, or pressureless sintering [58] [59] [60] as shown below.

In the Figure 2-5 below, Tallon et al. used a wet colloidal processing approach combined with pressureless sintering for densification. However, due to the low self-diffusion of titanium diboride, it has a poor sintering capability [50]. To overcome this issue, direct hot pressing followed by pressureless sintering [61], or cold pressing followed by high temperature sintering, are the preferred approaches. The cold pressing route is preferred because it has a lower cost and allows for more detailed net-shape fabrication.

Despite these efforts, there are significant challenges associated with using pure TiB_2 cathodes. These include the low sintering capability, high fabrication costs, brittle nature, poor thermal shock resistance, susceptibility to inter-granular corrosion by molten aluminium, and difficulties in retrofitting bulk TiB_2 cathodes into existing cells [62] [63].

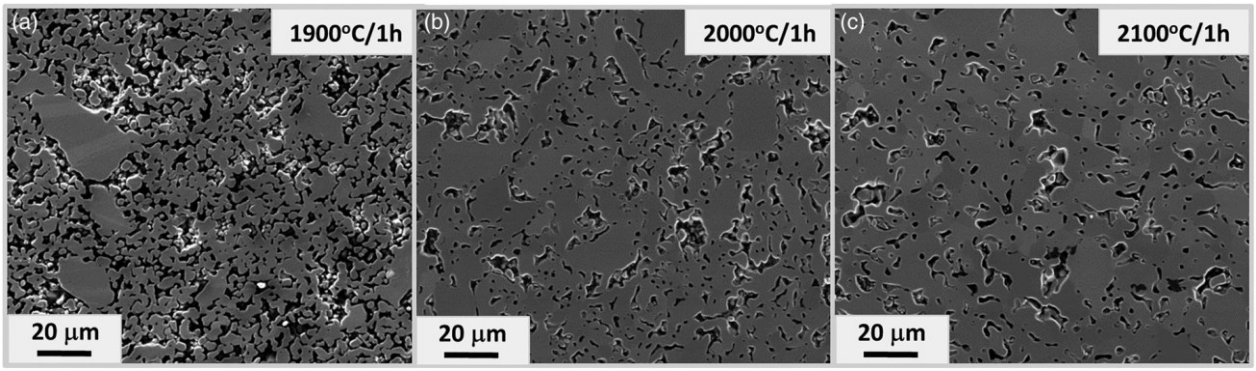

Figure 2-5 Microstructures of samples sintered in 1900 °C, 2000 °C, and 2100 °C [60].

Composite cathodes have also been explored, particularly the TiB_2-C composite route in the 1980s and 1990s. However, the results were not as promising as expected due to mechanical failure between the composite materials [64] [65] [66]. For instance, M.O. Ibrahiem et al. [67] conducted a deeper study on the impacts of the powder preparation process to create a TiB_2-C composite and showed that 50% of TiB_2 was enough to have good wetting properties and electrical conductivity. However, reactions occured through the open pores and grain boundaries, resulting in the formation of Al_4C_3 and Al_2O_3 in a matter of hours.

2.4.2. Additives

As discussed above, titanium diboride is challenging to format, to shape due to its very strong covalent bonding. In such cases, sintering additives can be used to improve the mechanical cohesion of sintered TiB_2 components. Various metallic or ceramic additives have been investigated for this purpose.

Metallic additives such as Fe, Ni, Cr, or Co enhance the densification of TiB_2 through liquid phase sintering, as they have good wetting properties on TiB_2 and adequate melting points to withstand the conditions in the Hall-Héroult cell. Eutectic reactions leading to the formation of borides, such as Fe_3B, act as a binding process for the TiB_2 grains [68]. However, these binder phases are brittle, which decreases the fracture toughness of the material. Moreover, they lead to exaggerated grain growth, resulting in spontaneous microcracking during the

cooling stage due to high thermal stresses building up among the large TiB_2 grains [69]. To counter this phenomenon, grain growth inhibitors such as TaB_2, W_5B_2 borides, WC or TiC carbides can be added [70].

Ceramic sinter additives can also be used to improve sinterability without degrading the mechanical properties of the coating, as some metallic additives do. For instance, $MoSi_2$ and SiC have shown promising results [71], while ZrO_2 has shown no significant impact on the densification process. However, the average amount of ceramic additive needed to improve the density of the coating is in the range of 5-10wt%, whereas it is lower, closer to 0.5-2wt% for metallic sinter additives [72].

2.4.3. Electrochemistry and other coatings approach

Once we set aside the strategies of creating bulk TiB_2 cathodes and using additives to bypass the associated issues, the next approach is to develop a coating instead of a bulk cathode. Several coating techniques have been attempted over the past decades, as illustrated in Figure 2-6. In this section, we will mention some results from these studies.

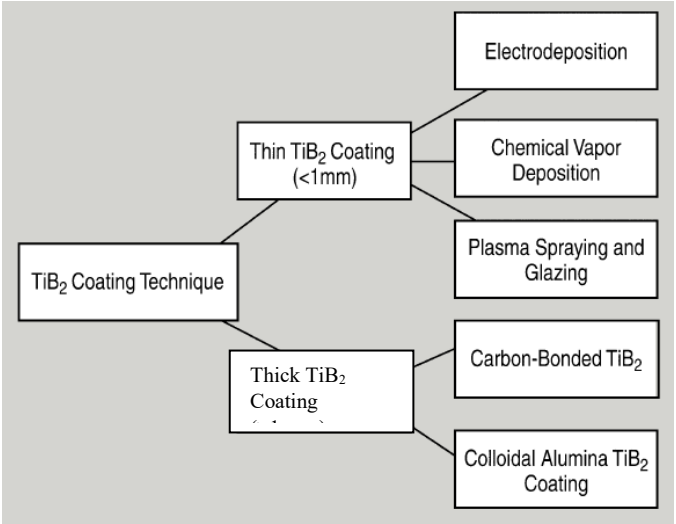

Figure 2-6 Titanium diboride coating techniques classified by thickness [72].

According to a study by A.Becker et J.Blanks [73], chemically vapor-deposited TiB_2 coatings showed a short lifetime due to an attack on the grain boundaries, leading to the coating's detachment.

Electrodeposition has also been used as a process, with a NaCl-KCl-NaF-K_2TiF_6-KBF_4 electrolyte heated at 700 °C. N. Rybakova [74] found that the homogeneity of the coatings was greatly affected by the pulse sequences and current density applied during the deposition. The coatings obtained under these conditions exhibited good wear resistance. However, Simov et al. [75] revealed in their work that the formation of dendrites led to low mechanical stability in the electrolytic bath.

A carbon-bonded TiB_2 coating developed by Comalco, derived from a mixture of TiB_2 and carbonaceous cement, demonstrated good properties for Hall-Héroult cell applications.

However, a reaction occurred between the cement and the aluminium layer forming on the cathode, creating Al_4C_3. As the cement dissolved, the TiB_2 particles were released, making the lifetime of the coating a significant issue [76], similar to approaches using additives.

Moltech company extensively tested its TiB_2-colloidal alumina extensively and found that it lasted for about three years under real conditions, with a TiB_2 dissolution rate by aluminium of 0.3 mm/year. However, this approach involved a multilayer technique, including a protective layer, an aluminium-wettable layer, and an anchorage layer on top of the substrate. Increasing the particle size of TiB_2 was found to enhance the mechanical properties but also increased the coating's electrical resistivity [77]. The coating's porosity was still about 30%. While these colloidal alumina coatings and carbon-bonded composite coatings could lead to thicker coatings of 3 mm to 8 mm with relevant properties, their lifetime suffered considerably, even worse than in previous techniques like CVD or electrodeposition.

In 2001, the ambient-temperature solidified coating method (ATC) was developed and adapted to TiB_2-containing coatings. The coatings obtained exhibited excellent properties for the desired application, such as high aluminium wettability, low electrical resistivity, strong bond strength, high compressive strength, and resistance to thermal shock and sodium expansion, which is one of the main causes of deterioration in Hall-Héroult cell cathodes.

This method underwent an industrial scale test at the Guangxi Branch of Aluminium Corporation of China, which demonstrated its superiority in terms of lifetime compared to the non-coated cathode. Figure 2-7 illustrates that the non-coated cathode is more deteriorated than the coated one. The lifetime of Hall-Héroult cells is usually determined by the deterioration of the cathode lining until it is broken by sodium penetration. The type of carbon additives to the TiB_2 coatings greatly influences its resistance to sodium penetration, along with the grain size and type of sintering agent, although to a lesser extent [45].

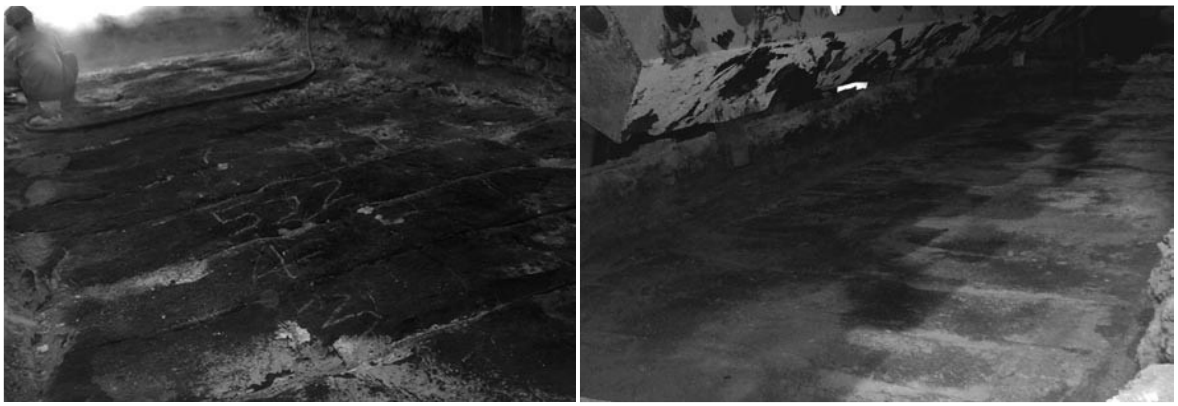

Figure 2-7 Cathode surface in 160 kA prebaked cell after one year of use, without coating (left) and with TiB_2 coating (right) [45].

In conclusion, each technique described above either resulted in a coating without sufficient mechanical stability that delaminated or required a more complex structure to avoid delamination, which negatively affected electrical properties. Our goal will be to overcome

these challenges without using additives by employing thermal spraying techniques, aiming to produce TiB_2 coatings with good mechanical structure and electrical properties.

2.5. Plasma Spraying

Thermal spray processes are efficient, versatile, and cost-effective methods for producing micro-structured functional coatings. Among these techniques, plasma spraying stands out as it uses plasma as a thermal energy source.

2.5.1. Physics of plasma spraying

The family of thermal spraying processes involve spraying a stream of molten, semi-molten, or solid particles onto a substrate, where the particles are heated and accelerated upon impact [78]. The techniques can be categorized based on how the jet is generated, such as electric discharge (DC arc or pulsing arc), RF glow discharge, combustion, or explosion. The main thermal spray techniques are depicted below in Figure 2-8. These spraying techniques offer various possibilities, including the development of nanostructured coatings, deposition in a controlled atmosphere for easily oxidized materials, and achieving high productivity or high-quality coatings. They can also deposit a wide range of materials, including ceramics, metals, and alloys.

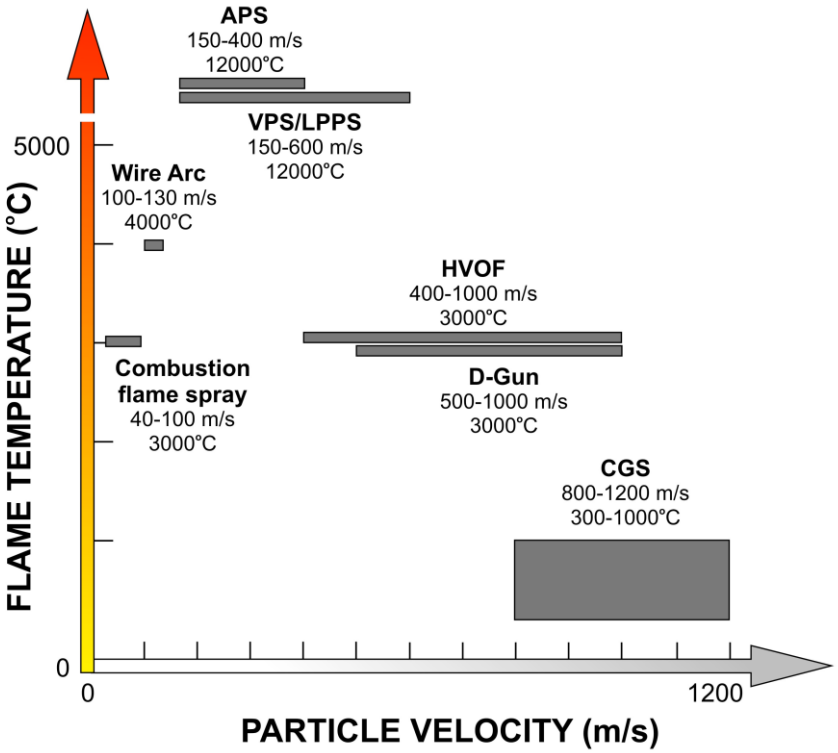

Figure 2-8 Schematic representation of the typical flame temperature and particle velocity for different thermal spray systems [79].

Atmospheric Plasma Sprayed (APS) coatings find applications in various sectors, such as thermal barrier coatings (TBCs), with materials like YSZ [80], corrosion-resistant surfaces, or biomedical prosthesis with hydroxyapathite [81]. These coatings have been developed through a deeper understanding of the physical phenomena involved in plasma spraying and the advancement of online monitoring systems, enabling the industrialization of the processes during the 1980s and 1990s. In APS, as seen below in Figure 2-9, the plasma gas enters the torch at the base of the cathode and is heated by the arc between the cathode and the cylindrical anode nozzle. The resulting plasma jet can reach temperatures and velocities in the range of 12,000-15,000 K and 500-2500 $m.s^{-1}$, respectively, depending on operating parameters and torch design. The plasma jet transports the injected particles to the substrate.

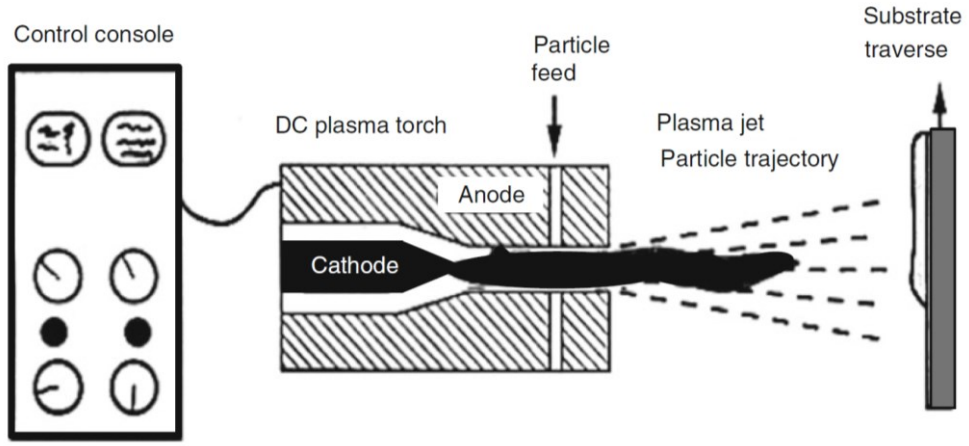

Figure 2-9 Schematic representation of plasma spray process [78].

The coating formation involves the succession of splats formed upon the impact of the spray particles, as seen below in Figure 2-10. APS, first invented in 1922 and heavily developed in the 1960s, utilizes an arc-induced plasma to transfer heat to the powder and accelerate the particles [82]. The plasma gas composition typically includes argon to stabilize the arc, along with secondary gases like H_2, N_2, or He, which help narrow the spray jet and enhance heat transfer to in-flight particles. The applied current ranges in the hundreds of amperes, and the resulting voltage is in the range of 30-70 V, increasing with the anode-cathode distance in the torch and the amount of secondary gas in the plasma. In the plasma plume, temperatures can reach as high as 14000K to 28000K. Recent years have seen efforts to optimize torch geometry to improve electrode durability and coating consistency. Electrode degradation mechanisms include arc-induced deterioration of the tungsten cathode, leading to tungsten particles appearing in the coating [83], and anode erosion due to high heat fluxes causing self-increasing erosion [84].

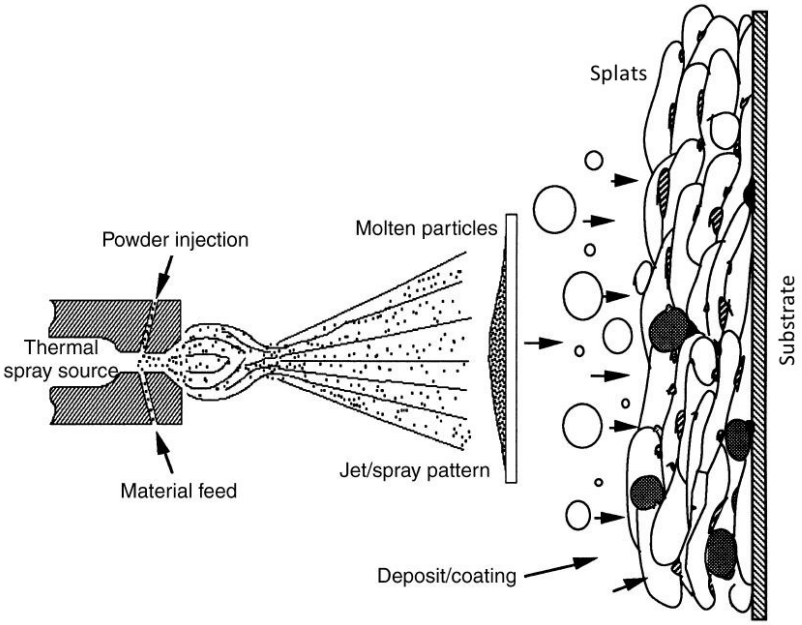

Figure 2-10 Formation of the coating in a thermal spray process [85].

One crucial parameter in powder-based thermal spraying techniques is the size distribution of the powder, which impacts the particle trajectory in the plasma and the resulting coating. Powders used in APS should have a relatively narrow and unimodal size distribution to ensure consistent results. Particle size also affects how the particle's speed correlates with the plasma velocity, with larger particles having more inertia and slower acceleration compared to smaller particles, influencing splat flattening. This relative movement of particles and plasma is quantified by the Reynolds number Re [86].

Thanks to the high temperatures achieved in plasma spraying, a wide range of materials can be deposited, including metals, ceramics, polymers, and cermets. The high velocities of the particles upon impact ensure excellent flattening. However, the combination of excellent particle melting and entrainment of air within the plasma jet leads to enhanced oxidation, which is why oxide ceramics are the primary materials deposited by APS. Examples include Al_2O_3, TiO_2, ZrO_2, $ZrSiO_4$, Cr_2O_3, and Y_2O_3, with Yttria-Stabilized Zirconia being widely used for thermal barrier coatings. It is the main industrial application of APS. For materials where oxidation must be avoided, a controlled atmosphere is typically used. Some of the post-treatments that have been used in the past to increase density were furnace annealing, laser treatment, or sealing [82].

2.5.2. Plasma Sprayed TiB_2

In 2014, P. Ruzhen et al. used Atmospheric Plasma Spray to deposit titanium diboride [87], obtaining relatively thick coatings, as shown below in Figure 2-11. However, these coatings were heavily oxidized [88], containing 20wt% of oxygen and the presence of TiO_2, B_2O_3, and $Ti_{1,86}O_3$, consistent with similar studies [89]. The coatings were found to consist of fully melted and partially melted particles, evenly distributed throughout the coating. These oxides are likely to react with cryolite during the Hall-Héroult process, leading to rapid

cathode damage. Like other transition metal borides such as ZrB_2 and MoB_2, TiB_2 has a low oxidation rate at temperatures below 1000 °C, forming a protective B_2O_3 glass layer on the surface. However, at temperatures above 1100 °C or in more oxidizing conditions, such as a humid atmosphere, the oxidation rate increases significantly [46].

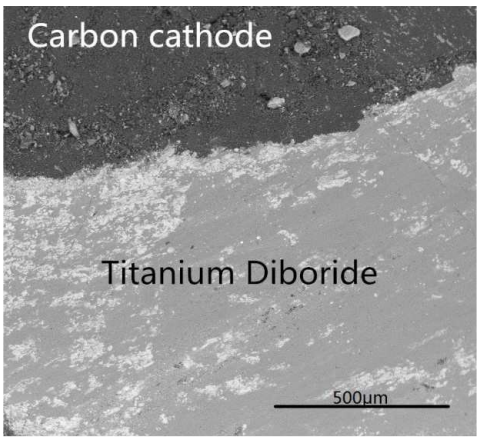

Figure 2-11 Polished cross-sectional micrograph of the as-sprayed TiB_2 ceramic coating [87].

To avoid oxidation, titanium diboride coatings were produced using Vacuum Plasma Spray (VPS), as depicted in Figure 2-12 [90] [91]. These coatings showed no open porosity, good mechanical cohesion, and high aluminium wettability. They also exhibited good adherence to carbon substrate materials. However, the high vacuum required for this technique comes with a high cost, which increases exponentially with the size of the parts to be coated. Given that the cathode surface to be coated is in the range of square metres, the cost becomes a barrier for the industrial application of VPS.

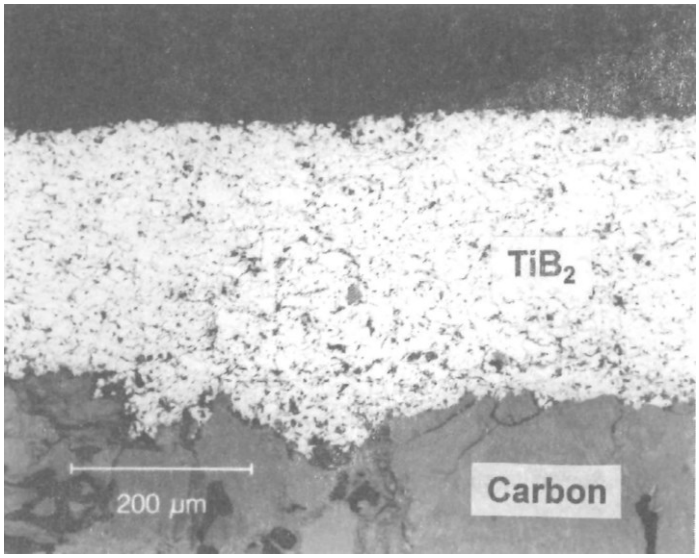

Figure 2-12 Typical microstructure of an interface anthracite carbon substrate and TiB_2 coating formed by VPS.

One additional advantage of a TiB_2 coating is its high hardness. The contact of molten aluminium with the current carbon-lining cathode results in the formation of aluminium

carbide, causing chemical erosion. By developing a dense layer of TiB_2, this phenomenon can be significantly reduced, as well as the expansion caused by sodium penetration, as explained below in Figure 2-13 in the example of the study by F. Hiltmann et K. Seitz [90] [91].

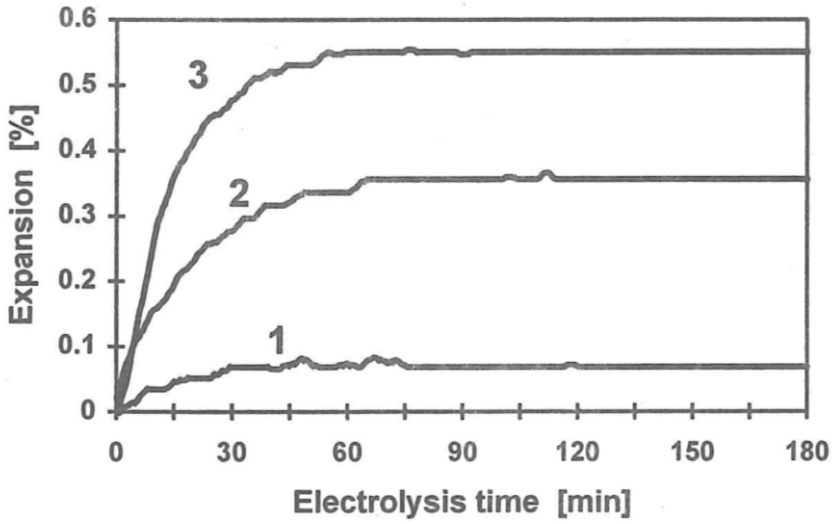

Figure 2-13 Expansion curve examples from Rapoport tests of anthracitic cathode samples. 1 = dense coating, 2 = porous coating, 3 = uncoated, from [91].

As shown in Figure 2-13 above, the coated samples, especially the dense ones, exhibit much lower expansion related to sodium penetration compared to anthracitic graphite cathodes. Semi-graphitized cathodes, to which a portion of the industry has already moved since 2000, already exhibit an expansion between 0.05 and 0.08%.

2.5.3. Suspension Plasma Spray

In the specific case of Suspension Plasma Spray, the powder is not injected in the plasma as is, but within a suspension [92]. This allows the use of powders with a finer size distribution compared to APS [93] [94]. Using powders with a size distribution below 10 µm would lead to agglomeration on the side of the injecting hoses and clog them if used in conventional APS [95]. The possibility to use these smaller particles enables the development of nanostructures with fine pores or even the production of very thin dense coatings [96]. When using a suspension, the particles continue with the flow of the liquid medium carrying them and do not clog the injection system. Upon atomization into the plasma, the solvent used - generally water or ethanol - is evaporated, and the particles are then melted by the plasma, similar to the APS case.

As shown in Figure 2-14, the suspension is atomized by coaxially injecting the atomizing gas, generally Ar, into the suspension, although some more advanced injection mechanisms have been the topic of research and development. The injection process significantly influences the deposition process and its efficiency. In our research, we will use the Axial-III torch, which has an axial injection, an improvement over the more classical radial injection. With radial injection, one must carefully control the speed at which the suspension penetrates the plasma jet to avoid complete penetration throughout the plasma if the speed is too high or complete

rebound from the plasma if the speed is too low. Axial injection in the middle of the torch avoids this issue, and all the particles flow with the plasma, increasing their residence time in the hottest part of the plasma and favoring full melting of the particles in flight. The axial injection is made possible thanks to the multiple-arc plasma generator geometry of the torch. The Axial-III has been studied, for instance, in [97], where Zimmermann et al. analyzed the temperature distribution within the plasma and its inhomogeneity.

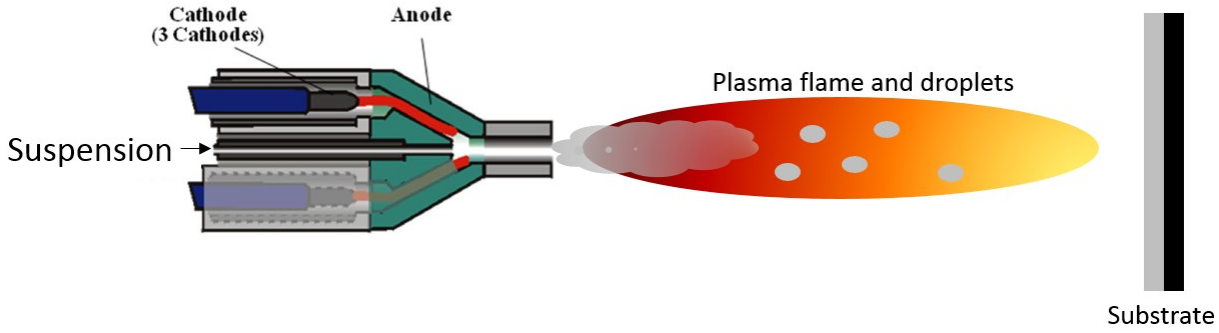

Figure 2-14 Suspension Plasma Spraying using a Mettech Axial III, adapted from [98].

As detailed in Figure 2-15, the droplets, upon entering the plasma, quickly break up into smaller droplets before the vaporization of the solvent, followed by the melting of the particles and their impact as splats on the substrate. The use of a suspension brings specific challenges: to ensure repeatability, they must have a high degree of consistency, which is difficult to establish as fine particles would naturally agglomerate, leading to inhomogeneity in the suspension and therefore in the deposited coatings [92]. Additionally, sedimentation must be avoided. Moreover, the evaporation of the solvent by the plasma cools down the plasma and wastes energy. Therefore, in general, ethanol is preferred as a solvent compared to water, as it has a smaller latent heat of vaporization (841 J/g for ethanol compared to 2257 J/g for water, at 25 °C, with a faster decrease in value with increasing temperature for $\Delta_{vap}H_{[ethanol]}$ compared to $\Delta_{vap}H_{[water]}$ [99] [100].) Finally, the load, the weight percentage of powder in the suspension, is generally limited to below 30%, as the higher the load, the higher the viscosity of the suspension. A higher viscosity lowers the flowability and slows the sedimentation rate, making it more difficult to feed the suspension into the plasma torch. Highly viscous suspensions also tend to lead to the formation of bigger droplets. As the solvent vaporizes, the viscosity of the suspension increases, and the droplet becomes more resistant to breakups. Therefore, for suspensions starting with a high viscosity, the droplets are bigger than for those with lower viscosity [101].

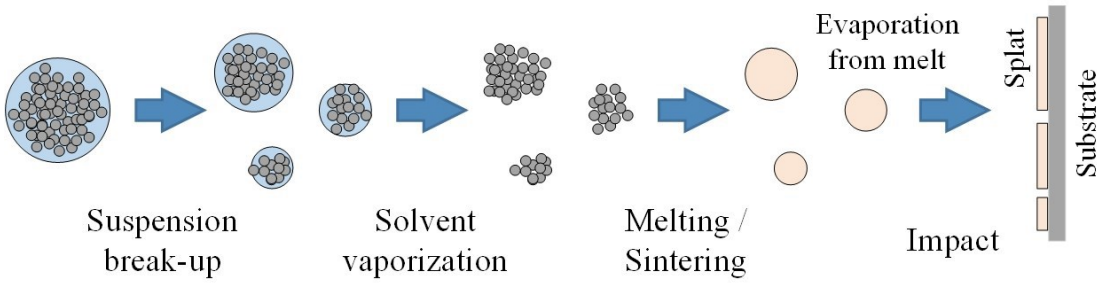

Figure 2-15 Stages undergone by the particles when deposited by Suspension Plasma Spray [102].

2.5.4. Shrouded Plasma Spray

Oxidation is a frequent phenomenon that significantly decreases the corrosion properties of materials. Wear resistance properties of materials can also be negatively affected when spraying composite coatings such as WC-Co or Cr_3C_2-NiCr, where the loss of carbide content through oxidation can reduce its microhardness [103]. Depending on the spraying parameters, the driving oxidation mechanism can be in-flight oxidation or oxidation during splat formation and coating build-up. One way to protect in-flight particles is the use of a shroud [104] [105] [106]. This can be a mechanical shroud [107] as well as a gas shroud [108] [109]. Using a shroud allows spraying coatings in the air while keeping a low oxide content, and preserving the composition of the coatings [110].

As detailed below, there are a variety of geometries that have been used. In Figure 2-16, the shroud types range from pure gas shrouding to solid inert barrier shrouding. The use of gas shrouding generally decreases the temperature of the plasma downstream due to turbulent mixing between the plasma and the shrouding gas. This is not the case when using pure solid barrier shrouding. However, the solid shrouding requires a cooling system due to plasma heat, which makes the installation more complex. Most shroud designs include both aspects of shrouding, and they vary in their physical geometry - length, convexity - and their gas geometry, with either an internal or external injection of the gas shroud, or both. The commercially available gas shroud from Mettech is the one we will use in this work, and it is a mix of a mechanical shroud which is 5.3 cm long and a gas shroud with gas influx both inside the mechanical piece along the inner edge, as well as at the exit of the mechanical piece, around the plasma flame.

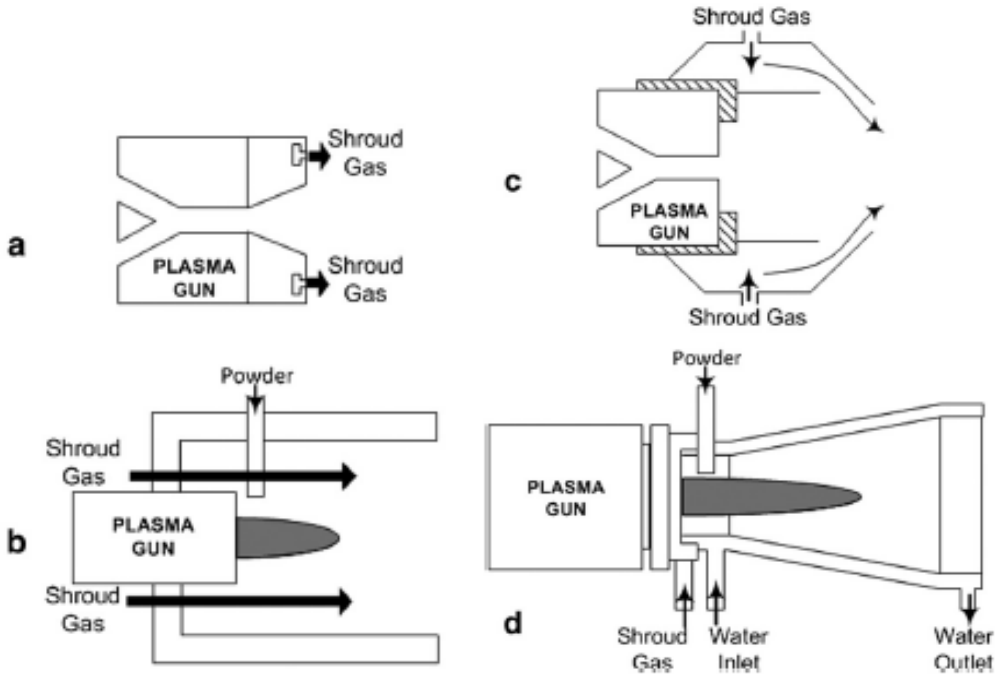

Figure 2-16 Schematics illustrating the range of shroud devices designed for plasma spraying [103].

2.5.5. Laser Treatment of Coatings

Laser treatment of coatings, also known as two-step laser deposition, is referred to as 2SLD in contrast to 1SLD, which is part of the additive manufacturing family for rapid prototyping and involves injecting powder into a melt caused by a focused laser beam. 2SLD is a treatment applied to coatings developed by thermal spraying, painting, screen printing, PVD, paste deposition [82]. The microstructure obtained by this laser treatment is typical of materials that rapidly re-solidify, and these laser-treated coatings have mainly attracted interest due to their wear resistance. They have been studied for applications such as TBCs [111], biomedical coatings [112], wear-resistant composite coatings [113], and hot wet corrosion-resistant coatings [114].

Although some of the 2SLD research shows some alloying or hard-phase dispersion, the main phenomena involved are cladding and glazing. Using a laser to remelt material is a process almost as old as the laser itself [115] and is the most widespread use of the laser on thermally sprayed coatings. Additionally, lasers can be used to sinter and relax stresses in coatings [111]. Metals and alloys alike can be remelted with a laser. Ayers et al. applied 2SLD to plasma sprayed coatings and have shown that the laser beam quality influences the depth of interaction [116], and that the scanning speed and the laser power density are the key parameters influencing the elimination of porosity by the laser and the amount of residual stresses that could relax to create cracks. The roughness caused by the 2SLD was analyzed by Das in [117] where it was shown that by increasing the defocusing of the laser, the temperature difference within the molten pool was decreased, thereby reducing the local difference in surface tension, which ultimately led in the end to a less rough surface. One

thing that is characteristically different between laser remelting of oxide ceramics compared to laser remelting of metals and alloys is that laser-treated oxide ceramics typically exhibit a cracked surface, as shown in Figure 2-17 below.

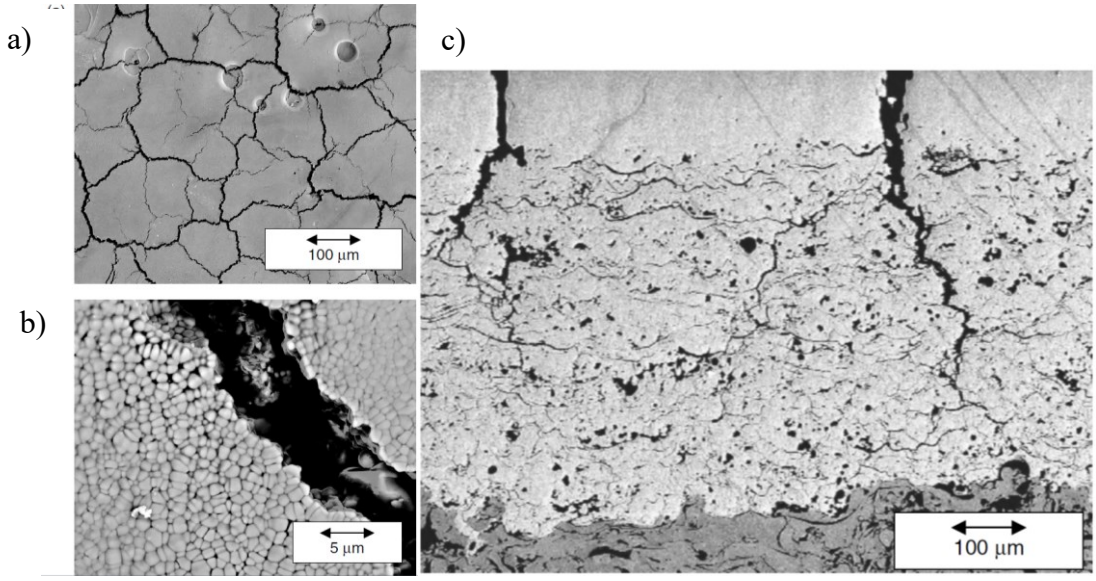

Figure 2-17 BSE SEM of a TBC composed of a MoCrAlY bond coat and an 8YSZ top coat after laser treatment, a)surface, low magnification, b)surface, high magnification, and c)cross-section. [118].

As can be observed in Figure 2-17a and b, the surface re-solidifies in a vertically cracked columnar microstructure. In a study on 2SLD of a mix of Al_2O_3-TiO_2 [119], it was observed that the laser treatment led to coating densification, a columnar microstructure, an improvement in wear and corrosion resistance, as well as in microhardness. These specific coatings, with a vertically cracked microstructure, have been the subject of intense research as they are especially convenient for the development of TBCs. The use of a continuous laser, as opposed to a pulsed laser, has been shown to lead to higher density [120].

2.6. Objectives and Originality of the Project

In this project, our aim is to use a technology to develop titanium diboride coatings for wettable cathodes. Despite ongoing research to develop such coatings through a variety of techniques, none has successfully advanced to the industrial stage as a significant improvement over the technologies currently in place. From sintering to TiB_2-C composites, from additives to colloidal alumina bonding, from electrolysis to CVD, no technique thus far has demonstrated the ability to develop titanium diboride coatings with the required properties for the industrial application considered in this thesis. Although several studies have been previously reported on plasma-sprayed titanium diboride, Suspension Plasma Spray (SPS) has not been attempted before. The objective of this research is to develop mechanically and chemically stable titanium diboride-coated cathodes for aluminium electrolysis using SPS. After reviewing the literature, we hope to achieve this goal by using suspension plasma spray, with the addition of a gas shroud. The influence of the processing parameters on the coatings' microstructure and composition will be detailed in the following chapters. Moreover, the aluminium wettability of the coatings will be thoroughly investigated, and the possibility of a Laser post-treatment will also be considered to assess the potential for obtaining fully dense coatings.

Chapter 3 Methodology

3.1. Experimental Procedures

3.1.1. Starting materials and sample preparation

For the coatings deposited in this thesis, two types of substrates have been used:

- Steel substrates, of the SS304 variety, for the preliminary coatings, in 2.5 cm × 2.5 cm squares,
- Graphite GR008G grade from Graphitestore, USA,
  - In 2.5 cm × 2.5 cm squares, cut from an 8-inch square plate,
  - In disks with a 2.54 cm diameter and 5.5 mm thickness, cut from a 12-inch-long rod, as detailed in Figure 3-1.

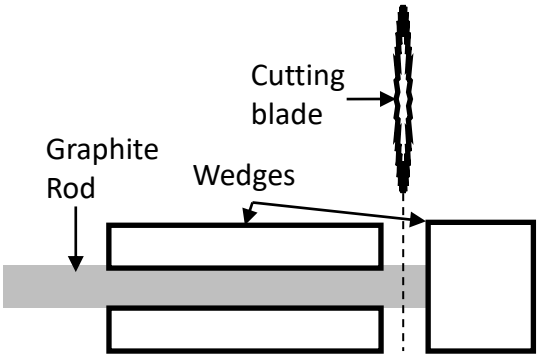

Figure 3-1 Schematics of the cutting machine used to prepare the graphite substrates from the rod.

Depositing on graphite substrates by plasma spraying can be challenging, which is why steel substrates were used in the beginning. However, after these initial experiments, graphite substrates were used, as they are more suitable for the application.

The powder used for suspension plasma spraying was ordered from Hunan HuaWei Aerospace Special Materials, China. It was supposed to have a powder size distribution d_{90} of 1.5 µm. The dark grey powder size distribution was evaluated with a Malvern Spraytec Particle Size Analyzer. It was supposed to have a purity of 98%, with a light oxygen contamination.

The ethanol was anhydrous ethyl alcohol ordered from Les Alcools de Specialites Greenfield Inc. The surfactant Polyvinylpyrollidone $(C_6H_9NO)_n$ was ordered from Sigma-Aldrich Life Science. This amorphous, hygroscopic polymer is commonly used as a binder. The molar weight of this white powder was 360,000 g/mol.

The samples were grit-blasted with parameters detailed in Chapter 4, and their roughness was measured with a roughness meter SJ-210 from Mitutoyo, as shown in Figure 3-2 below. The characteristic roughness used was the R_a - the arithmetic average of a roughness profile. When studying the roughness of a material, other parameters can also be considered, such as the kurtosis R_{ku} which measures the tailedness of the profile about the mean line, the skewness R_{sk} which measures the asymmetry around the mean line of the profile. All these parameters can also be assessed on a surface basis, measuring, therefore S_a, S_{sk}, S_{ku}, etc. In general, in the literature, R_a is the most mentioned roughness parameter.

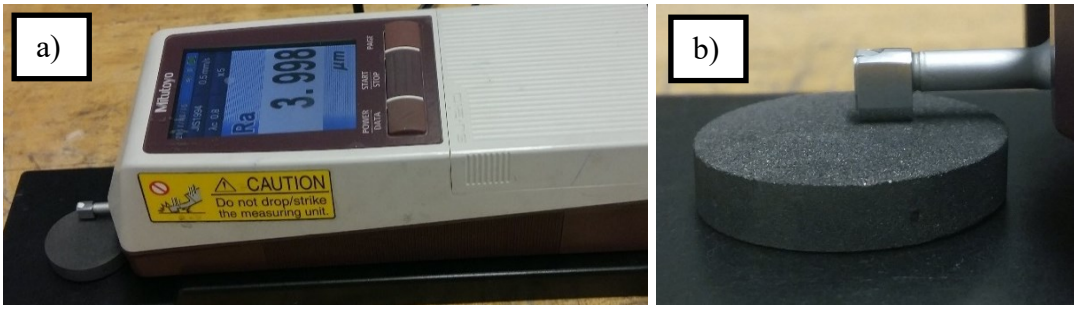

Figure 3-2 Roughness meter (a) and zoom on the measuring tip on a graphite substrate (b).

3.1.2. Suspension Preparation

To properly prepare the suspension, the weight percentage of powder, commonly referred to as the suspension load, must be chosen first. In our research, it will be 10% or 20%. In the SPS community at large, this suspension load rarely exceeds 30% because issues of flowability and stability of the suspension increase significantly above this mark. In SPS, the two main solvents used are water and ethanol, and in our case, ethanol was chosen. That is because ethanol has a smaller enthalpy of vaporization, and as such, it takes less energy from the plasma to burn off compared to water. This is beneficial in our case, as it will decrease the energy loss due to vaporization, and we want the maximum amount of energy to fully melt titanium diboride in flight. Additionally, the storage and manipulation of ethanol in the industry demands a specific control, unlike water.

As shown in Figure 3-3 below, the amount of ethanol is weighed with a balance, and then a surfactant is slowly added to the suspension. Its role is to limit the formation of aggregates and maximize the homogeneity of the suspension, as well as to reduce sedimentation. If the suspension is heterogeneous, then the coating will be as well, and that would be detrimental to the application. In our research, Polyvinylpyrrolidone (PVP) will be used as the surfactant. The amount of PVP in the suspension has been determined to be 1.2 weight percent based on a comparison between the sedimentation time of suspensions with PVP percentages varying from 0 to 1.6%. To maximize the homogeneity of the suspension, magnetic stirring and a sonicator were constantly used during suspension preparation. The PVP must be added slowly to the ethanol to ensure a homogeneous dispersion of the surfactant and to avoid the agglomeration of PVP molecules in filaments. This preparation is done under a nanocabinet to protect the experimenter from inhaling nanopowders and ethanol fume and to maintain a healthy lab environment.

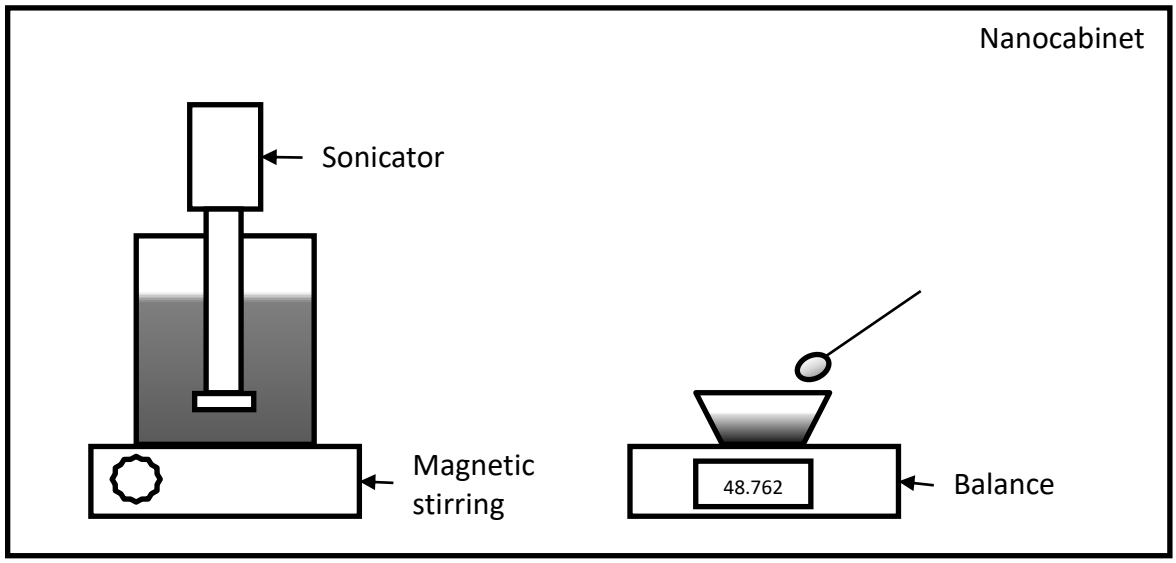

Figure 3-3 Schematics of suspension preparation and homogenization under a nanocabinet

3.1.3. Plasma Spraying

In the process of plasma spraying, there are over 70 intertwined parameters that can influence the coating's quality and properties. Schematically, we can group them as shown below in Figure 3-4. Such a high level of complexity makes plasma spraying both very versatile in terms of coatings sprayed and difficult to finely tune.

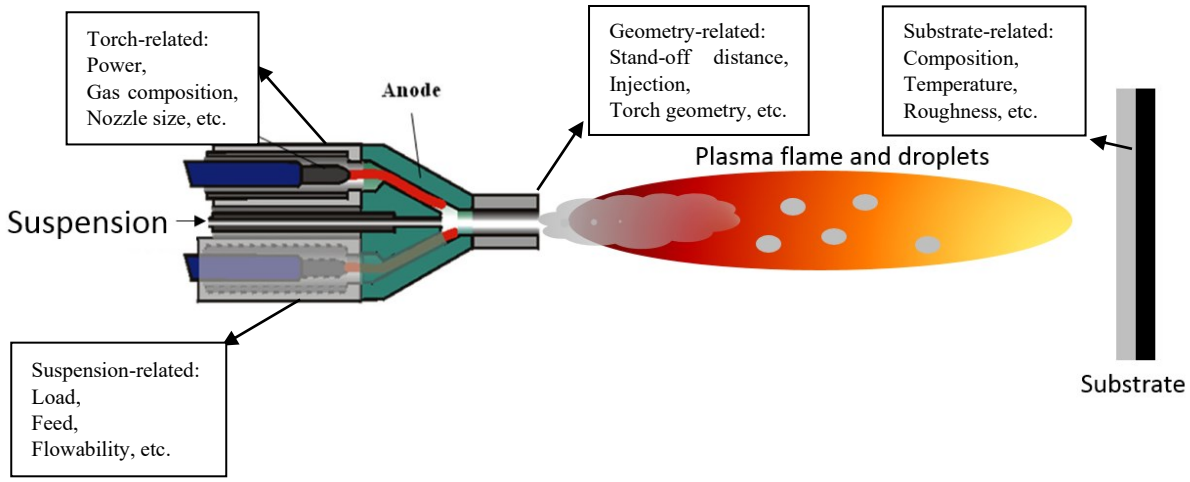

Figure 3-4 Examples of parameters influencing the deposition by suspension plasma spray.

The torch used was an Axial-III torch from Mettech Corp, Canada. It has several advantages, the main one being an axial injection. Thanks to its three-cathode system, the powder or suspension can be injected axially directly into the hottest part of the plasma plume, as shown in the figure above. The axial injection is, therefore, a significant improvement over the more conventional radial injection and should be expected to become standard in the decade to come [97]. Indeed, with radial injection, there is an issue of the pressure with which the medium is injected: if it is below a critical value, it bounces off the plasma and is not

deposited, and if it is too high, then it just pierces through the plasma and is not deposited either.

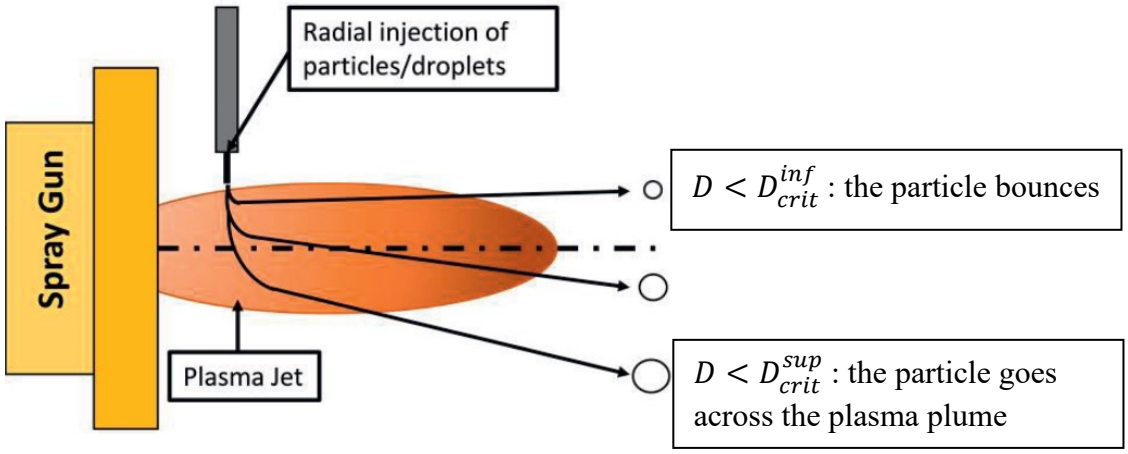

Figure 3-5 Schematic of radial injection of powder in plasma spray [121]

In axial injection, this problem completely disappears, as all the material is in all cases injected into the plasma and directed towards the surface to be coated. The torch was fixed on a robot with six degrees of freedom, and the deposition was made in a spray booth with appropriate ventilation for security purposes, as shown in Figure 3-6 below.

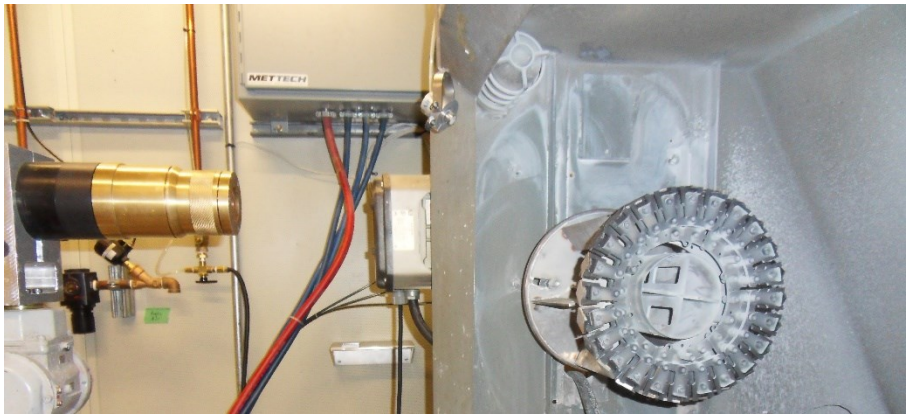

Figure 3-6 Axial-III plasma torch on a 6-axis robot in front of a rotating sample holder.

Additionally, a gas shroud, also available from Mettech Corp, is used to protect molten droplets from in-flight oxidation. The shroud works as a mechanical piece, displayed in Figure 3-7, screwed at the exit of the torch. It is 5.3 cm long and has four gas outputs: two inside the shroud and two at the exit of the shroud. In our case, the shroud gas used was Argon, as it is an inert gas and, therefore, had no possibility to react with our in-flight particles. N_2 could also have been used as a shroud gas, as shown in the literature.

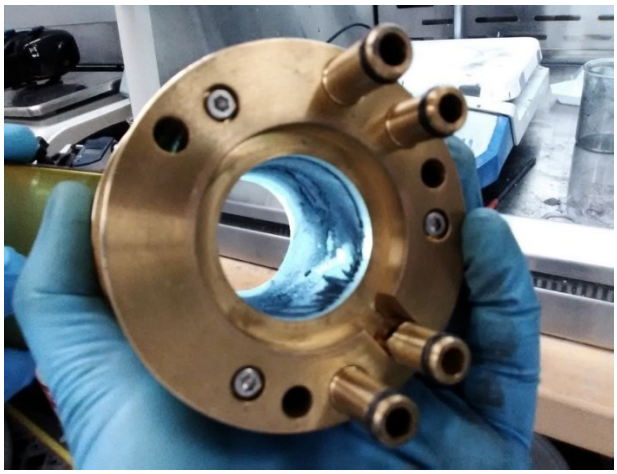

Figure 3-7 Shroud observed from its rear end, with the inlet and outlet of gases observable.

The substrates were put on various sample holders during the thesis, portrayed in Figure 3-8:

- The first one was a static water-cooled sample holder fitting 4 samples, as shown below in Figure 3-8a. It is a home-made set-up which was already available at the lab at the beginning of the thesis. The idea behind the use of a water-cooled sample holder was to try to reduce the damage that could be caused by the intense heat that dissipates through the samples to the sample holder, as well as keeping the substrate temperature relatively low throughout the deposition.
- The second one was a rotatory sample holder, fitting 24 samples, as shown in Figure 3-8b. It is a set-up made by PTC Innovation, linked to University West. The rotation could fill the role of the water-cooling. The speed of the robot was adjusted to keep the same linear deposition speed as with the water-cooled sample holder.

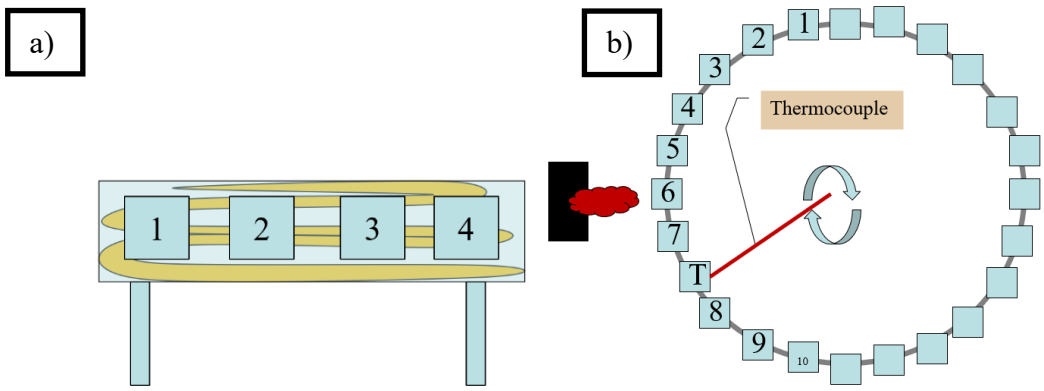

Figure 3-8 Schematics of the sample holders used, (a) static water-cooled, front view, and (b) rotating sample holder, side view as seen in Figure 3-6.

The plasma torch is on a 6-axis ABB robot. Using the associated controller, the trajectory is programmed with a constant linear speed of the torch. Each line has an overlay with the neighbouring ones to ensure a deposition as homogeneous as possible. With a static sample

holder such as the one in Figure 3-8a, the robot sprays on the samples with a linear scan, repeating each scan a definite number of passes to coat a high enough thickness.

During the deposition, when possible, the temperature of the samples was measured. It is an important parameter, as one can observe in the literature [122] [123]. For instance, in [124], Jalilvand et al. showed that when depositing a CoO-NiO mix via SPS, a reduction from NiO to Ni occurred at low substrate temperature, below 950 °C, whereas a single-phase mixed oxide coatings were obtained at a $T_{substrate}$>950 °C. With the static sample holder (Figure 3-8a), a FLIR A320 infrared camera from FLIR Systems Inc., USA was used to monitor the evolution of the samples' temperature. With the dynamic sample holder, such as the rotating one (Figure 3-8b), it could not be used. Thus, a thermocouple adequate to the range of temperature of the system was used. It was glued to the back of one sample with thermal-resistant glue. At first, a home-made IR transmitter was used to receive the data, and later a commercial one was used, an SS-002 thermocouple with a wireless sensor from Omega Inc., USA, to fulfil the same role.

3.1.4. Laser Post-Treatment

One approach that was considered during this research was the use of a laser post-treatment to remelt the top surface and reach a dense layer. It is a technique vastly present in the literature [125] [126] [127]. In our case, the laser used was a 4 kW YLS-4000-CT high-power Ytterbium fibre laser from I.P.G. Photonics, USA, used in continuous mode, as shown in Figure 3-9.

The principle is as follows: by changing a set of parameters - robot speed, laser power - the energy density transmitted to the coating is set to the adequate value to properly melt the top surface of the coating. This can in turn, as shown in Section 2.5.5, leads to change in microstructure. The distance between the laser and the samples is set to the focal distance of the laser, which was 550 mm. More details on this post-treatment process are present in Chapter 5 of this thesis.

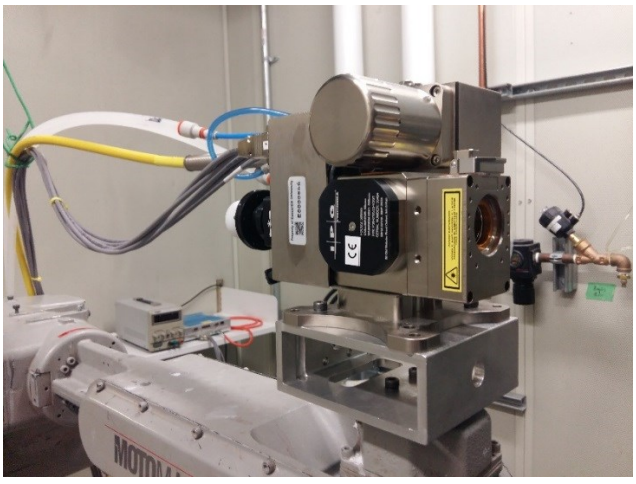

Figure 3-9 Robot-mounted 4 kW Laser used to remelt the top layers of the coating.

3.2. Characterization methods

3.2.1. Particles' in-flight temperature and velocity

The determining factors for plasma spraying can be summarized by the particles' velocity and temperature upon impact. Over the past decades, several systems have been developed to measure those characteristics, such as PIV, the DPV-2000, or Accuraspray. The various measurement methods are based on different approaches: shadowgraphy for imaging, Phase Doppler analysis or diffraction analysis for the light scattering approach, and a two-colour pyrometer for the thermal emission approach [123]. However, these methods have been developed mainly for APS. In SPS, and particularly in SPS with a shroud, the measurements face increased challenges, making it harder to capture a clear signal free of noises. Some of these limitations were discussed in [128] [129] and mainly stem from the high noise-to-signal ratio, which is derived from the turbulent flow, high refraction of light, and high radiation from the plasma. Accuraspray was the system used in our research to obtain an estimate of our in-flight particles' speed, to be correlated with the physical phenomena leading to the microstructures obtained. Below in Figure 3-10 is an example of the output of Accuraspray, indicating the temperature and velocity of the particles.

Figure 3-10 Examples of the outcome of an online monitoring of a plasma spraying process with Accuraspray [130].

As shown in this dashboard, Accuraspray gives us an estimate of the plasma temperature and density. It also provides an estimate of the particles` temperature and velocity through the analysis of the plasma radiation.

3.2.2. Deposition efficiency

The deposition efficiency is an important parameter when considering the costs and, therefore, the industrial applicability. It measures how much material is deposited compared to the amount that is wasted, and it can be calculated using the following formula:

$$DE = \frac{w_{exp}}{w_{th}} = \frac{w_{exp}}{f \cdot N \cdot \frac{1}{R} \cdot L}$$

Where DE: Deposition efficiency

w_{exp}: Coating weight experimentally measured after deposition, in grams (g)

w_{th}: Coating weight theoretically calculated, in grams (g)

N: Number of passes

f: Feed rate, calculated in grams per minute (g/min), from the feed rate of the suspension and the suspension load

R: Robot speed, in meters per minute (m/min)

L: Characteristic size of the sample, in meters (m) - diameter for disks, width for squares

In general, the literature reports lower deposition efficiency in Suspension Plasma Spray – typically ranging from 5% to 30% - compared to Atmospheric Plasma Spray, which typically ranges from 45% to 60% [94]. This lower efficiency is mainly due to the limited amount of solid content in the suspensions, which is generally lower than 30%, as well as the cooling effect of the plasma caused by solvent evaporation.

3.2.3. Bulk Density and Porosity

During this thesis, one of the key objectives, as detailed in the following chapters, especially Chapter 4, was to reach a fully dense coating. To evaluate the density of the coatings, two techniques were employed.

The first, which is more qualitative, involved measuring the thickness and weight of the samples before and after the deposition. This provided an estimate of the density of the coating obtained using the following formula:

$$d_{app} = \frac{w_{fin} - w_{init}}{A \cdot (t_{fin} - t_{init})}$$

With d_{app}: apparent density

w_{fin}: final weight (in grams)

w_{init}: initial weight (in grams)

t_{fin}: final thickness (in millimeters)

t_{init}: initial thickness (in millimeters).
A: area of deposition (in square millimeters)

The second technique, which is more precise, relied on the use of image analysis software ImageJ 1.52n to quantify the porosity of the coatings based on SEM micrographs. The algorithm used in the software is as follows:

- Set the image in RGB
- Split the colour channels
- Crop the image to avoid interfaces
- Adjust and Apply the threshold of pore selection by the default method
- Analyze particles and Display Results to estimate the noise
- Re-Analyze results and Sumarize, based on the minimal value for pore determined at the previous step.

An example of the image treatment is shown in Figure 3-11 below. One of the advantages of using this image analysis software is that it also provides information on the pore size distribution, which is generally smaller in SPS compared to APS.

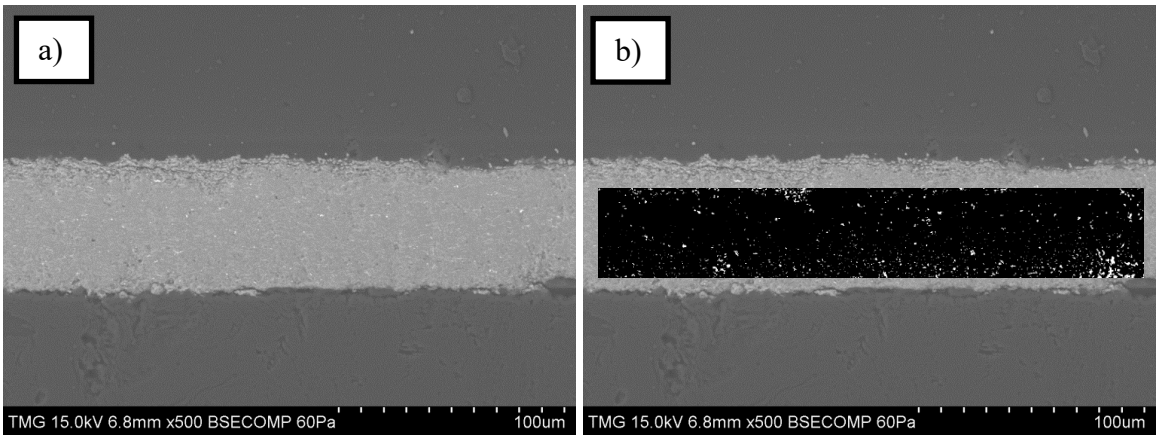

Figure 3-11 SEM micrograph of a TiB_2 coating before (a) and after (b) image treatment for porosity analysis.

3.2.4. Microstructure characterization

Optical Microscopy was used to assess the quality of the coatings and the main features of their microstructure. The microscope used was a GX51 from Olympus, with the StreamBasic software v5.10.

However, the primary tool used to observe the coatings' microstructure was Scanning Electron Microscopy, using a VEGA3 SEM from TESCAN coupled with XFlash 6|10 energy-dispersive X-ray spectroscopy (EDS) detector from Bruker for elemental analysis and mapping.

While the top surfaces could be observed as they were, cross-sections had to be prepared and polished for a more detailed analysis. To do so, the samples were cut using a precision cut-off machine Secotom-15 from Struers A/S, Denmark. As graphite is a very soft material, any blade could be used. The cut samples were then mounted in Epofix resin from Struers, with a 25 mL/3 mL ratio of resin to hardener. After being placed under 0.12 atm for 10 minutes, the resin would solidify in one day. These cross-sections were further ground and polished with a Tegramin-25 machine from Struers, using polishing paper with grits 500 and 800, following by polishing suspensions (3-body polishing) of 9 μm, 3 μm, and 1 μm.

These finely polished cross-sections could then be observed under SEM without the need for a conductive coating, as the material studied is conductive itself. Various settings could be used to observe the microstructures with different contrasts. With secondary electrons (SE), the morphology contrast is increased, while with backscattered electrons (BSE), the elemental contrast is enhanced. All the micrographs included in this thesis were taken in the 3DBSE mode of our SEM, which utilizes all the available detectors and provides optimal contrast, allowing us to analyze the details of the coatings' microstructures. Most of these micrographs were performed in a partial vacuum of 50-70 Pa, except for the high magnification higher than x10.000 where a high vacuum of 10 Pa was necessary to obtain a clear image.

3.2.5. Phase Composition

To study the phase composition of the coatings obtained and verify the oxidation status of our material, as well as potential accidental secondary reactions, three techniques were used during this research work:

- X-ray Diffraction (XRD):
  An X-ray diffractometer Bruker D8 was used, using a Cu K_{alpha} source with a wavelength of 0.154 nm. The program was set to use a 0.5° step to obtain characteristic XRD spectra, which were then compared to references using a database. The XRD spectrum provided information about the presence of a significant oxidation, to obtain a global analysis of the content of the coating
- Energy Dispersive X-ray Spectroscopy (EDS):
  Attached to a Scanning Electron Microscope, EDS is the primary analysis tool for mapping the elements within the coating. In this case, an XFlash 6|10 energy-dispersive X-ray spectroscopy (EDS) detector from Bruker was used. It enabled specific analysis of certain structures observed on micrographs. However, one of its limitations is that it cannot detect light particles unless specifically designed to do so, as shown in [131]. As our main material contains boron, which is the fifth lightest element, the analysis was only semi-quantitative.
- X-ray Photoelectron Spectroscopy (XPS):
  X-ray photoelectron spectroscopy (XPS) analyses of the TiB_2 coatings were performed with an Escalab 220i XL from ThermoFisher Scientific. X-rays were emitted from an aluminium monochromatic source with a photon energy (hν) of

1486.6 eV. The energy scale for all spectra was adjusted so that the C1s peak was at 284.8 eV. XPS peak fitting was done using version 2.3.22 of CasaXPS software. XPS provided valuable information about the surface composition and chemical states of the elements in the coatings.

3.2.6. Wettability by Molten Aluminium

For the specific application of the coatings, measuring the aluminium wettability was of great interest. However, it is no easy task, especially as it must be done in a controlled atmosphere to avoid measuring the contact angle of alumina instead of aluminium.

First, a wire of aluminium (weighing in the range of 50 mg) was cleaned with a molar solution of NaOH for 10 minutes. Then, it was further cleaned in acetone with ultrasound for another 10 minutes. Subsequently, it was placed on the coated substrate in a sealed alumina tube furnace and heated progressively to 500 °C overnight. The setup can be observed in Figure 3-12. At the same time, a vacuum was reached by pumping. The temperature was then brought to 1000 °C at a heating rate of 4°C min^{-1} and was maintained at 1000 °C during the sessile drop measurement. A camera monitored the furnace throughout the process, and from the pictures taken with the help of a fixed light at the other end of the furnace, the evolution of the contact angle of aluminium was measured as an average from both the left and right angles of the droplet. The contact angles were determined manually using ImageJ 1.52n software. This provided us with not only to the static wettability of the coatings, but also the kinetics of aluminium spreading on the samples. This entire set-up is described in Figure 3-12

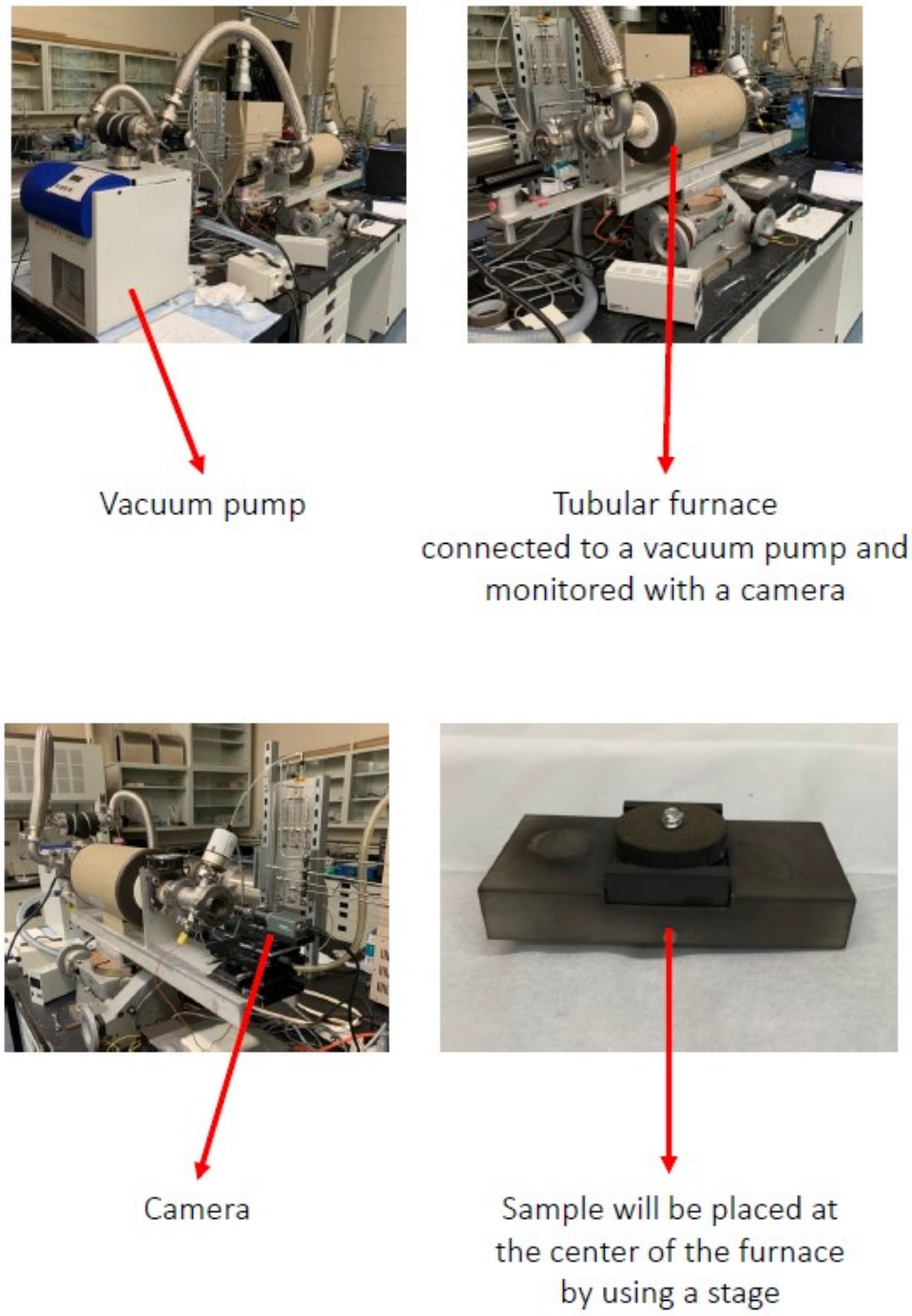

Figure 3-12 System used for aluminium wettability measurement, including a tubular furnace, a vacuum pump, and a camera.

Special thanks to Mr. R. Schulz from IREQ (Hydro-Québec Research Institute) for letting us use his experimental set-up for Al wetting measurements.

3.2.7. Scratch test

Attempts were made to assess the mechanical cohesion of the coatings, as it has proven to be an issue in the steps towards industrializing titanium diboride in the aluminium sector. Scratch test measurements were performed using the Micro Scratch Tester from CEM instruments on a cross-section of resin-embedded samples. Constant normal loads at 1, 2, 3, 5 N and 10 N were applied by a Rockwell C diamond type with a radius of 200 µm in ambient air. The diamond tip moved along a straight line of 1 mm to 1.5 mm at a speed of 0.8 mm min^{-1} from the graphite substrate towards the TiB_2 coating. However, one of the issues encountered was the porosity of those coatings, as will be detailed in the next chapter.

Chapter 4 Influence of the spraying parameters: raw materials, oxidation, and densification

4.1. Difficulty of Melting Factor and Ability of Heating Factor

As suspension plasma spraying is a technique that was never used before to deposit titanium diboride, a starting point had to be found by searching through the existing literature on thermally sprayed TiB_2 coatings, as detailed in

Table 4-1. As this deposition of TiB_2 by Suspension Plasma Spray was a world premiere, we believe it is highly valuable to explain in this section 4.1 the early stages involved in the process of realizing those coatings.

Exp	Power (kW) (V·A)	Primary gas Ar (slpm)	2nd gas H_2 (slpm)	Carrier gas Ar (slpm)	Gun traverse speed (mm/s)	Powder feed rate	Spray distance	Thickness (in µm)
TiB_2 APS [87]		33-50	2-10	2-10	50-200	15-50	80-150	700-900
70%Al_2O_3/30%TiB_2 APS Axial III [132]	99 (137*240*3)	140-180	20	12		15-20	90	250-320
TiB_2 VPS [90]	(70*)	60-80%	20-40%			30-60		10-550
TiB_2 APS [133]	12	20	5 (N_2)	8		20	100	800-1000

Table 4-1 Experimental conditions for titanium diboride deposition by plasma spraying from the literature.

In [87], Ruzhen et al. used a DH-2080 gun to deposit an 800 µm TiB_2 coating which exhibited a lamellar microstructure with partial oxidation and the presence of semi-molten agglomerates. In [132], Cheng et al. used an Axial-III gun to deposit a 300 µm composite coating 70% Al_2O_3 + 30% TiB_2 where there was slight oxidation of TiB_2 and most of it remained undeformed. In [90], Seitz et al. used a Plasma Technik A2000 Vacuum Plasma Spray system to deposit a 300 µm TiB_2 coating with a lamellar microstructure and no oxidation. In [133], Ananthapadmanabhan et al. used a plasma spray system to deposit a 500 µm TiB_2 coating which exhibited significant oxidation and the presence of boric acid, inducing a major decrease in the electrical conductivity. However, the change in medium deposited called for a different approach: to draw the conditions from materials that were

deposited by SPS and which had similar properties in terms of melting point and density. These two material properties are key in determining the residence time of the particles in the plasma. A raw analysis can be derived from taking the calculations from chapter 5 of Pawlowski et al. [82], as follows:

$$AHF = \frac{L \cdot (\int_{300}^{T_g} \lambda_g dT)^2}{\langle \eta_g \rangle \cdot v_p} \geq \frac{H_m^2 \cdot d_p^2 \cdot \langle \rho_p \rangle}{16} = DMF$$

Where AHF is the Ability of Heating Factor, the ability of the plasma to melt a particle

With L: Length of the trajectory of the deposition

$\int_{300}^{T_g} \lambda_g dT$: Mean thermal conductivity of the plasma

$\langle \eta_g \rangle$: Mean viscosity of the plasma

v_p: Velocity of the plasma

Where DMF is the Difficulty of Melting Factor, the difficulty for the particle to be molten

With H_m^2: Enthalpy of melting

d_p^2: Diameter of the particle

$\langle \rho_p \rangle$: Average density

Trying to obtain an ability of heating factor higher than the difficulty of melting factor can lead us to obtain a high percentage of molten particles upon impact, which is a requirement to obtain dense coatings. The melting enthalpy evolves in the same direction as the melting point, as they both characterize the difficulty for a material to change its phase from solid to liquid. Starting from here, we compared said properties of TiB_2 with a couple of other materials which had already been deposited in the lab:

Material	Melting temperature (K)	Density (g/cm^3)
TiB_2	3200	4.52
ZrO_2	2950	5.85
Al_2O_3	2320	3.97

Table 4-2 Density and melting point of various materials deposited by SPS.

From this analysis, the spraying conditions chosen for the first coatings were as follows, based on the experimental parameters used in the lab previously to deposit Al_2O_3 (Exp.1) and ZrO_2 (Exp.2), respectively [134] :

Experiment	Intensity (A)	Working Distance (cm)	Total Gas Flow (splm)	%Ar	%N_2	%H_2
1	220	5	245	75	10	15
2	180	5	180	45	45	10

Table 4-3 Initial set of experimental parameters for plasma spraying.

The feed rate of the suspension was set at 45 mL/min, with a carrier Ar gas flow of 15 slpm, and 80 passes were applied at a linear robot speed of 1 m/s. At first, the suspension deposited was a 10%wt ethanol-based suspension, to ensure no sedimentation or clog would happen, as it would decrease the quality of the obtained coatings.

4.2. Results and discussions

4.2.1. Microstructure of the coatings

The observed microstructure of the coatings obtained is quite typical of suspension plasma spray [135] [136] [137]. It is called the “cauliflower” microstructure, in reference to the appearance of the top surface under microscopy (Figure 4-1d). It is formed when the particles impact on the substrate and create splat upon splat through a shadow effect, leading to this peculiar microstructure. The microstructure resulting from experiment 2 (Figure 4-1a) exhibits it more clearly than the one from experiment 1 (Figure 4-1c). This could be attributed to a variety of factors, but, given the latter analysis, the main contributing factor seems to be the higher N_2 content in the plasma gas, which increases the plasma heat conductivity, leading to an improved melting of the particles in-flight.

One can see in Figure 4-1a that the average thickness of the observed coating is in the range of 350 µm, meaning that the average thickness deposited per pass was 4.4 µm/passes, significantly more than what is usually observed in the literature of suspension plasma spraying [138] but does match some more recent results with newer torch technologies [139] . In our case, this can also be attributed to a relatively high percentage of un-molten particles, leading to a higher porosity and a higher thickness per pass. On Figure 4-1b, we can even observe the deposition of each pass upon each other, and even though some melting seems to happen, it is also clear that a significant number of particles deposit without having experienced a change in physical state.

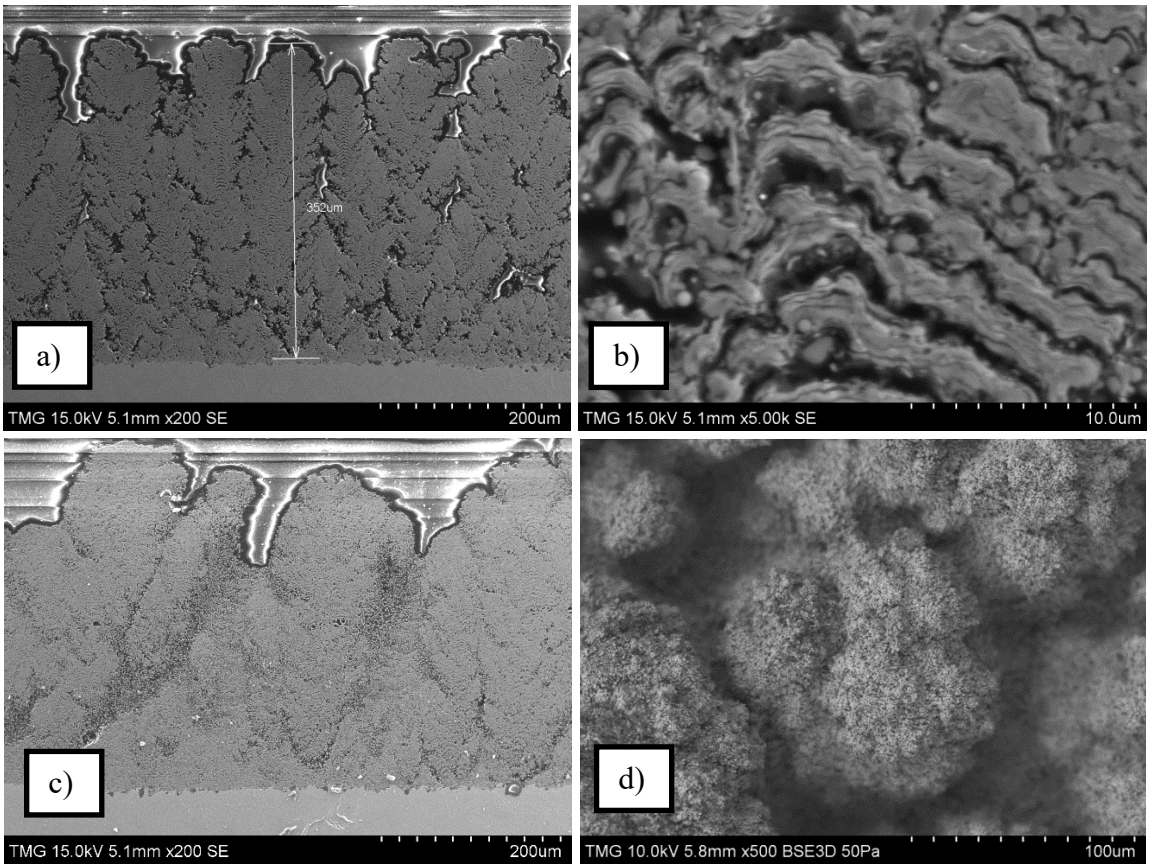

Figure 4-1 SEM micrographs of SPS TiB_2 coating obtained with Experiment 2, cross-section (a-x200, b-x5000) and top surface (d-x500) and Experiment 1, cross-section (c-x200).

As can be seen in the schematics below, a variety of microstructures can be obtained by varying the deposition parameters [140] [141]. They vary from dense to porous, from vertically cracked or segmented lamellar, as indicated in the figure below to columnar, with a decreasing melting percentage of the particles. With a net power of 86 kW and an inversed total gas flow rate of 0.004 (Exp.1) and 0.006 (Exp.2), our experiments do not fit in the graph from Figure 4-2 but we can expect, by extrapolating, a columnar structure which should not be powdery, the higher power leading to a melting increase. If we compare the results from experiments 1 and 2 to the results from [139] in terms of micrography, we can fit it somewhere in the wide columnar region. In general, the particles' speed, measured with an Accuraspray 4.0, was in the range of 560 $m.s^{-1}$.

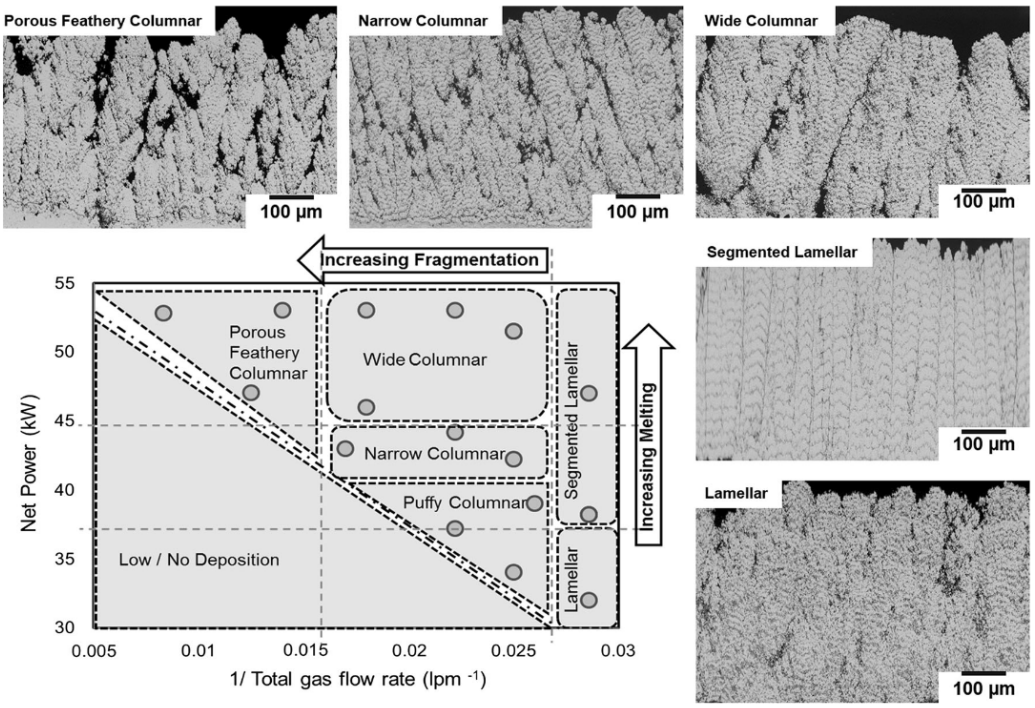

Figure 4-2 Suspension plasma spray process map illustrating microstructure evolution zones at different torch operating conditions combining effects of suspension fragmentation in the plume and melting regimes [139].

4.2.2. Influence of TiB_2 Purity

An issue that was encountered in those first coatings was the purity of the powder used. A significant amount of zirconium was observed, both in XRD and EDS, as shown in figures 4-3 and 4-4. In Figure 4-3 below, one can observe the granular aspect of the raw powder, as well as the particle size distribution, showing a d_{50} of 1.4 µm and a d_{90} of 2.1 µm. This size is in the lower part of the range of grain size distribution associated with suspension plasma spraying. On the micrograph of Figure 4-3a, we can also observe some particles that appear lighter. Given that the image is done with backscattered electrons, this difference in contrast corresponds to an elemental difference, meaning that the lighter elements correspond to atoms with a higher atomic number, which are the zirconium atoms. As observed in the XRD spectrum of Figure 4-4, the zirconium is present as an oxide, ZrO_2, as shown by the characteristic peaks identified.

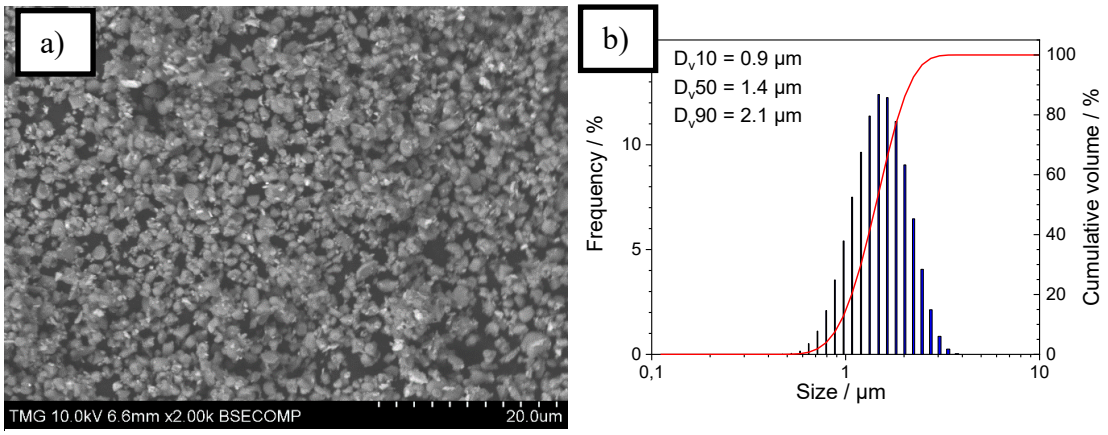

Figure 4-3 SEM micrograph of the raw powder (a) and particle size distribution associated (b).

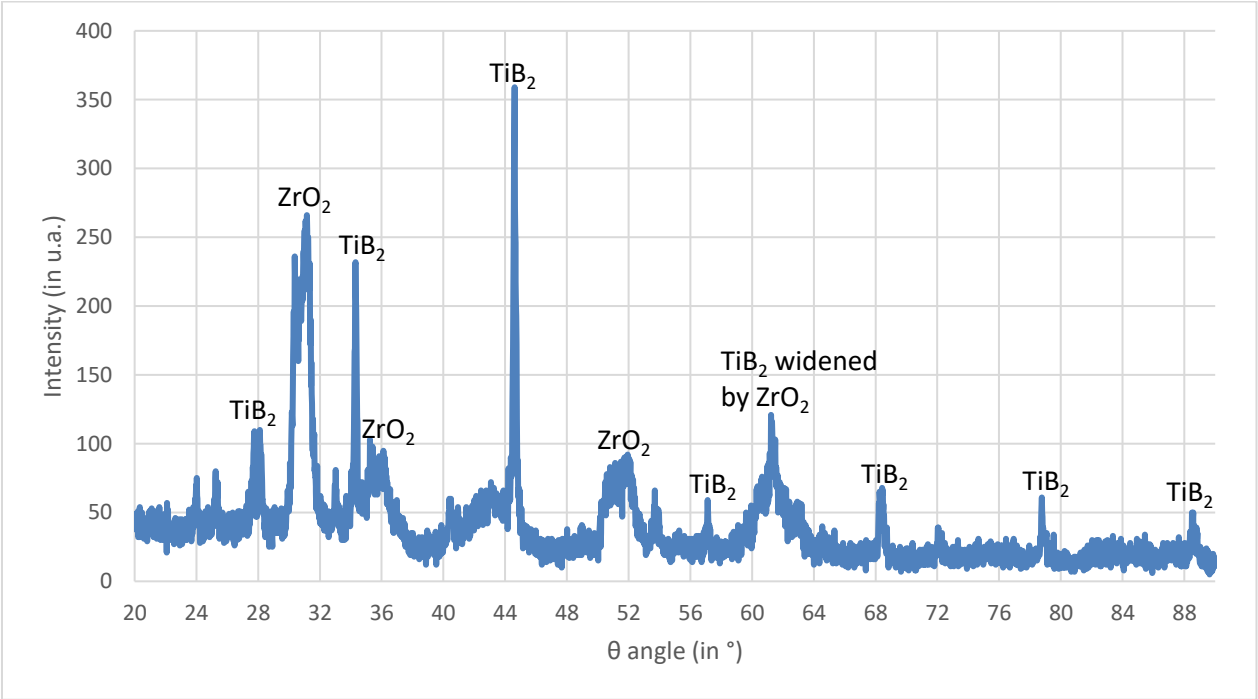

Figure 4-4 XRD spectrum of SPS TiB_2 coating.

After analyses, it was observed that this zirconium was, in fact, present in the starting powder used, as shown below in Figure 4-5a. Upon inquiry with the manufacturer, the use of ball milling with YSZ balls was a step in the process of manufacturing the powder, and that is where the pollution came from. The Yttria peaks are not observed as Yttria in YSZ is typically a few percent, 8%YSZ being the most common, and a quantity of a few percent of a few percent, in the range of 0.08% is unlikely to be distinguishable in the spectrum. The zirconia can be observed in the lighter particles in the micrograph above. The origin of the contamination can also be an explanation for the relatively broad width of the ZrO_2 peaks: resulting from debris from ball milling, they are likely to be relatively small, and with a highly inhomogeneous strain distribution. This leads to a widening of the XRD peaks.

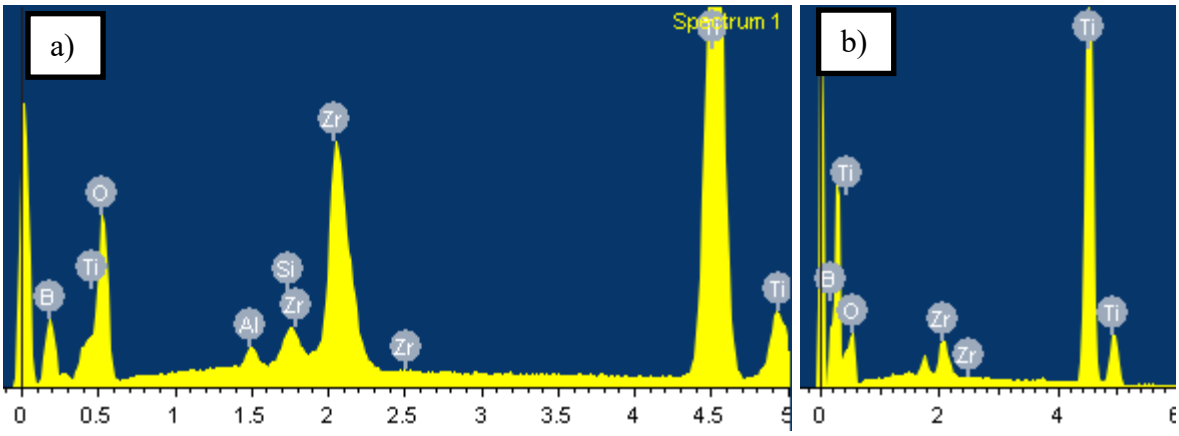

Figure 4-5 EDS spectrum of raw TiB_2 powder, first contaminated batch (a) and second purer batch (b).

To solve this contamination issue, a new batch of powder was ordered from the same manufacturer, this time with a significantly lower zirconia pollution: 2% instead of 14%. The EDS performed in Figure 4-5 above shows the relative reduction in pollution. On top of this, and as planned, the boron cannot be correctly detected by EDS as it is too light an element for our detector, which is why the data used to determine the zirconia pollution is not the absolute zirconia weight percentage measured by EDS but the ratio Zr/Ti. In case a, the Zr/Ti ratio was 17.9 at%. In case b, the Zr/Ti ratio was 3.2 at%.

Another important aspect is the fact that the presence of a relatively high amount of ZrO_2 seems to enhance the cauliflower microstructure. Even though it is still present in subsequent results, as can be seen from top-view micrographs, it is evident from cross-section micrographs that it is made of wider, more powdery columns. The hypothesis we propose for this is that as the YSZ is being molten by the conditions of plasma spraying used in this section whereas the TiB_2 is not, the zirconia provides the architectural skeleton of the coating upon impinging on the substrate, and the unmolten titanium diboride particles fill it. Moreover, the zirconia contamination coming from ball milling is composed of fine particles, which further increases the tendency to form columns, as schematized in the figure below.

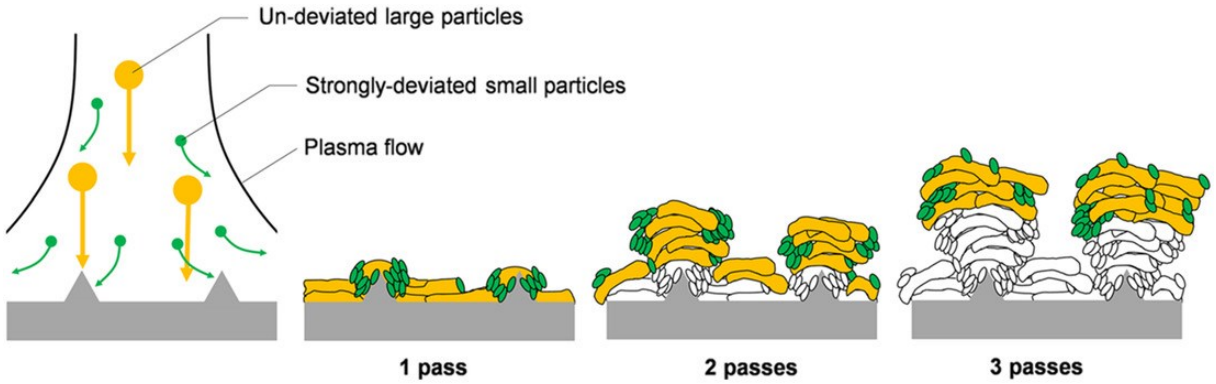

Figure 4-6 Schematic representation of the formation of typical tapered columns by the concurrence of small and large particles in SPS [142]

4.2.3. Difficulty of Melting TiB_2

From the micrographs shown so far, one thing is relatively clear: the particles are not molten upon impact. Their shape, size and overall appearance remain unchanged from the raw powder to the coating, which is characteristic, not even of in-flight re-solidification before impact, but even of not melting the particles at all in the process. This is especially evident in Figure 4-7 below: comparing the particles in the raw powder and the particles in a coating, it becomes evident that they are similar in shape and size, which is most simply explained by the fact that they did not undergo any phase transition of some sort. In the coating micrograph of Figure 4-7b, some lighter material seems to have undergone a change and acts as a binder between particles. The lighter character of this binder could be interpreted as a zirconia-rich binder, easily explained by the fact that zirconia has a lower melting point of 2450 °C and therefore will undergo melting during spraying before titanium diboride does.

Thermodynamically, the plasma heat is enough to melt the particles. But the kinetics also must be considered: the time spent by each droplet in the plasma plume is very limited, and increasing it is one of the directions to take to melt a material with a high melting point. Indeed, the high melting point of titanium diboride (2970 °C), combined with its relatively low density (4.52 g/cm^3), means that the particle has a low residence time in the plasma, and as such, does not receive enough heat to be fully molten upon impact. Typically, the residence time in APS is in the range of one ms to four ms.

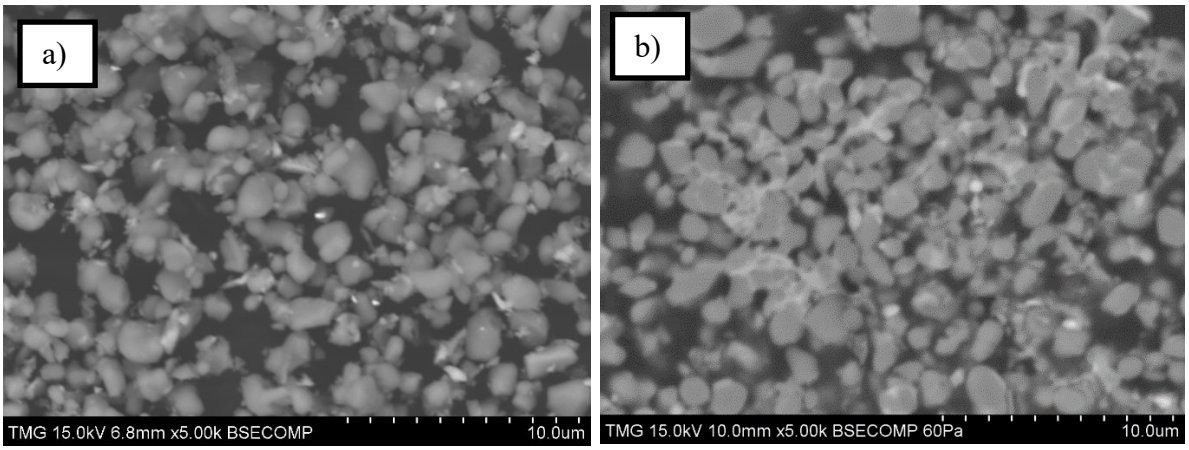

Figure 4-7 SEM micrograph x5000 of raw powder (a) and of particles in the coating (b-Exp.2).

The lack of particles' melting renders the coating highly porous: if the particles are not liquid upon impacts, then they cannot form compact splats. This led to coatings with as high as 31.07% porosity for Exp.1 and 29.45% for Exp.2, as shown in Figure 4-8. These results are comparable results in terms of porosity and are significantly too high for the desired application.

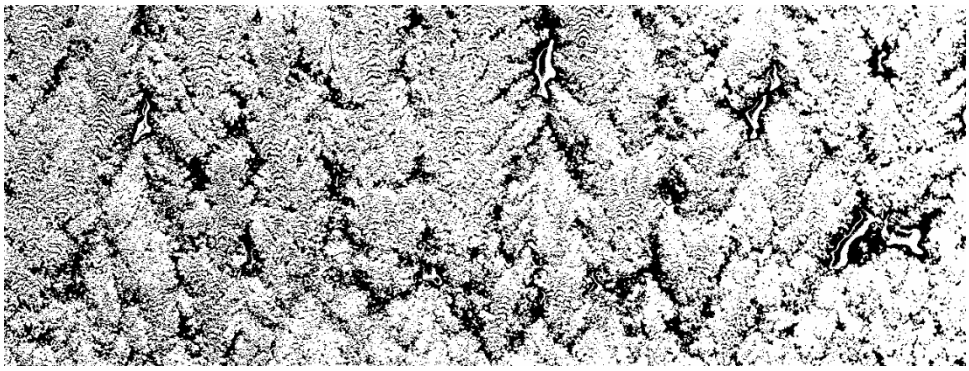

Figure 4-8 Examples of porosity analysis done with ImageJ, on a portion of the micrograph from Fig.4-6a.

To tackle this issue, the parameters should be optimized to increase the available heat per particle to improve in-flight melting, as will be described in Section 4.4.

4.2.4. Influence of the nature of the substrate

When depositing with similar conditions, as detailed in Table 4-4, on two different substrates, stainless steel and graphite, the influence of the substrate on the coating's quality can be determined. Experiments 1, 2, and 3 were done on stainless steel substrates. However, in condition 3, the use of the gas shroud to protect from in-flight oxidation led to a higher heat available per particle. As already mentioned, the use of the gas shroud requires a longer stand-off distance, as the mechanical piece of the shroud is itself 5.3 cm long, hence the increased working distance of 8 cm. As shown in Figure 4-9a, a delamination of the coating was observed in this case. However, this was not the case when using the same experimental conditions but depositing on graphite, as exhibited in Figure 4-9b.

Experiment	Intensity (A)	Working Distance (cm)	Total Gas Flow (slpm)	%Ar	%N_2	%H_2	Shroud	Substrate
3	180	8*	180	45	45	10	Yes	SS304
4	180	8*	180	45	45	10	Yes	Graphite

Table 4-4 Experimental conditions of SPS TiB_2 coatings deposited on Stainless Steel and on Graphite.

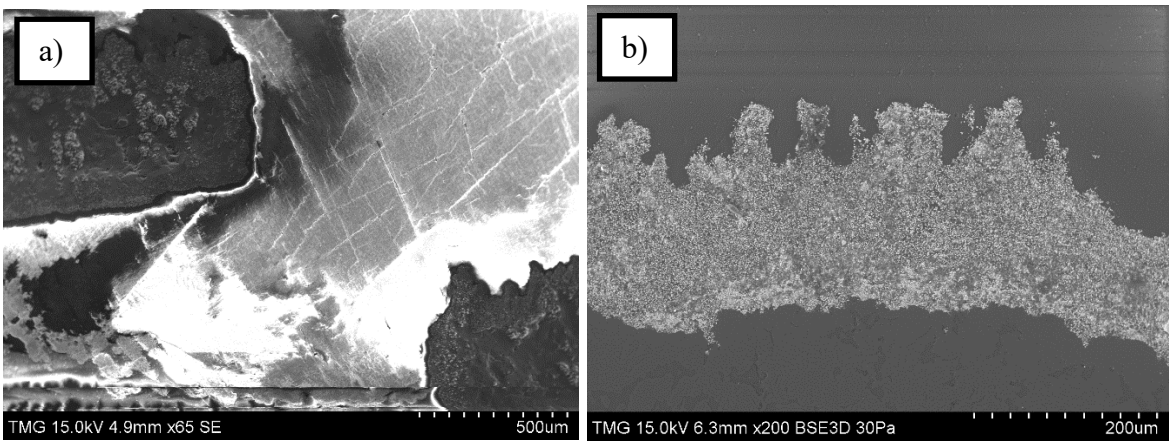

Figure 4-9 Delamination of TiB_2 coating from stainless steel (a-Exp.3) and coating made with same conditions of deposition but on graphite (b-Exp.4).

Upon further analysis, this was attributed to the intense heat flowing through the substrate during deposition and upon cooldown at the end of the deposition, and to the difference in thermal expansion coefficients between stainless steel and titanium diboride [47].

$\Delta TEC = TEC(SS304)-TEC(TiB_2) = 17.3-7.4 = 9.9 .10^{-6}$ /°C

$\Delta TEC = TEC(Graphite)-TEC(TiB_2) = 2.0-7.4 = -5.4.10^{-6}$ /°C

This difference in TEC led to a difference in expansion during and after spraying, and the thermally induced mechanical stresses it created led to the delamination of the coatings. That is why, for all further research, the coatings will be deposited on graphite, as it is the application but also as this means a lower difference in TEC, and therefore lower stresses, and better mechanical cohesion. However, the porosity of the coating is still extremely high, up to 63.9%, as can be observed from the powdery microstructure in Figure 4-9b.

4.2.5. Influence of the Roughness of the Substrate

As the microstructure obtained depends on a shadow effect, it therefore relies on the roughness of the substrate to some extent. However, while grit-blasting stainless steel is relatively easy, doing the same for graphite in a controlled manner is harder since graphite is a significantly softer material. For the purpose of obtaining repeatable and relatively homogeneous coatings, we need the substrate to be in a consistent state before the deposition. Additionally, a rougher substrate tends to enhance the adhesion with the coating to some extent [143]. The parameters of the grit-blasting that can be controlled include the size of the grit used, the pressure of the grit-blasting, its duration, and the distance between the grit-blasting gun and the substrate. Since graphite is soft, using smaller grit size gives us better control over roughness. Hence, we chose the #80 grit size, which corresponds to 165 µm, the smallest available in our laboratory. Among the other parameters, the only one we can set scientifically with our set-up is the pressure. The distance might vary from one user to another

and, for the purpose of this study, is in the range of 5 cm. As for the duration of the grit-blasting, it has been set at 15 seconds. When grit-blasting was done with shorter or longer distances (1 cm and 10 cm, respectively) or with a duration longer than 30 seconds, the inhomogeneity in the roughness state was too high based on optical analysis, or the roughness of the substrate was too high.

As shown in Figure 4-10, roughness measurements were made on each substrate before the deposition, while the other parameters were kept constant. We can see a correlation between the average roughness Ra and the grit-blasting pressure. Some cross-sections after plasma spraying titanium diboride are shown in Figure 4-11, to reveal the impact of difference in substrate roughness on the coating's microstructure.

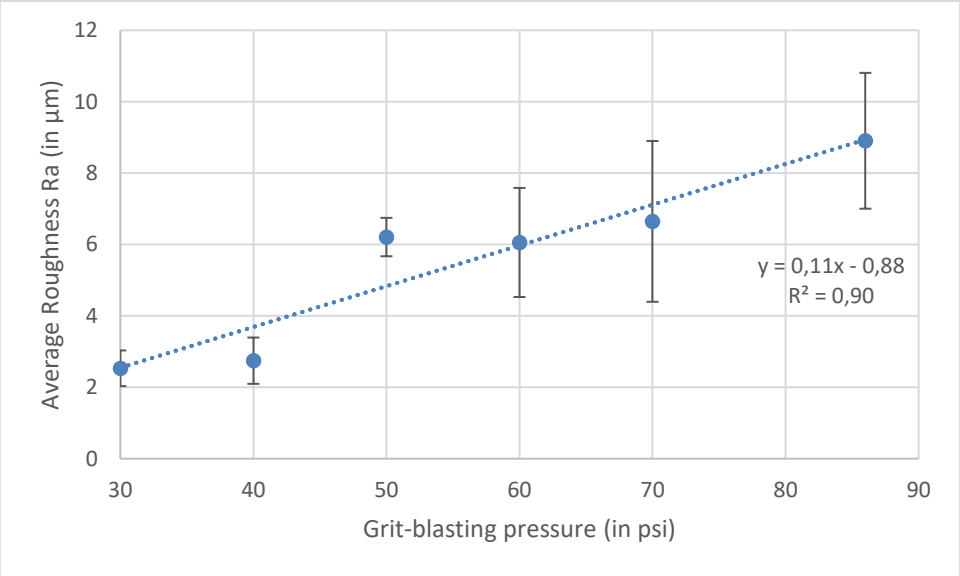

Figure 4-10 Graph of the Ra measured to the grit-blasting pressure for graphite, all other parameters being constant.

As can be seen from micrographs below in Figure 4-11, the roughness of the substrate can significantly impact the adhesion and microstructure of the coating. In Figure 4-11b, without grit-blasting, deposition on a flat substrate leads to poor adhesion and the formation of cracks at the substrate-coating interface, which are not seen on grit-blasted samples. In Figure 4-11a, one can observe that high roughness leads to a strong local shadow effect, resulting in inhomogeneity in the coating structure, with variations in porosity between denser and more porous region, ranging from 13.55% to 36.2%. Such inhomogeneity in porosity will create pathways for sodium penetration and coating delamination in the Hall-Héroult cells. In Figure 4-11a, one can also see that a depression in the coating's surface leads to the growth of a column. In conclusion of this study, the optimal grit-blasting conditions were set at grit-blasting with #80 alumina, at 5 cm distance from the substrate, for 15 seconds, and at a pressure of 50 psi. This resulted in an R_a of 5±1 µm.

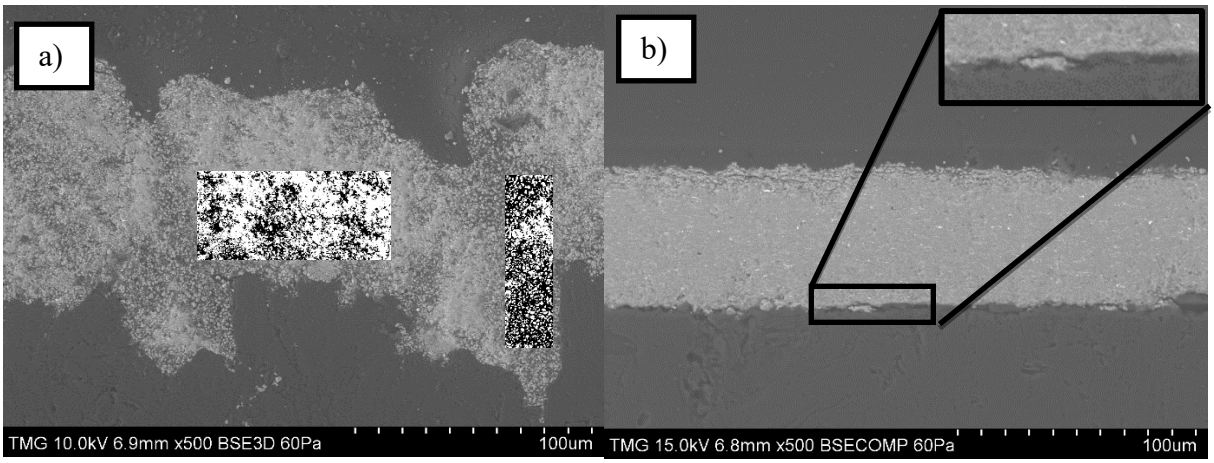

Figure 4-11 Micrographs of coatings deposited on the substrate with various roughness .

4.3. Tackling the Issue of Oxidation

As explained in section 2.5.2, in-flight oxidation poses challenges for TiB_2 deposited by atmospheric plasma spray. To address this issue, we will employ an argon shroud to protect in-flight particles from oxidation. This section will discuss the effectiveness of this approach, its impact on the microstructure of the coatings, and its influence on the wettability of the coating by molten aluminum. Some of the work presented in this chapter has been published in the article [144].

4.3.1. In-flight Oxidation and the Shroud

The experimental conditions for the coatings studied in this section are shown below in Table 4-5. These conditions are essentially the same as those used in Section 4.2 (Experiment 4), but with a higher intensity of 220A and a shorter working distance. The reasons for these changes are addressed with in Section 4.4. Increasing the plasma intensity results in more heat being directed towards the in-flight particles, leading to a higher percentage of molten particles. A shorter working distance, 5.3-6.3 cm compared to the previous 8 cm, reduces the probability of in-flight re-solidification and increases the likelihood of particles impacting in a fully molten state, which is ideal for obtaining dense coatings. The only difference between conditions 5 and 6 is the use of the shroud, which necessitates a longer working distance due to the length of the shroud itself (5.3 cm). To determine if oxidation was observed in suspension plasma sprayed TiB_2 coatings. EDS did not show anything of significance. However, under XRD, some oxidation was observed without the shroud, whereas none was observed with the shroud. In both spectra on Figure 4-12 (with and without the shroud), as well as in the spectrum of the raw powder, the typical peaks of titanium diboride were observed, the main ones at 27.68 °, 34.11 °, and 44.48 °, and smaller ones at higher angles: 57.16 °, 61.06 °, 68.32 °, 71.83 °, 78.61 °, and 88.50 °. The TiO_2 peak at 28.12° was observed in the unshrouded case.

Experiment	Intensity (A)	Working Distance (cm)	Total Gas Flow (slpm)	%Ar	%N_2	%H_2	Shroud	Substrate
5	220	5.3	180	45	45	10	No	Graphite
6	220	6.3	180	45	45	10	Yes	Graphite

Table 4-5 Experimental conditions for SPS TiB_2 coatings, with and without a shroud.

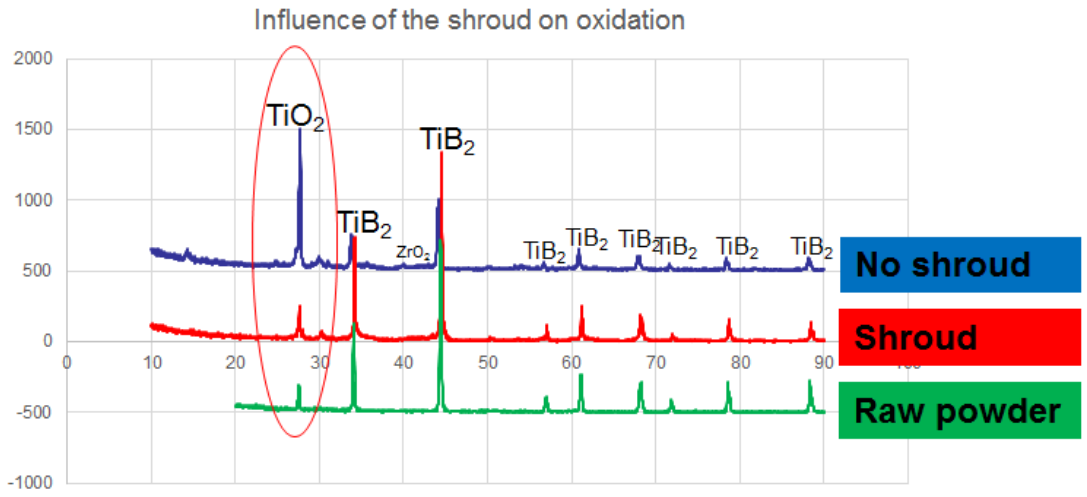

Figure 4-12 XRD spectra of TiB_2 SPS coatings, deposited without shroud (blue-Exp.5), with a shroud (red-Exp.6), and XRD spectrum of the original powder (green).

However, as the XRD only shows one peak of titanium dioxide, X-ray Photoelectron Spectroscopy (XPS) was used to obtain a more in-depth analysis. Both spectra in Figure 4-13 exhibit the characteristic peaks of Ti $2p_{3/2}$ of TiO_2 at 458.7 eV and B 1s of B_2O_3 at 192.4 eV. The Ti $2p_{1/2}$ spin-orbit coupled component is also observed at 464.9 eV. However, only the spectrum of the coating made with the shroud exhibits the peaks located at 454.5 eV (Ti $2p_{3/2}$) and 187.5 eV (B 1s) associated with TiB_2 [145]. The corresponding Ti $2p_{1/2}$ spin-orbit coupled component is expected at 460.7 eV, but it is not observable as it falls on the high-binding energy side of the main Ti $2p_{3/2}$ peak of TiO_2. In the XPS spectra below, the curve for Ti associated with O is weaker in the shrouded coating than in the unshrouded coating, confirming what was seen on XRD and providing more details. The presence of the peaks associated with TiB_2 in the shrouded coating reveals that the top oxidized layer is thinner in this case, as the depth of analysis of XPS is a few nanometres: the shroud has been efficient in reducing the oxidation of the coating, resulting in a thinner top oxidized B_2O_3+TiO_2 layer.

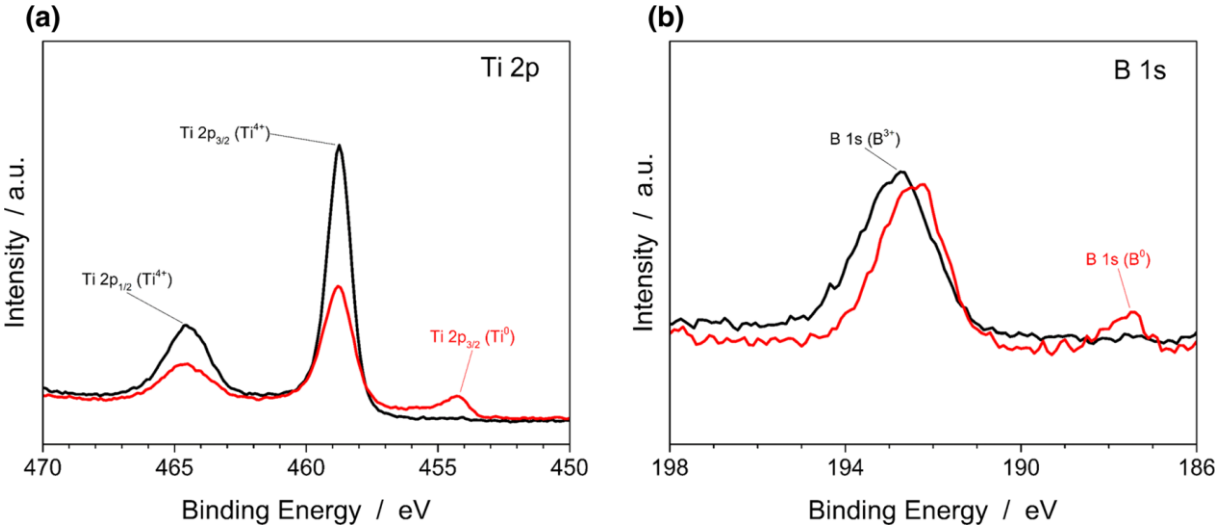

Figure 4-13 XPS Ti 2p (a) and B 1s (b) spectra of TiB_2 coatings prepared with a shroud (red line) and without shroud (black line).

4.3.2. Kinetics of wettability

Another interesting aspect is the influence of the amount of oxidation on the aluminum wettability of the coatings. When measuring the wettability of our coatings by molten aluminum, differences were observed in the kinetics of wettability.

As seen in Figure 4-14, which shows the results of molten aluminum sessile drop tests on SPS TiB_2 coatings, the contact angle of TiB_2 by aluminum reaches a much lower value in both the shrouded and unshrouded cases compared to the value on graphite alone [146]. However, the kinetics of wetting are different. In the shrouded case, the low value is reached faster than in the unshrouded case: in half an hour instead of five hours. This is attributed to the fact that the aluminum first needs to reduce the oxide layer before wetting the boride. Additionally, due to the high porosity of both coatings, they act as sponges and absorb a lot of aluminum. Thus, we observe a sharp decrease quite early, which corresponds to the liquid aluminum percolating through the porous coating, including its cauliflower-like structures. This phenomenon of oxide reduction by molten aluminum delaying spreading kinetics has already been observed by Weirauch et al. [48] and by Heidari et al. [147]. The reduction of TiO_2 and Al_2O_3 is feasible under the conditions of the sessile drop test, at 1000 °C, according to the following reactions with data determined using HSC Chemistry 8 software:

$1.5\ TiO_2 + 2\ Al = 1.5\ Ti + 2\ Al_2O_3$ $\quad\quad$ $\Delta G_r(1000\ °C) = -200\ kJ$

$B_2O_3 + 2\ Al = 2\ B + Al_2O_3$ $\quad\quad$ $\Delta G_r(1000\ °C) = -309\ kJ$

As the coatings obtained with and without shroud have a similar microstructure, it can be concluded that it is the chemical state of the surface of the coating that affects the kinetics of wettability: the oxide layer slows down the aluminum wetting kinetics.

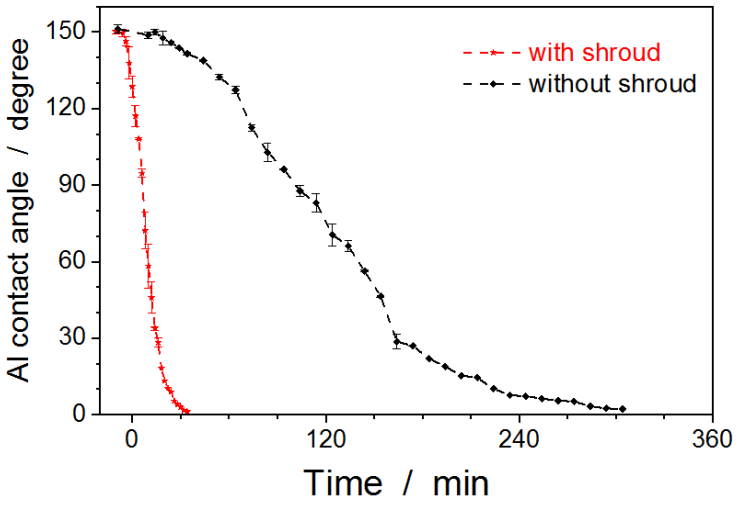

Figure 4-14 Aluminum wettability of TiB_2 SPS coatings, deposited with shroud (red curve), and without a shroud (black curve).

As shown in Figure 4-15 below, molten aluminum percolates through the entire porous coating and reaches the interface, in agreement with what was deducted from the rapid and extremely low wetting angle observed in Figure 4-14. From Figure 4-15d, we observe that Al tends to accumulate at the interface, which could lead to the formation of the brittle Al_4C_3 phase [148]. The formation of this phase is already one of the driving mechanisms of cathode deterioration in the Hall-Heroult process. However, no delamination is observed across the section shown in Figure 4-15, suggesting good adhesion of the SPS TiB_2 coating to the graphite substrate. On Figure 4-15e, we also observe that the YSZ pollution seems to concentrate at the interface. This suggests that the YSZ contamination has reacted with molten aluminum and followed it to the interface as it impregnated the coating. A possible mechanism is that YSZ is reduced by liquid Al to form a liquid Al(Zr) phase. At 1000 °C, the solubility of Zr in molten Al is about 2 wt% [149]. The formation of solid aluminate phases such as Al_3Zr cannot also be excluded. According to the study of [150], aluminothermic reduction of ZrO_2, which generates Zr-Al alloys and Al_2O_3, may occur at 995 °C. The reduction in ZrO_2 by molten Al was also observed at 1000 °C by [151].

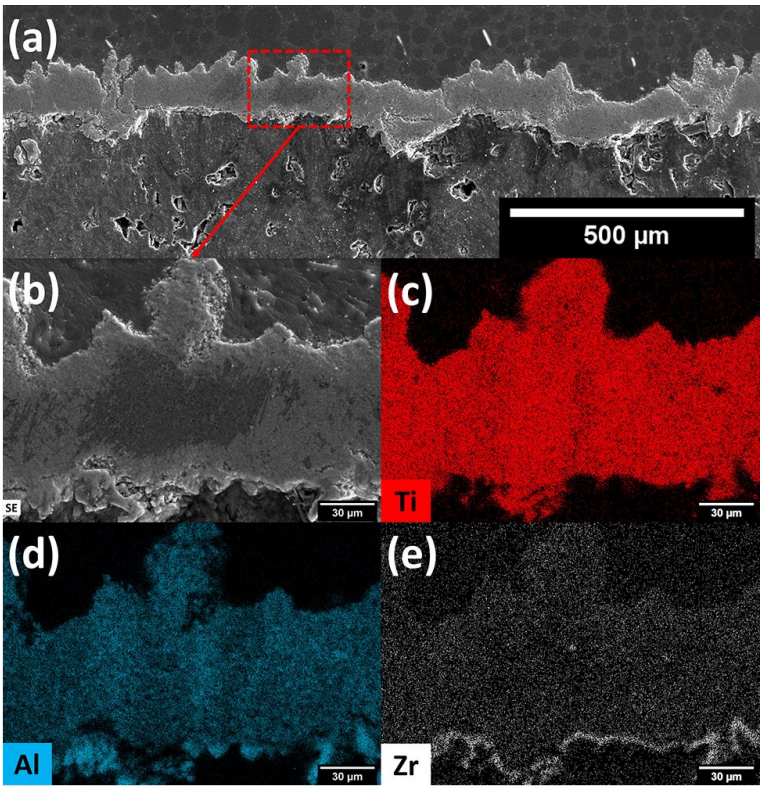

Figure 4-15 Cross-sectional SEM micrographs (a,b) and EDS mapping images of Ti (c), Al (d), and Zr (e) elements as SPS TiB_2 coating made with shroud after 8h of contact with molten Al at 1000 °C (Exp.6).

4.3.3. Mechanical analysis

Scratch test measurements were performed to investigate qualitatively the mechanical properties and adhesion strength of the coating on the graphite substrate. The micrographs of the grooves formed by applying a force of 5 N are shown in Figure 4-16a and b for coatings made with and without a shroud, respectively. In both cases, the stress is accommodated by a homogeneous and irreversible deformation of the coating typical of plastic behaviour. No delamination of the coating from the graphite substrate was observed, even at a 10 N load, confirming the strong anchorage of the deposited layer on the graphite substrate. Figure 4-16c shows that the scratch width increases with the load, but no difference related to the presence or absence of the Ar shroud has been observed.

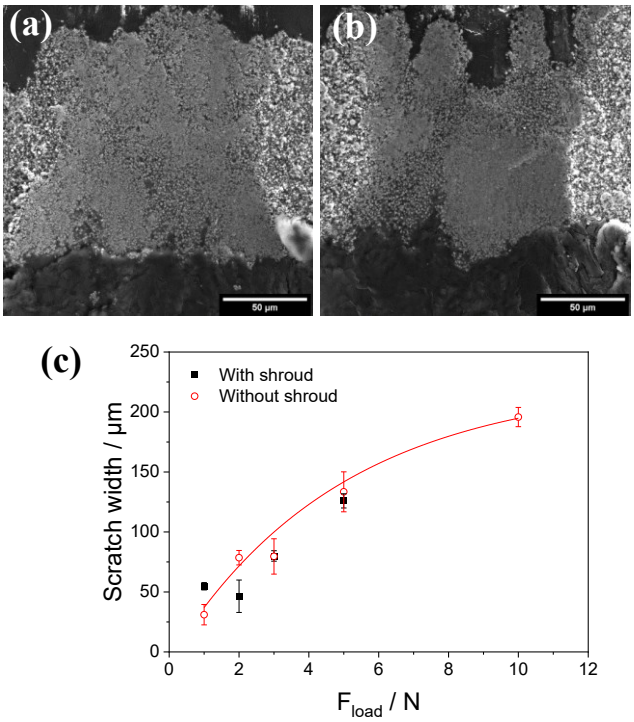

Figure 4-16 Cross-section SEM micrographs of scratch test grooves made at 5 N in TiB2 coatings deposited without (a-Exp.5) and with a shroud (b-Exp.6). Graph (c) shows the evolution of the scratch width applied with the applied load.

4.3.4. B_2O_3 Formation and Cleaning

From Figure 4-17, we observe flaky shapes on top of the coating that are not seen in the bulk of it, after preparing a cross-section. The fact that they are not observable on top of the cross-section suggests that they were likely ground off during the cross-section preparation process. EDS analysis indicates that it is an oxide phase, which was already the main hypothesis from SEM observation, as these shapes appear much brighter than the coating underneath because they are charging. As the EDS mapping reveals no coincidence with Zr or Ti, it is safe to assume that it is B_2O_3, boron oxide.

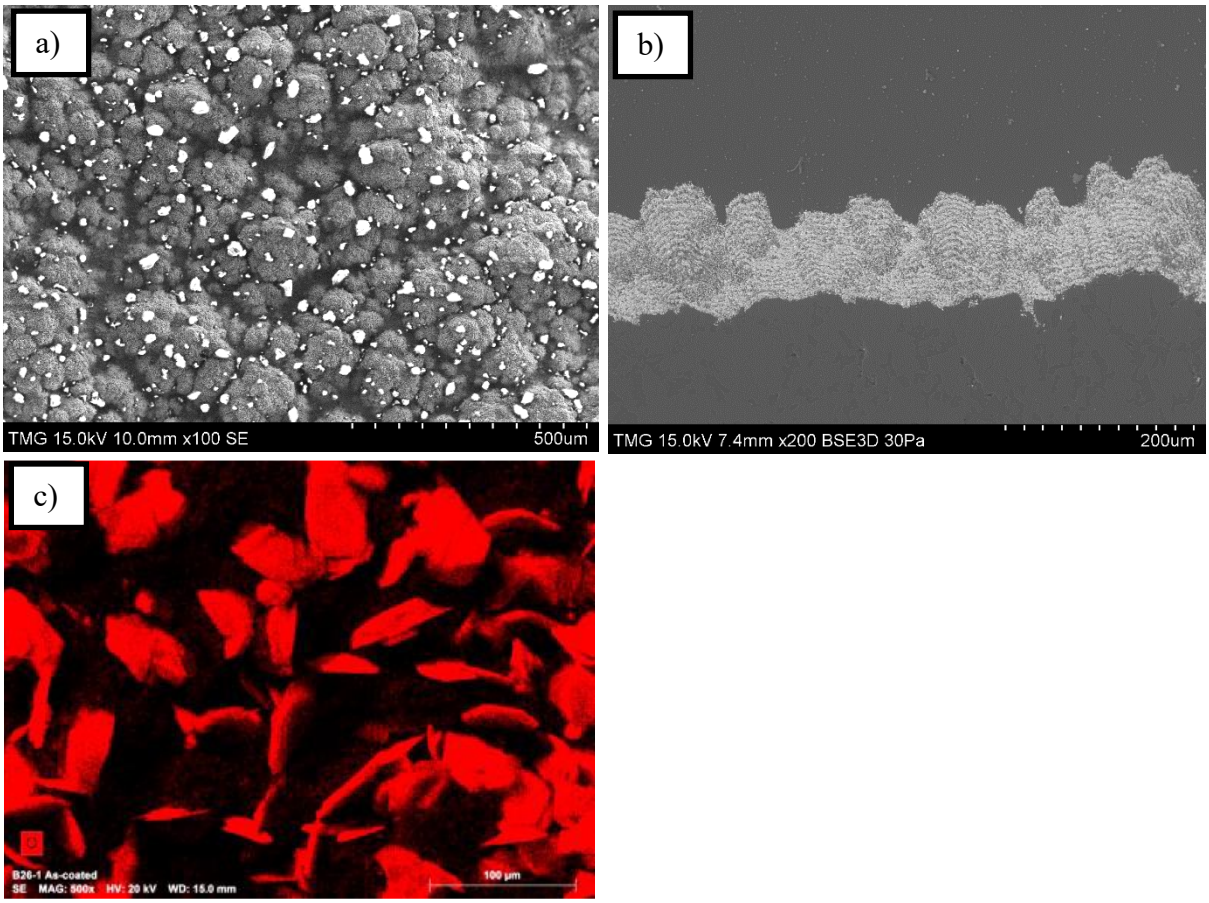

Figure 4-17 SEM micrograph of the top view (a-x100) and the cross-section (b-x200) of an SPS TiB_2 coating, with an EDS mapping of oxygen on the top surface (c-x500).

The formation of boron oxide was expected, as it is the first oxide formed upon high-temperature oxidation of TiB_2 [88]. To be more precise, one can observe the model proposed in [152] for the mechanisms of zirconium boride oxidation, which can be adapted to titanium diboride oxidation shown in Figure 4-18 below. At low temperatures below 1000 °C, a columnar TiO_2 forms, with B_2O_3 forming in between and on top of those columns, as boron oxide is the first oxide to be formed. At intermediate temperatures of 1000°C to 1800°C, boron oxide starts to vaporize. And at high temperatures above 1800 °C, boron oxide completely vaporizes, leading to a more severe oxidation with more TiO_2 being produced. Additionally, boron oxide vaporizes at a temperature above 1200-1500°C [153].

The scenario that is likely to happen is that the TiB_2, when it starts to oxidize in flight, forms an outer layer of B_2O_3 which is then vaporized. During the deposition, this boron oxide vapour follows the gas lines and does not deposit on the coating. However, at the end of the deposition, there is still some B_2O_3 in the air, and as the general temperature decreases rapidly, it solidifies and adheres to the coating.

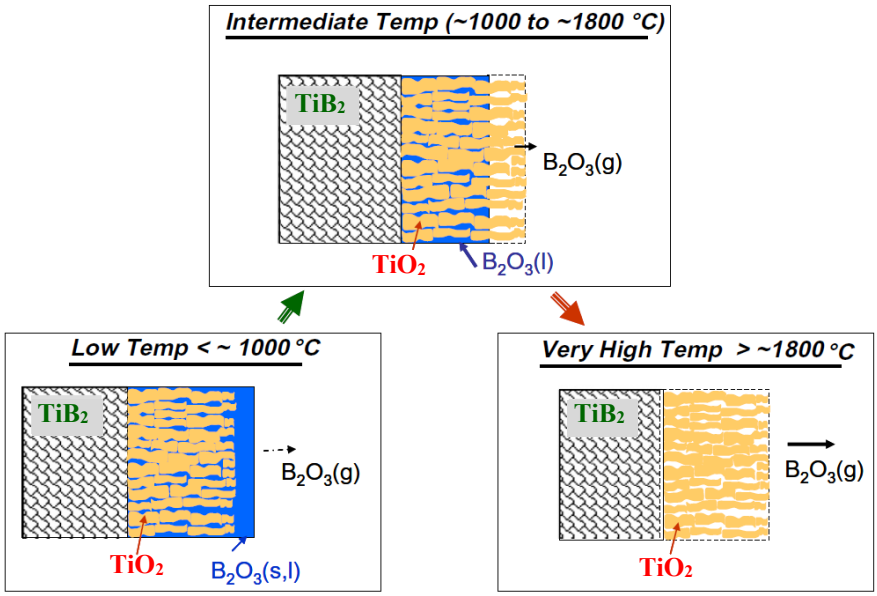

Figure 4-18 The oxidation products formed during oxidation of TiB_2, adapted from [152].

Fortunately, this surface boron oxide is relatively easy to clean away. As observed from [154], boron oxide is dissolvable in water. It dissolves to form boric acid, and at a temperature of 75 °C its solubility in water is 17.41 wt%. Therefore, to eliminate this boron oxide flakes, the following post-treatment can be used:

- Putting the sample in hot water at 70-80°C for one hour,
- Then dry it at room temperature for 48 hours.

As can be observed in the Figure 4-19 below, this post-treatment proved to be very efficient:

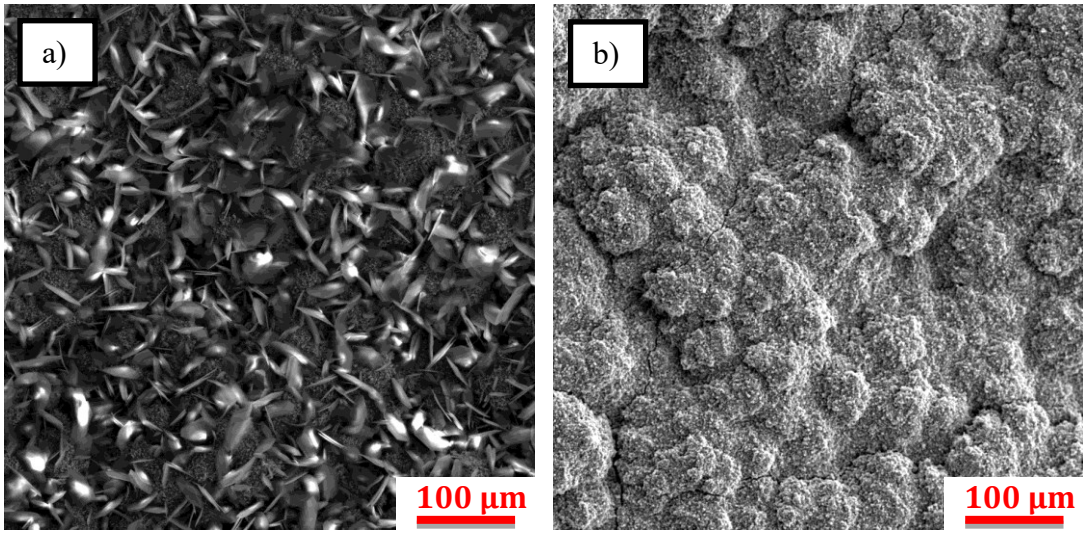

Figure 4-19 SEM micrograph of the top surface of a TiB_2 SPS coating, before (a) and after (b) dissolving B_2O_3 flakes with water.

After 1 hour in hot water at 80 °C, the boron oxide flakes have completely dissolved, and the surface of the coating, with its cauliflower-column shapes, can be observed. Macroscopically,

it also translates into a change in appearance: the sample with boron oxide flakes appears shiny and reflects light, whereas the sample without the B_2O_3 flakes is simply matte grey, the natural colour of pure titanium diboride. This macroscopic observation is an easy way to determine if boron oxide has formed when developing TiB_2 coatings.

Alternatively, mechanically polishing the flakes away has been tried, but this approach did not lead to efficient removal of the boron oxide flakes and resulted in severe deterioration of the rest of the coating. That is mostly due to the relatively porous microstructure of the coating itself, which makes it relatively easy to be polished away.

4.4. Obtaining Tight Coatings

To be used in a Hall-Héroult cell, it is crucial for the TiB_2 coating to be as impermeable as possible to the cryolite. Open porosities would allow the electrolyte to easily percolate to the interface, leading to deformations that could cause rapid delamination of the coating. If the liquid aluminum were to reach the coating/substrate interface, the formation of aluminum carbide could result in even faster delamination. Therefore, the coating should have minimal density and no open porosities to be suitable for this application.

Achieving the desired density was not an easy task at all. Titanium diboride has a high melting point of 2970 °C and a low density of 4.52 g/cm^3, making it difficult to fully melt and reach a dense layer due to its low resilience time in the plasma plume. Several studies were conducted to determine an experimental set of parameters that would allow for a dense coating.

4.4.1. Influence of Stand-off Distance

The stand-off distance refers to the distance between the exit of the torch and the substrate. In our experiments, several stand-off distances were assessed, as shown in Table 4-6 below. The gas shroud was not used in this set of experiments.

Experiment	Intensity (A)	Working Distance (cm)	Total Gas Flow (slpm)	%Ar	%N_2	%H_2
7	220	12	180	45	45	10
8	220	10	180	45	45	10
9	220	7	180	45	45	10

Table 4-6 Experimental conditions for SPS of TiB_2, with varying stand-off distance.

The coatings obtained with the highest stand-off distances (12 cm) were powdery and not cohesive, as did not adhere well to the substrates. This is explained by the fact that when the stand-off distance is increased, so is the time of flight before impact. And the higher is the time of flight, the more important is the cooldown of the particles, leading to re-solidification before impact, and lower mechanical adhesion to the substrate as the particles impact at a

lower speed. A lower particle speed upon impact decreases the mechanical bonding of the particles with the substrate and with each other.

On the contrary, the coatings with the lowest stand-off distance were cohesive and exhibited good adhesion to the substrates. However, it posed a safety issue of properly regulating the temperature and heat flow around the samples and on the sample holder to limit damages during the deposition of titanium diboride. This was addressed by using the minimal stand-off distance possible and cooling down the samples during deposition. Therefore, for further deposition, the stand-off distance was kept at 5.3 cm when the argon shroud was not used, and at 6.3 cm when the Argon shroud was used (5.3 cm of the mechanical shroud + 1 cm of distance outside the shroud).

As seen in the SEM pictures below, even with a low stand-off distance, the coatings obtained were not dense and the particles were intact, not molten upon impact. The total thickness as well as the thickness per pass increased with the stand-off distance: 8.6 µm/pass at 7 cm compared to 12.1 µm/pass at 10 cm. Further work needed to be done to obtain a dense layer.

Another observation from Figure 4-20 is that the higher the working distance, the bigger are the columnar structure. In experiment 7, the average column width was 303 µm. In experiment 8, it was 205 µm. In experiment 9, it was 111 µm. This can be explained by the fact that with increased working distance, the particles have more time to cool down in flight and slow down, impacting at a colder temperature and a smaller speed. The particles are less deformed upon impact, meaning that each impacting particle increases the coating thickness more than if it impacted at a higher temperature and speed. This leads to less mechanical cohesion and a build-up with less physico-mechanical bonding, resulting in more porosity. The larger columns eventually overcome the smaller ones as they grow larger and taller simultaneously, just like the bigger and taller trees are the only ones observable from the top of a forest.

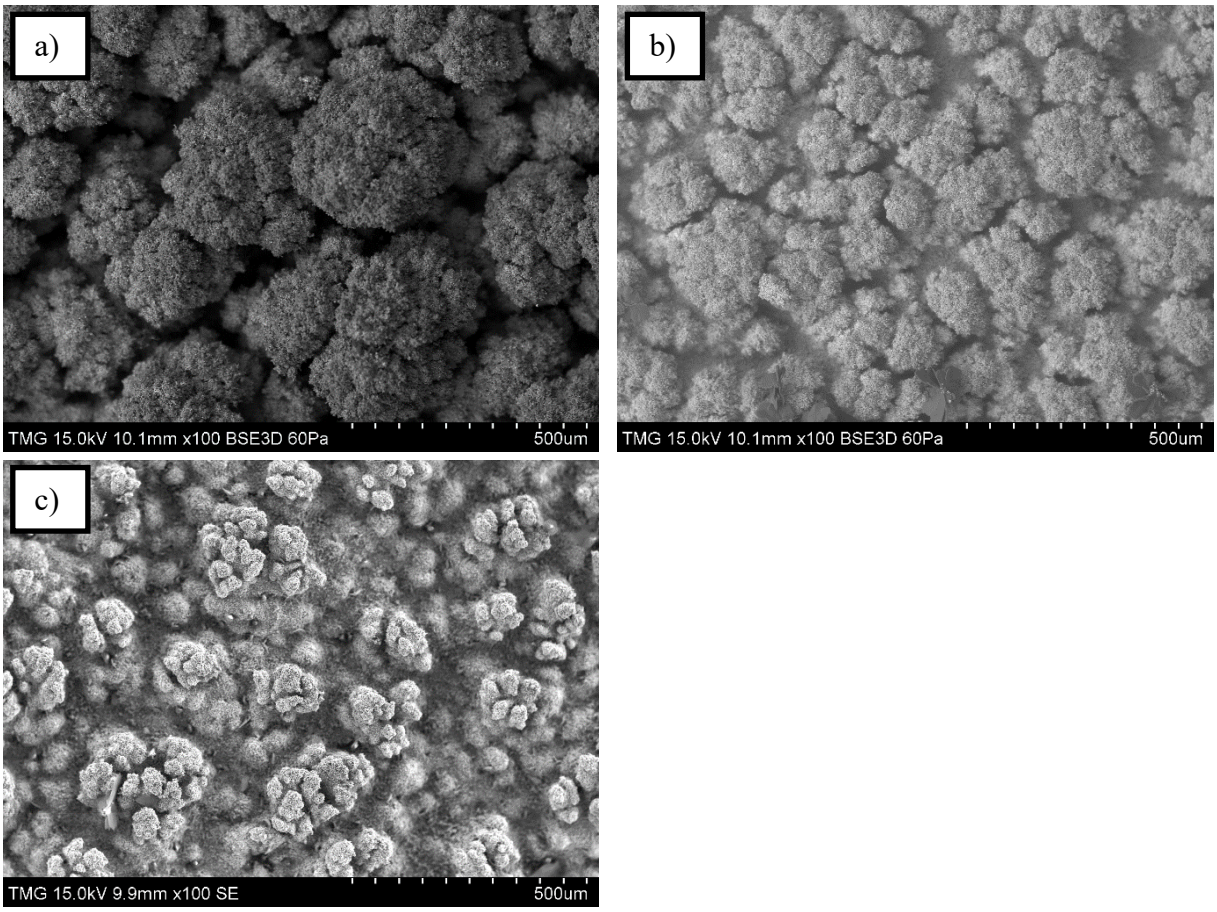

Figure 4-20 Top-view micrographs x100 of SPS TiB_2 coatings deposited with a working distance of 12 (a-Exp.7), 10 (b-Exp.8), and 7 cm (c-Exp.9).

4.4.2. Influence of Power and Plasma Gas Composition

The impact of the power of the torch on the coatings' quality was assessed by varying the current applied between the electrodes, as detailed in Table 4-7. The plasma power results from this current multiplied by the voltage, which itself depends on the plasma gas composition and flow, and the model of the torch used. It was expected that a higher power would lead to denser coatings, as a higher-power plasma means more energy available to melt the particles. In experiment 11, plasma intensity was increased from 180 A to 220 A resulting in a power increase from 85 kW to 100 kW. In experiment 12, the $\%N_2$ of the plasma was increased, resulting in a power reaching the value of 110 kW.

Experiment	Power (kW)	Intensity (A)	Working Distance (cm)	Total Gas Flow (slpm)	%Ar	%N_2	%H_2
10	85	180	5	180	45	45	10
11	100	220	5	180	45	45	10
12	110	220	5	180	30	60	10

Table 4-7 Experimental conditions for SPS of TiB_2, with varying plasma power.

The increased power made it so that there was more heat available to melt the particles. In Figure 4-21, the left micrograph corresponds to experiment 10 and the right one to experiment 11.

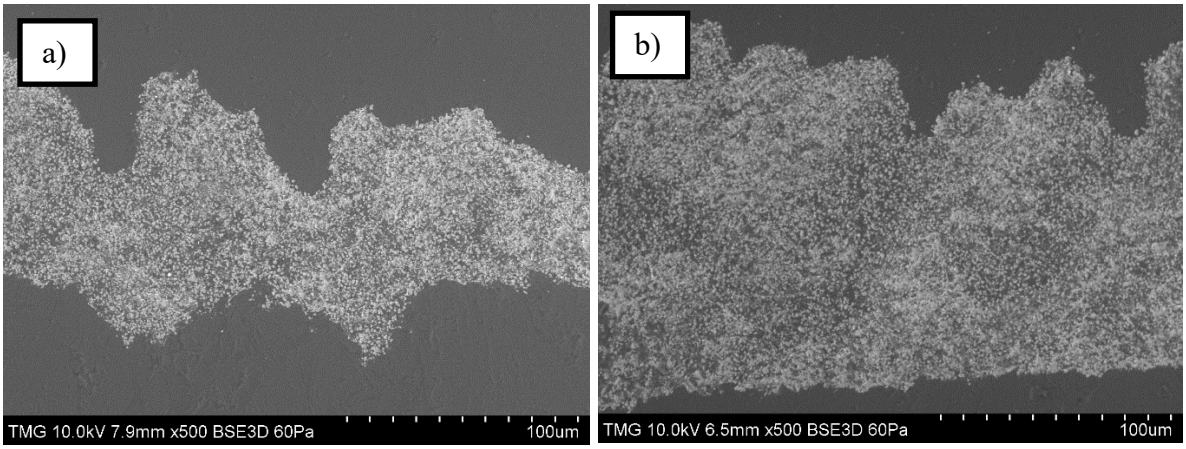

Figure 4-21 Cross-section micrographs of SPS TiB_2 coatings deposited with the plasma of 86 kW (a-Exp.10) and 100 kW (b-Exp.11).

From the micrographs above, there seems to be more areas with flattened splats in the case with a higher-power plasma, characteristic of fully molten particles upon impact. The porosity decreases from 30.94% in experiments 10 to 21.34% in experiment 11. However, that is not yet enough as there are still clearly open pathways across the coating. Also, one can observe that the substrate from Exp.10 has a higher roughness than the one from Exp.11. This is because the study of the influence of the roughness of the substrate on the coating was done after those experiments and at the time, the grit-blasting was not as consistent.

Therefore, to further improve the in-flight melting of the particles by the plasma, the plasma gas composition was changed. A higher percentage of nitrogen was used, as nitrogen has a higher thermal conductivity than Argon, and therefore plasma with a higher amount of nitrogen was expected to transmit more heat to each individual particle.

In addition, as nitrogen is a diatomic gas, it undergoes more reactions upon heating: first and second ionization, but also before that, the dissociation which is in a dynamic equilibrium with the ionizations [155]. Consequently, a higher amount of nitrogen in the plasma also increases the voltage and therefore power of said plasma, further increasing the heat available

to melt the particles. Nitrogen has a higher enthalpy than Argon at the operating temperature of the plasma. It also reduces the velocity of the plasma, leading to a longer dwell time of the particles in the plasma and to better melting. Increasing the hydrogen amount in the plasma could also have been an option, as it is also a diatomic gas and has an even higher thermal conductivity than nitrogen. However, the use of a high amount of hydrogen increases safety issue far more than the use of a high amount of nitrogen.

Analyzing the resulting micrographs in Figure 4-22 confirmed our approach. As expected, the increased N_2 amount in the plasma gas led to better fusion of the particles. The porosity decreased from 21.34% to 13.55%, which was a significant improvement in terms of particles melting and improving density. But still, some parameters could be changed to reach the required lower porosity.

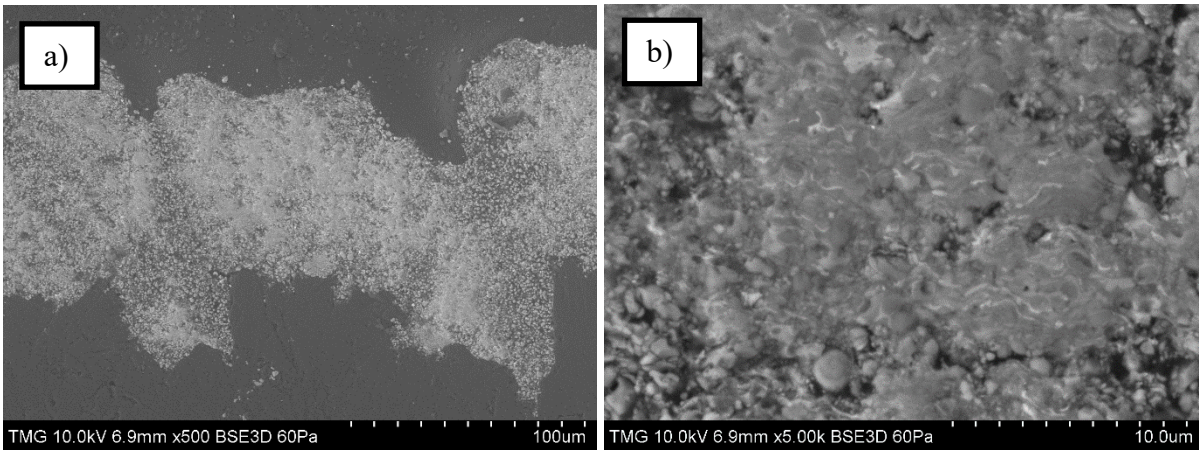

Figure 4-22 Cross-section micrographs of SPS TiB_2 coating deposited with N_2-rich plasma of 110 kW (Exp.12), at low magnification (a-x500) and high magnification (b-x5000).

4.4.3. Influence of Feed Rate

As the conditions established so far are approaching the limit of the system in terms of providing heat to melt the particles, another approach that could be taken would be to decrease the number of particles sent into the plasma per minute. Consequently, that would increase the heat available per particle. Therefore, in experiments 15-16, we reduced the suspension feed rate and the suspension load, respectively. Experiments 13 and 14 are the same as experiments 11 and 12 but done with the gas shroud, hence the 6.3 cm stand-off distance. To properly follow the reduction in actual TiB_2 fed to the plasma, a TiB_2 powder feed rate is calculated from the equation below and indicated in Table 4-8.

$$f_p = f_s \cdot d_{app} \cdot L$$

Where f_s: Suspension feed rate, in mL/min

f_p: TiB_2 powder feed rate

d_{app}: Apparent density of the suspension, in g/cm^3

L: Load of the suspension (in %)

Experiment	Total gas flow (SLPM) Ar/N_2/H_2 (%)	Power (kW)	Working distance (cm)	Suspension feed rate f_s (mL min^{-1})	Suspension load L (wt%)	TiB_2 powder feed rate f_p (g min^{-1})	Coating thickness [m]	Passes
13	180 45/45/10	100	6.3	45	20	7.10	110	30
14	180 30/60/10	109	6.3	45	20	7.10	95	30
15	180 30/60/10	109	6.3	30	20	4.70	80	30
16	180 30/60/10	109	6.3	30	10	2.35	60	50

Table 4-8 Experimental condition of SPS of TiB_2, with varying TiB_2 powder feed rate.

In Experiment 15, the suspension feed rate is reduced from 45 mL/min to 30 mL/min, leading to a decrease in the TiB_2 powder feed rate of 34%. As the heat provided by the plasma is the same in both cases, a 34% reduction in TiB_2 feeding means a 50% increase in heat available per particle. As observed in the micrograph below in Figure 4-23, there was a further improvement in terms of density, which makes sense when we consider the physics involved in the process. The porosity decreased in experiments 15 to 7.86% from 13.55% in experiment 14. It is extremely clear from Figure 4-23b that the particles impact the substrate in a fully molten state. As already mentioned, the brighter spots observed are the ones where the YSZ contamination is concentrated.

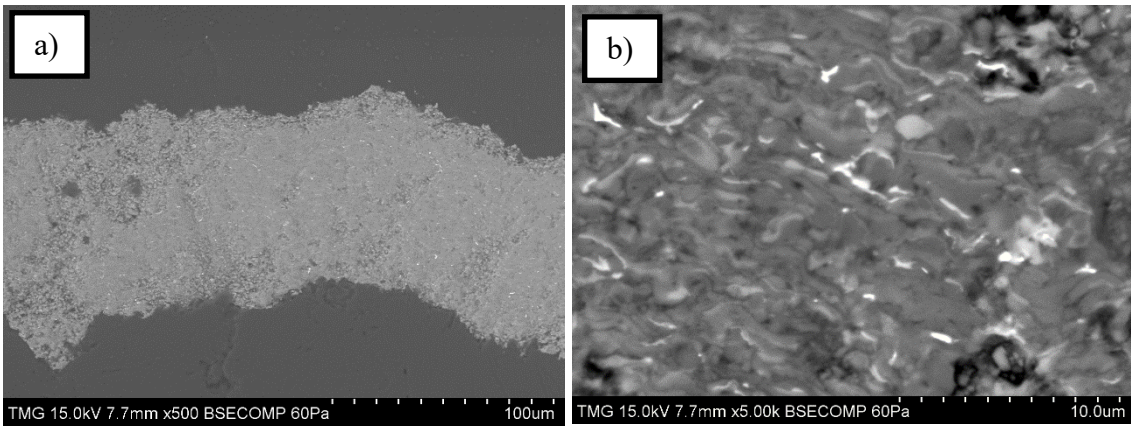

Figure 4-23 Cross-section micrographs of SPS TiB_2 coating deposited with N_2-rich plasma of 110 kW at reduced feed rate (Exp.15), at low magnification [left] and high magnification [right].

4.4.4. Influence of suspension load

Using the same logic as in section 4.4.3, the suspension load, which is the weight percentage of titanium diboride in the injected suspension, can be decreased. As a result, this would reduce the number of particles injected per minute, increasing the heat available per particle. One of the drawbacks to consider when reducing the suspension load, as well as when reducing the feed rate of the suspension, is that it increases the deposition time to obtain a thick coating, consequently increasing the operational cost to run the plasma spraying booth for a longer time. As can be seen in Figure 4-24 below, there was a further increase in density of the coating, which was what we were looking after. However, as observed from the top view of those samples with high density, we observe cracks across the entire coating. These cracks are attributed to the fact that the increase in density reduced the margin available to mitigate stresses through porosities. These increased mechanical stresses, along with the thermal stresses built during the deposition and upon the cooldown of the sample at the end of the deposition, led to fractures upon cooling down. In Figure 4-25 below, three coatings deposited on each other, with the experimental conditions 14, 15, and 16, show the higher density of each coating clearly.

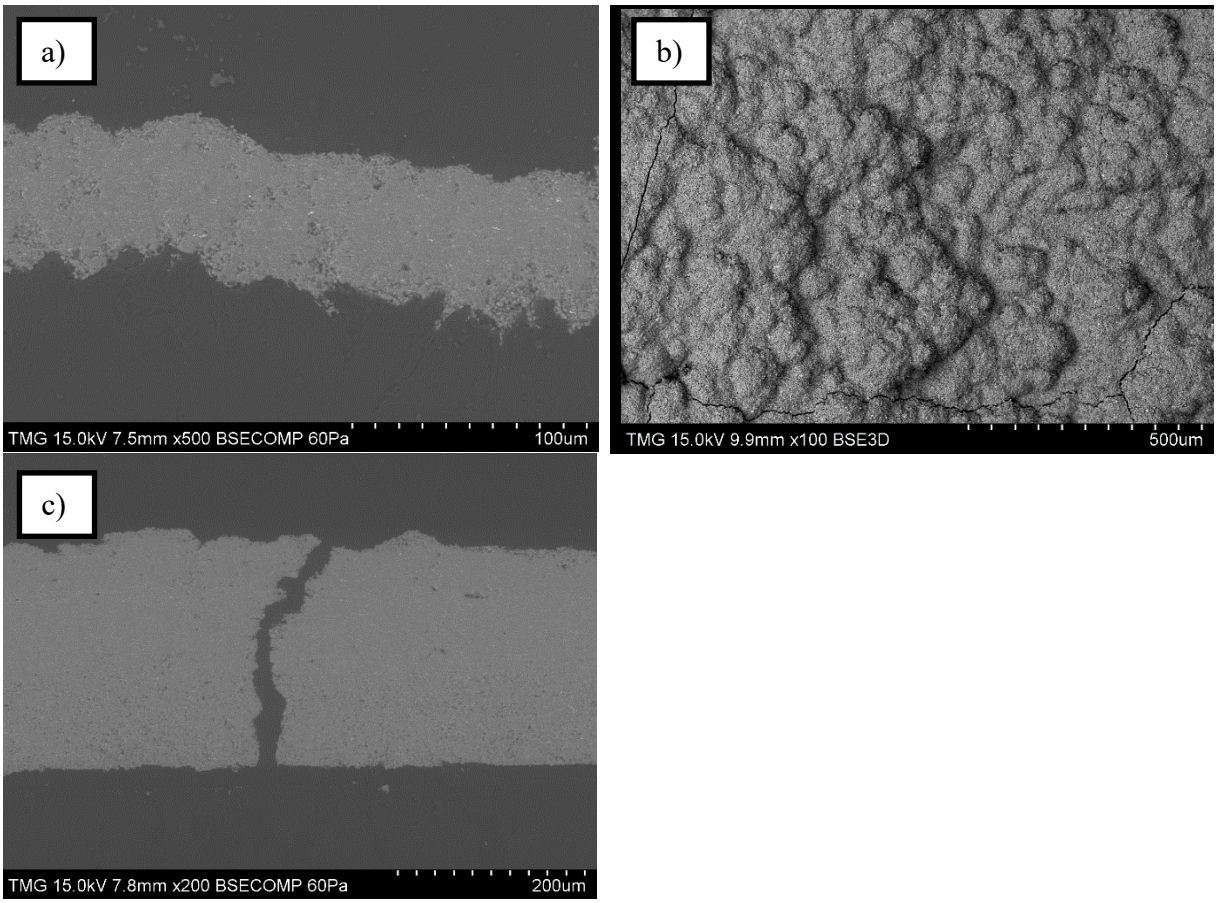

Figure 4-24 Micrographs of SPS TiB_2 coating deposited with N_2-rich plasma of 110 kW at reduced feed rate and reduced suspension load – Exp.16, cross-section (a-x500) and top view (b-x100) and a cracked cross-section (c-x200).

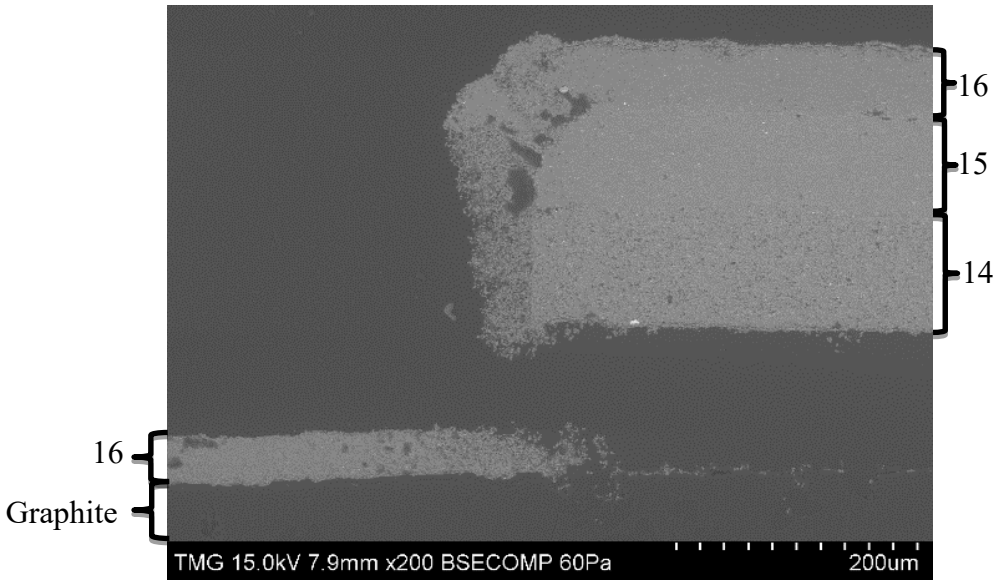

Figure 4-25 Cross-section SEM micrograph of a triple TiB_2 coating, with conditions from top to bottom: 16, 15, and 14.

Additionally, in the figure Figure 4-25 above, one can deduce the history of the coating. The first layer, 14, is thicker and more porous. After cooling down, a new layer is deposited on

top, 15, which is denser and thinner. Then, there is a second cooldown. A delamination happens, with the left section of these two coatings falling off the substrate, and the right section still being connected to it, outside of the image. Then, when depositing the third layer, 16, the densest, and as such the thinnest, we observe it sticks well to the previous layers, as well as to the graphite substrate in the left section, where the previous layers have already delaminated. Obviously, the geometry creates a strong shadow effect that leads to a more porous coating at the rupture of delamination.

As observed in the graph below in Figure 4-26, we were successful in decreasing the originally extremely high porosity of the coatings. The main trend to achieve this has been to improve the heat available per particle, to completely melt them in flight. This has been done first by increasing the heat of the plasma as well as its heat conductivity, and second by decreasing the titanium diboride powder feed rate. We can also notice that in general, the porosity of the coatings obtained with the shroud is lower than the ones deposited without the shroud. This can be explained by the fact that the mechanical piece of the shroud confines the heat of the plasma and, as such, improves the melting of the particles, leading to higher density.

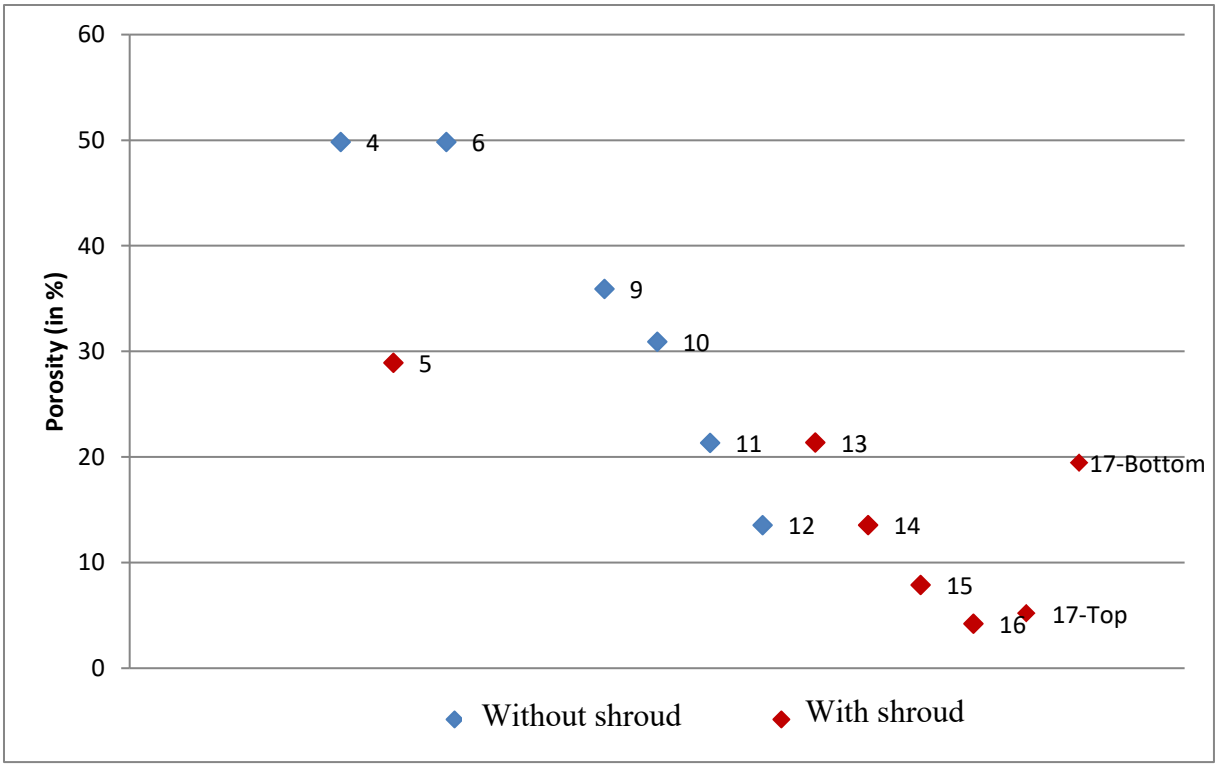

Figure 4-26 Evolution of the SPS TiB_2 coatings' porosity, from experimental conditions 1 to 16.

4.4.5. Impact of cooldown and substrate temperature

In Figure 4-27 below, the red profile corresponds to a setting where the time waited between each pass is longer to keep the substrate temperature relatively low. Each upward

part of the profile corresponds to two passes, which is why there is this small automatic pause in the middle, and the downward parts are the manual pauses between every two passes to ensure the temperature doesn't increase higher. In the blue profile, the first peek at close to 300 °C corresponds to 2 passes of preheating, meaning that we preheat the substrate without yet sending in the suspension. Then, in the same manner, every two passes back and forth are easily identifiable. In the blue profile, the temperature reached was higher, as no pause was implemented between each back and forth. The slight decrease in temperature observed at 4 min 30 is due to the fact the blue profile corresponds to a multilayered coating. This slightly longer pause corresponded to the time required to manually change the deposition parameters to change the porosity of the coating, from the bottom porous layer to the top dense layer. As can be seen on both profiles, the temperature of the samples diminishes at a high speed after spraying, at approximately 5.3 °C/s for the low $T_{substrate}$ case, 8.5 °C/s for the high $T_{substrate}$ case. This fast cooldown is most likely to be at the origin of the thermomechanical stresses that eventually lead to the observed fractures in the coatings.

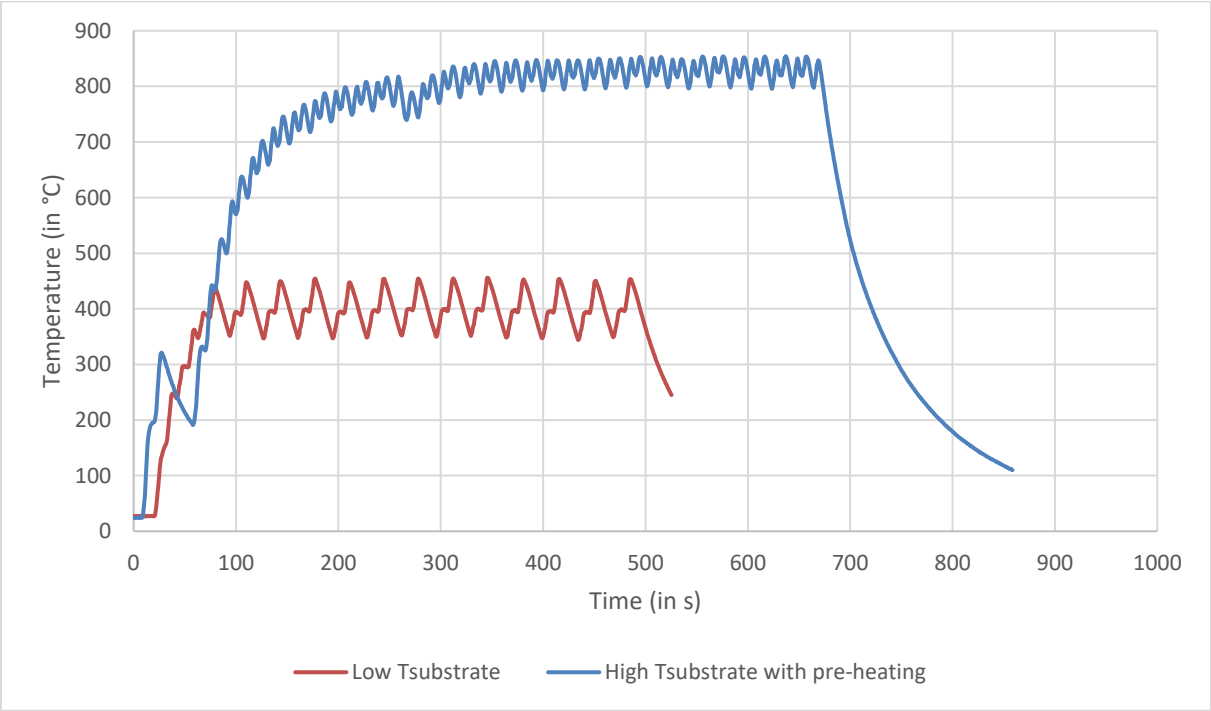

Figure 4-27 Substrate temperature profiles during spraying.

To reduce the build-up of stresses, a better control of the cooldown of samples after deposition could be assessed. Using otherwise the same deposition parameters, a slower cooldown could be put in place. In our experiments, the samples are just cooled down from the airflow in the spraying booth, and reach room temperature in a few minutes, from a temperature of up to 450-850°C during the deposition. To control the cooldown, the suspension feed could be switched off after the deposition, but the plasma torch would be kept on, and at the end of the deposition, passes of the torch in front of the substrates could be made, increasing the time between each pass slowly, to gradually decrease the temperature of

the sample. This would allow for a less harsh build-up of stresses, reducing the possibility of obtaining fractures.

4.5. A multilayer approach

An approach taken to reduce the possibility of cracks and delamination has been a multi-layered approach. This approach has already been implemented in various fields, particularly in the field of electrochemistry, as demonstrated in [156] and [157]. The idea behind using such an approach is illustrated in the scheme below in Figure 4-28:

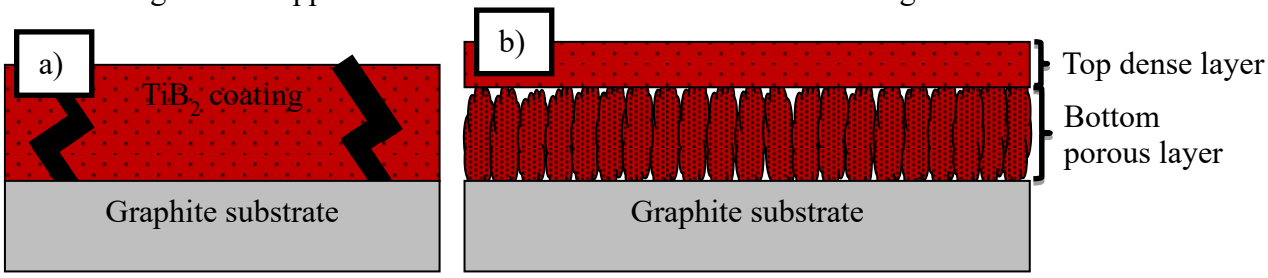

Figure 4-28 Schematics of the multilayer approach. a: Dense layer with fractures. b: Multilayer without fractures as the pores mitigates the stresses.

By first depositing a more porous layer and following it with a denser layer, the aim was to mitigate the build-up of mechanical stresses through the bottom porous layer. The differences in spraying parameters used for the bottom porous layer and the top dense layer were chosen to keep the torch on, avoiding a cooldown between the deposition of one layer and the next, as shown in the table below in Table 4-9. A higher feed rate and a longer stand-off distance were used at first to result in fewer heated particles upon impact, thereby creating a more porous layer initially. Then, the conditions were adjusted back to those used in experiment 16 to obtain a top dense layer.

An additional benefit of using a structure that includes a more porous layer is the expected decrease in thermal conductivity of the coating. The porous layer acts as an insulating region, limiting the propagation of phonons through the coating and thereby reducing its heat conductivity. The number of pores as well as their size distribution will also impact this reduction in heat conductivity. This is positive as it will limit the heat loss from the cell, which is the main source for loss of energy in the Hall-Héroult process.

Experiment	Total gas flow (SLPM) Ar/N_2/H_2 (%)	Power (kW)	Working distance (cm)	Suspension feed rate (mL min^{-1})	Suspension load (wt%)	TiB_2 powder feed rate (g min^{-1})	Coating thickness (m)	Passes
17-Bottom	180 30/60/10	109	8.3	45	10	3.55	65	20
17-Top	180 30/60/10	109	6.3	30	10	2.35	40	40

Table 4-9 Spraying conditions used for the multilayered TiB_2 coating.

The multi-layered approach yielded very promising results, as shown in the micrographs below in Figure 4-29. A bottom layer with higher porosity of 19.45% was obtained, and on top of it, a dense layer was deposited, with a porosity reduced to 5.2%. Additionally, as observed from the top view of the sample, the cauliflower structure was retained, enhancing the aluminum wettability of the coating. The number of cracks significantly decreased, indicating that the approach taken was successful. It was observed that the two layers have a gradient transition. This is attributed to the fact that the impacting particles of the second layer are more molten than those from the first layer and penetrate its porosities. This density gradient at the juncture of the two layers enables the maintenance of good cohesion in this type of multi-layered structure.

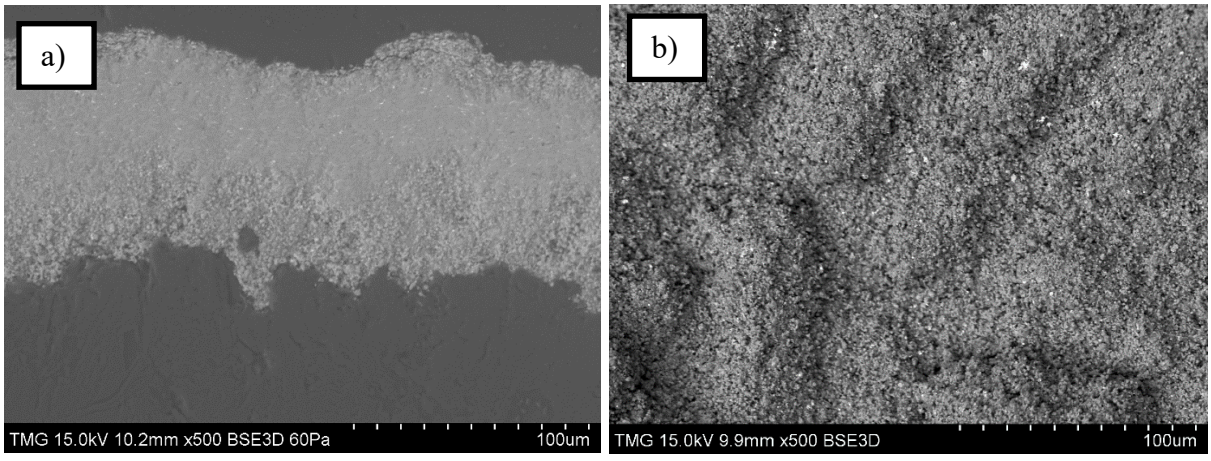

Figure 4-29 Micrographs of the multilayered SPS TiB_2 coating (Exp.17), cross-section [left] and top view [right].

As observed in Figure 4-29 above, the bottom layer, 65 µm thick, had a porosity of 19%, while the top layer, 40 µm thick, had a porosity of 5%. A series of cross-section SEM micrographs were taken over 1 cm, with a representative example shown in Figure 4-29. As can be observed on the top-view micrograph, the higher percentage of molten particles used to

build up the coating also led to the gradual vanishing of the cauliflower microstructure. In effect, what has been obtained is a functionally graded coating. The porosity gradient allows for increased lifetime and reduced heat conductivity while building thick impermeable coatings.

4.6. Relationship Between Microstructure and Aluminum Wettability

Across sections 4.4 to 4.5, the emphasis was placed on obtaining mechanically coherent, dense coatings. A variety of microstructures have been obtained, and it is important to compare their effectiveness in wetting molten aluminum. Therefore, in this section, we will focus on this specific aspect: the impact of the coating microstructure on its ability to wet molten aluminum, as previously described by us in our published articles [144] [158]. As shown in Figure 4-30 below, the wettability of these coatings by molten aluminum is excellent, with a low apparent contact angle.

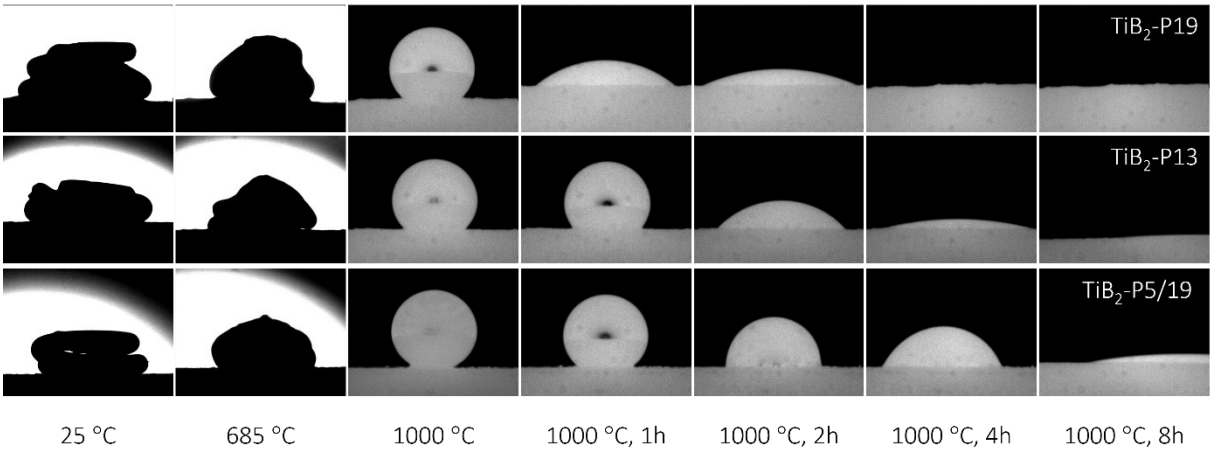

Figure 4-30 Evolution over time of the contact angle of molten aluminum at 1000 °C on coatings with high porosity (first line), medium porosity (second line), and on the multilayered coating (third line).

The sessile drop test displayed above in Figure 4-30 reveals a similar behaviour as observed in the previous coatings in Section 4.3.2. In the 19% high porosity and 13% medium porosity tests, the aluminum droplet wets completely and seems to be absorbed by the coating in 4 and 8 hours, respectively. However, in the 5%/19% multilayered coating, even after 8 hours, the droplet has not been completely absorbed by the coating. Slower kinetics of wetting are also observed with increasing density of the top layer of the coating.

In Figure 4-31 below, showing the EDS mappings of samples of several porosities after sessile Al drop tests, three layers are observed: aluminum, TiB_2 coating, and graphite substrate. In the case of a), the most porous one, aluminum has almost completely permeated through the TiB_2 layer, acting as a sponge for molten aluminum. Large Al-rich regions formed at the interface with the substrate, leading to partial delamination. In case b), there was an observable thick layer of aluminum on top of the coating, yet some of the aluminum

did penetrate through the coating, and small Al-rich regions formed at the substrate-coating interface. Case b) is an intermediate case, as no delamination was observed. In the case c), a multilayered approach was taken, and we can observe that the molten aluminum did not permeate through the TiB_2 coating. In that case, no Al-rich formation was observed at the interface, and no cracks or delamination was observed. The Al-rich regions are likely to be zones of formation of Al_4C_3, which in a Hall-Héroult cell, will lead to delamination of the coating and aging of the cathode.

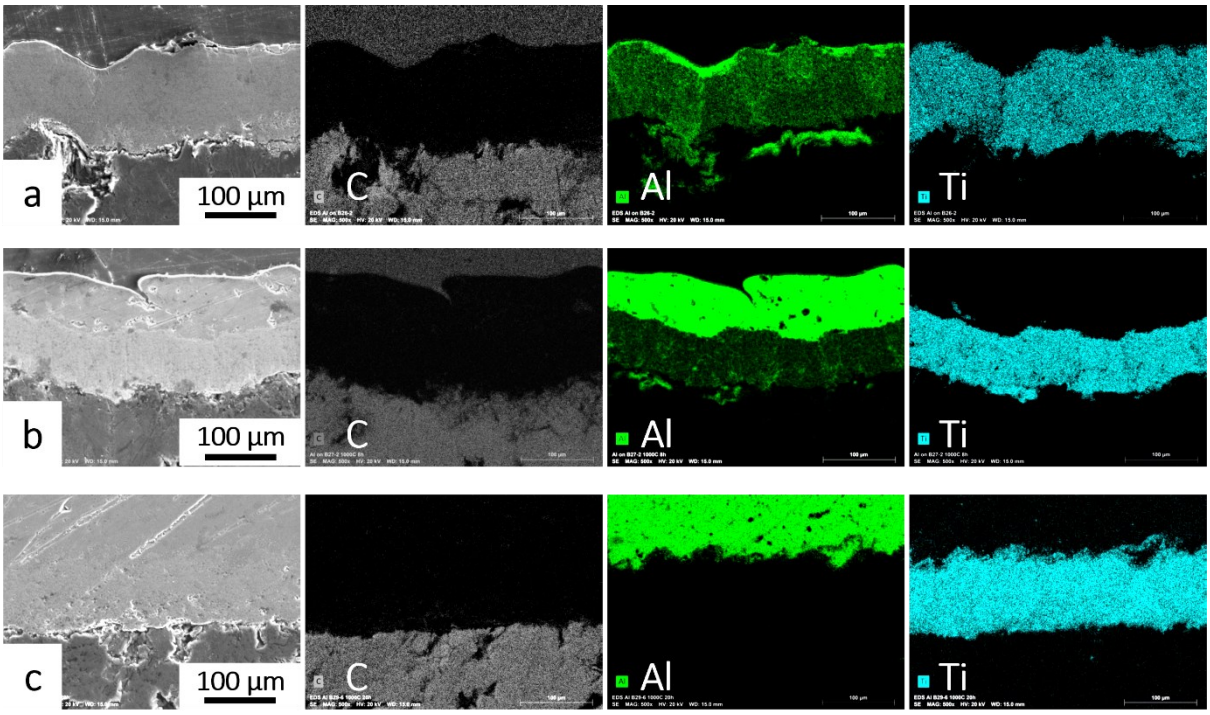

Figure 4-31 Cross-sectional SEM images and corresponding elemental C, Al and Ti EDS maps of a) TiB_2 coating with high porosity, b) TiB_2 coating with medium porosity, and c) TiB_2 multilayered coating after sessile drop tests at 1000 °C for 8h.

In Figure 4-32 below, the different kinetics of wettability of TiB_2 coatings of various porosity, and of graphite, by molten aluminum are shown. As known from the literature, liquid aluminum does not properly wet graphite, with a contact angle barely reaching 75° after eight hours. In the case of high and medium porosity, the infiltration of the molten aluminum through the pores of the coating explains the rapid drop in contact angle that occurs early in the experiment, in the first two hours. In the multilayered case, since the top layer is dense enough to avoid significant rapid penetration of the molten aluminum as observed in Figure 4-30, the kinetic of wetting is slower. Yet, it does reach a contact angle much lower than that of graphite: 5° versus 75°. This decrease in wetting kinetic is only significant during the cell startup. During its operation, the steady contact angle is reached, and this slower kinetics of wetting is of no industrial relevance.

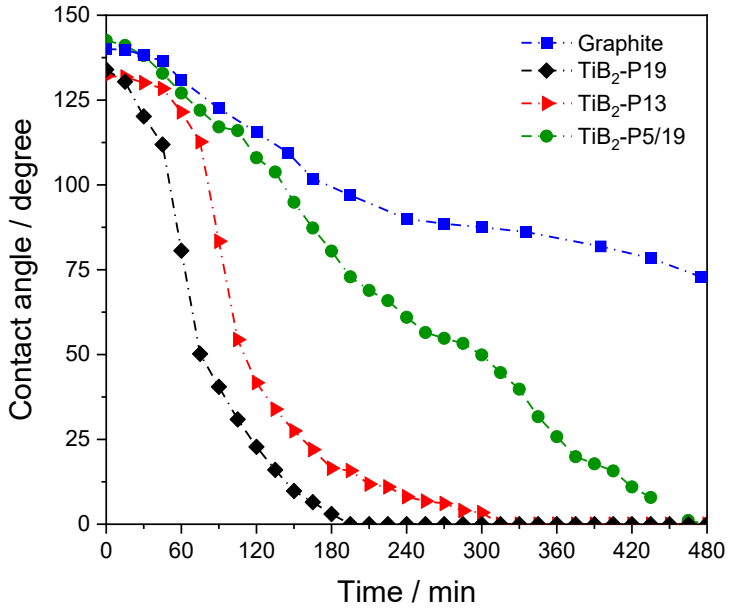

Figure 4-32 Evolution over time of the contact angle of molten aluminum at 1000 °C on graphite, and coatings with varying density.

4.7. Evolution of the Deposition Efficiency

An important factor to evaluate for the later industrialization of this plasma-sprayed process is its deposition efficiency: that is, how much titanium diboride powder is effectively deposited and how much is wasted. This Deposition Efficiency, or DE, can be measured with the equation below:

$$DE = \frac{m_{exp}}{m_{th}} \quad with \quad m_{th} = \frac{N \cdot f \cdot t}{v}$$

With m_{exp}: Mass of material experimentally deposited, measured by weighing the samples before and after the deposition, in grams

m_{th}: Theoretical mass expected, calculated from the deposition parameters, in grams

v: Robot speed, in m/s

N: Number of passes of the plasma torch on the substrate

f: Feed rate of solid TiB_2, in g/s

t: Width of the sample to deposit upon, in metres

By calculating this, the DE of all experiments from Chapter 4 can be summarized in the graph of Figure 4-33 below:

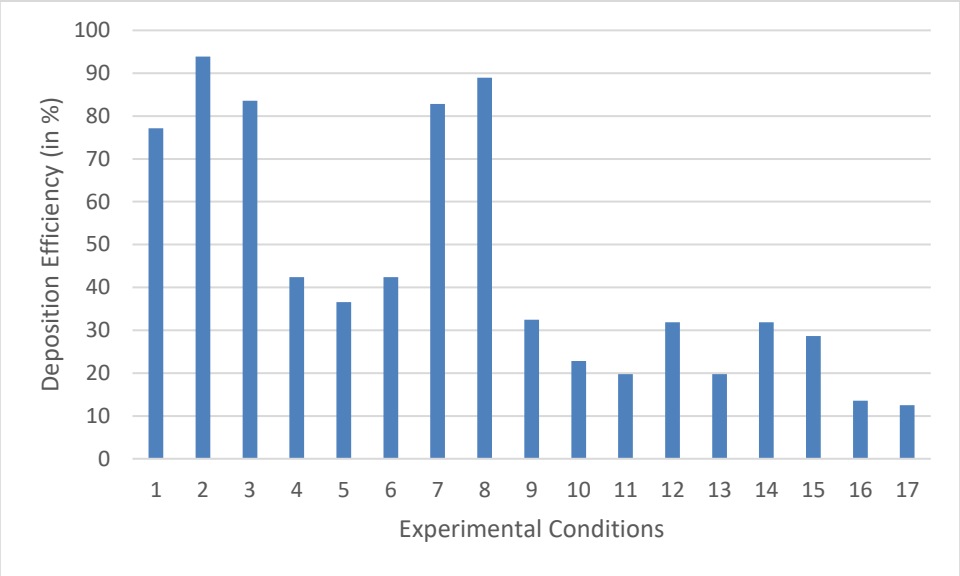

Figure 4-33 Evolution of Deposition Efficiency across the 17 experiments displayed in Chapter 4

Several trends are observable in the graph above. First, it must be noted that compared to typical SPS deposition efficiency, some of these are relatively high, resulting in a thickness/pass deposited up to one order of magnitude higher than usual, in the range of 5-15 µm/pass. The trends observed in Figure 4-33 can be explained by the following physical phenomena:

- A decrease in DE is observed when there are a higher number of unmolten particles upon impact, as those are more likely to follow the streamlines and to not adhere to the coating.
- An increase in DE is observed when using the Argon shroud, as it contains the particles in a more localized area, thereby decreasing their dispersion in the atmosphere. This is also in agreement with literature showing that a shroud gas can keep the particles closer to the torch axis and reduce the entrainment of cold air into the plasma jet [159].
- A decrease in DE is observed when reducing the feed rate, mathematically. However, this decrease is a reasonable cost when compared to the improved density of the coating.

The DE of the multilayered coating, the best coating obtained in this chapter, is 13%. Some directions that could be taken in future work to improve the DE to a more adequate level for industrialization could be using a program with gradient conditions between the porous layer and the dense layer. This would help keep more of the loosely connected particles in the porous layer by having a more progressive change in the depositing conditions.

4.8. Conclusion

In conclusion, in this chapter, several key points of the research have been refined. We have shown that:

- The contamination of TiB_2 by YSZ must be maintained below 5%. A higher contamination greatly deteriorates the corrosion resistance of the coating in the Hall-Héroult cell and has a significant impact on the microstructure. This contamination acts as a binder between the TiB_2 particles in the coating due to its early melting.

- The general microstructure obtained when depositing TiB_2 by SPS is of the wide columnar type and rather porous.

- The substrate must have a TEC (Thermal Expansion Coefficient) close to that of TiB_2 to avoid delamination due to stresses upon cooling after plasma spraying. For this reason, stainless steel is not as optimal a choice as graphite.

- The surface state of the substrate greatly influences the coating's microstructure and surface state. Spots of high local roughness on the substrate will lead to porous columns across the coating. Therefore, when using a soft material as a substrate, such as graphite, the grit-blasting procedure must be properly defined, as it was in our case: alumina grit size of #80, distance of 5 cm, grit-blasting duration of 15s, and pressure of 50 psi or 345 kPa.

- The in-flight oxidation is smaller in SPS compared to APS, with an oxygen percentage reduced to a few percent in the former compared to over 20% in the latter. This can be attributed to the fact that the use of smaller particles reduces their residence time in the plasma, thereby reducing the amount of heat provided to the particles. Consequently, there is a decrease in the percentage of in-flight molten particles. As oxidation primarily happens to liquid particles, in these conditions, fewer molten particles result in less oxidation.

- The gas shroud is useful to reduce oxidation, as revealed by the XPS analysis. When a shroud was used, the oxide layer on top of the coating was significantly smaller.

- The amount of oxidation can significantly impact the kinetics of wetting, as the aluminum must first reduce the oxide layer TiO_2+B_2O_3 on the surface before completely wetting the titanium diboride.

- The porosity of the coatings must not exceed a certain value of at least 9%, to avoid complete permeability by aluminum, which would lead to the coating's failure by the formation of aluminum carbide.

- The YSZ contamination reacts with molten aluminum and is brought by it to the coating-substrate interface.

- Mechanical analysis has qualitatively shown good adhesion strength of the titanium diboride coating to the graphite substrate, with apparently no influence of the presence of the shroud on this adhesion.

- In the event of the formation of boron oxide flakes on the coating's surface, those are easily dissolved by a post-treatment in hot water.

- The influence of several parameters on the microstructure has been studied. In particular, the physical properties - high melting point and low density - of titanium diboride made it difficult to obtain dense coatings. It was observed that with a low stand-off distance of 6.3 cm, a high-power 60% N_2-rich plasma, a low total feed rate comprising of a 10% low suspension load as well as a 30 mL/min low suspension feed rate, dense coatings were obtained.

- However, the increase in density came at the cost of a more fragile, fractured coating. This is because the pores that were present previously were able to mitigate the thermomechanical stresses occurring during the cooldown at the end of the deposition.

- To counter this, a multilayer approach was taken to mitigate the stresses built-up in a porous layer, while having a dense layer on top to keep the structure impermeable to aluminum and sodium. This has proven to be a successful approach. The functionally graded coating thus obtained shows the path forward for TiB_2 coatings.

- The Aluminum wettability has proven to be optimal with the multilayered coating, as the Aluminum does not penetrate throughout the coating in this case.

- One of the drawbacks that we underline is the decrease in DE when increasing the density of the coatings.

Chapter 5 Post-processing: 2-Step Laser Deposition

5.1. Laser post-treatment

As detailed in Chapter 4, one of the key aspects of this work has been to attempt to densify the coatings. This was achieved in Chapter 4 by using a porous/dense multilayer approach, tuning the porosity of the coatings gradually to obtain the correct architecture. Another completely different approach to densify the coatings is to use a laser after obtaining the coating, to densify just a layer of the coating, as exemplified in Figure 5-1 . The advantages of using such a technique are the fact that more and more facilities are using high-power laser that could be utilized for this purpose, and also that it would allow for easier repair of the cathode by redoing the post-treatment, assuming the geometry of the Hall-Héroult cell is reworked, which is also something that has been researched by the aluminum community [160].

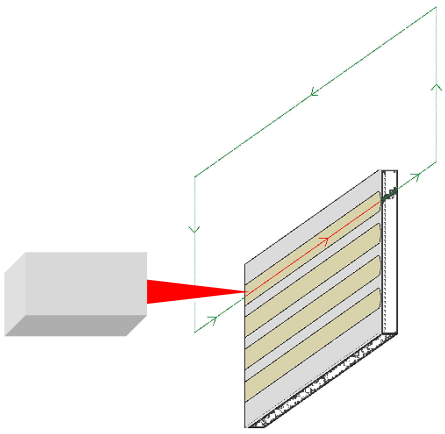

Figure 5-1 Schematic of a laser remelting a surface.

The main impact of the laser post-treatment will depend on the power density and the energy density transmitted to the coating. These parameters are crucial for determining how much energy is transmitted to the coating, and how long each spot receives this amount of energy. To study this, the main parameters studied were the laser power and the robot speed. The spot size of the laser, which could be changed in various manners remained the same in this thesis. For instance, the spot size of the laser could be adjusted by changing the laser-to-sample distance away from the focal distance of the laser.

$$P_d = \frac{4P_{out}}{\pi d^2}$$

$$E_d = \frac{P_{out}}{vd}$$

With P_d: Power density (in MW/m²)

P_{out}: Laser output power (in W)

d: Spot size (in mm)

E_d: Energy density (in J/mm²)

v: Robot speed (in m/min)

One characteristic of TiB_2 to be considered when treating it with a laser is its index of refraction, as it will determine the absorption coefficient, that is, how much energy is absorbed to remelt the coating, versus how much is reflected. Analyzing data from Aouadi et al. [161] and knowing that the wavelength of our laser is λ=1,0701µm, meaning that its energy is:

$$E = \frac{hc}{\lambda} = \frac{6.626 \cdot 10^{-34} \cdot 3 \cdot 10^{8}}{1.0701 \cdot 10^{-6}} = 1{,}1584\ eV$$

This approximately leads to a complex index of refraction of n'= n-ki = 3.68-3.79i when plotted in the appropriate graph from [161].

From here, one can calculate the absorption coefficient $\alpha = \frac{4\pi k}{\lambda} = 44{,}5\ \mu m^{-1}$. The absorption coefficient describes the intensity attenuation of the light passing through the material. The higher the value of α, the shorter the laser can penetrate the material before it is absorbed.

This means that at a depth of $\frac{1}{\alpha} = 23\ \mu m$, the power of the beam is attenuated by a factor of $\frac{1}{e} = 36\%$. It is possible to remelt the top layer of the coating, but the values calculated here show that the window of energy density provided is thin between remelting the coating and cracking it by overpowering the coating.

After depositing SPS coatings using the conditions from experiment 15, a laser post-treatment was applied. By varying the robot speed and the power output of the laser, a vast array of conditions was obtained, and they are shown in the graph below in Figure 5-2 in terms of power density and energy density.

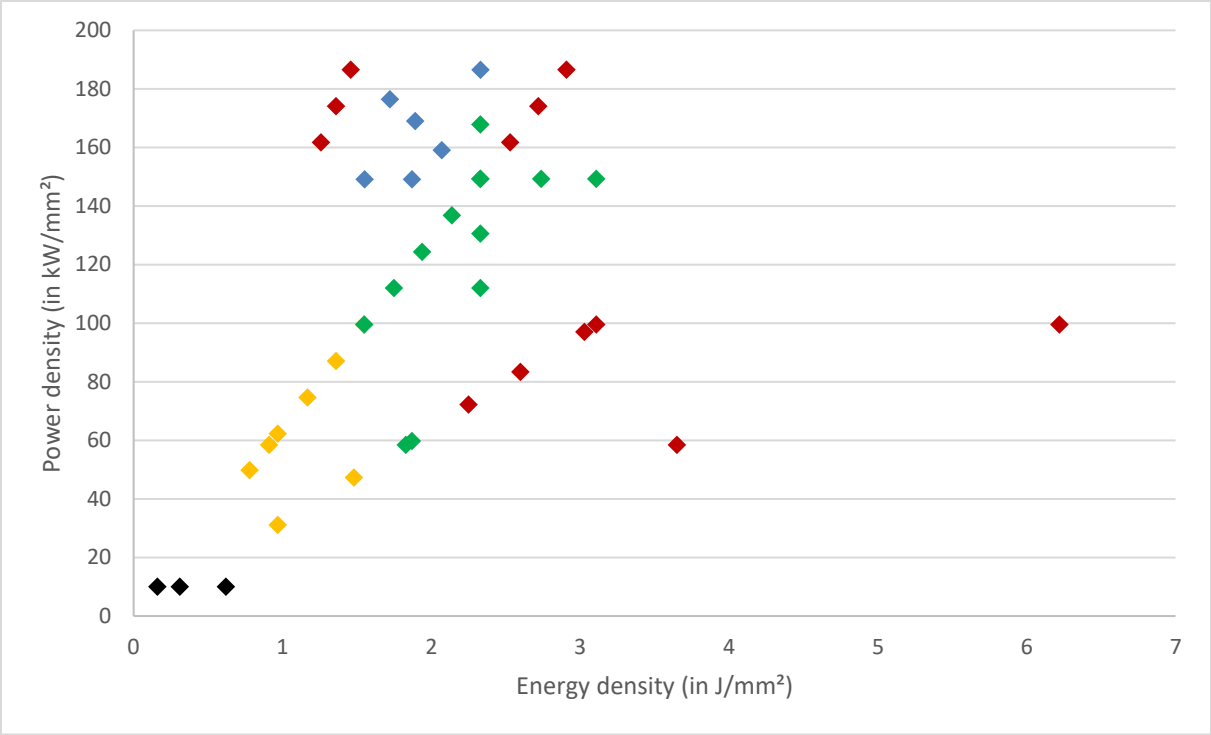

Figure 5-2 Experimental laser remelting conditions expressed in terms of power and energy density.

In Figure 5-2 above, the red dots represent the conditions that led to significant failure and delamination of the laser-treated coating. The black dots represent the conditions where no significant change was observed. The yellow dots represent the conditions where the coatings were affected without being remolten. The green dots represent the window in which the coatings were at least partially remolten. As detailed, each line corresponds to a specific robot speed, with increasing laser power input. For example, in Figure 5-3 below, some catastrophic failures are observed. A change in the colour of the laser-treated lines reveals possible oxidation of the material, which most likely happened as the coating delaminated, significantly increasing the power density in the cracked part.

Robot speed (m/min)	**10**	
Laser Power (W)	Pd	Ed
600	74,6	2,33
700	87,0	2,72
800	99,5	3,11

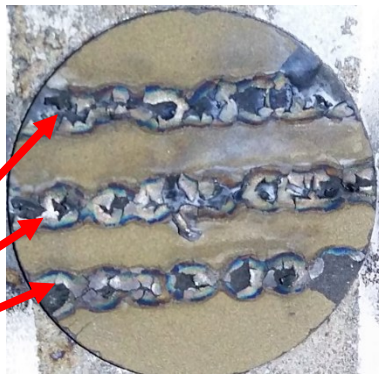

Figure 5-3 Examples of catastrophic failure upon laser remelting of a coating, with the corresponding laser parameters.

Photos of laser-treated samples are shown below in Figure 5-4. One can observe that the window to correctly melt the coating without damaging it into delamination is rather thin. Also, a lack of homogeneity across one line can be observed in several cases, which could be explained by either a lack of the coating's homogeneity or a lack of consistency in the laser stability. Given the stability observed in the laser, and the difficulty observed in previous sections to obtain a homogeneous roughness, it is likely that the homogeneity of the coating is at fault there.

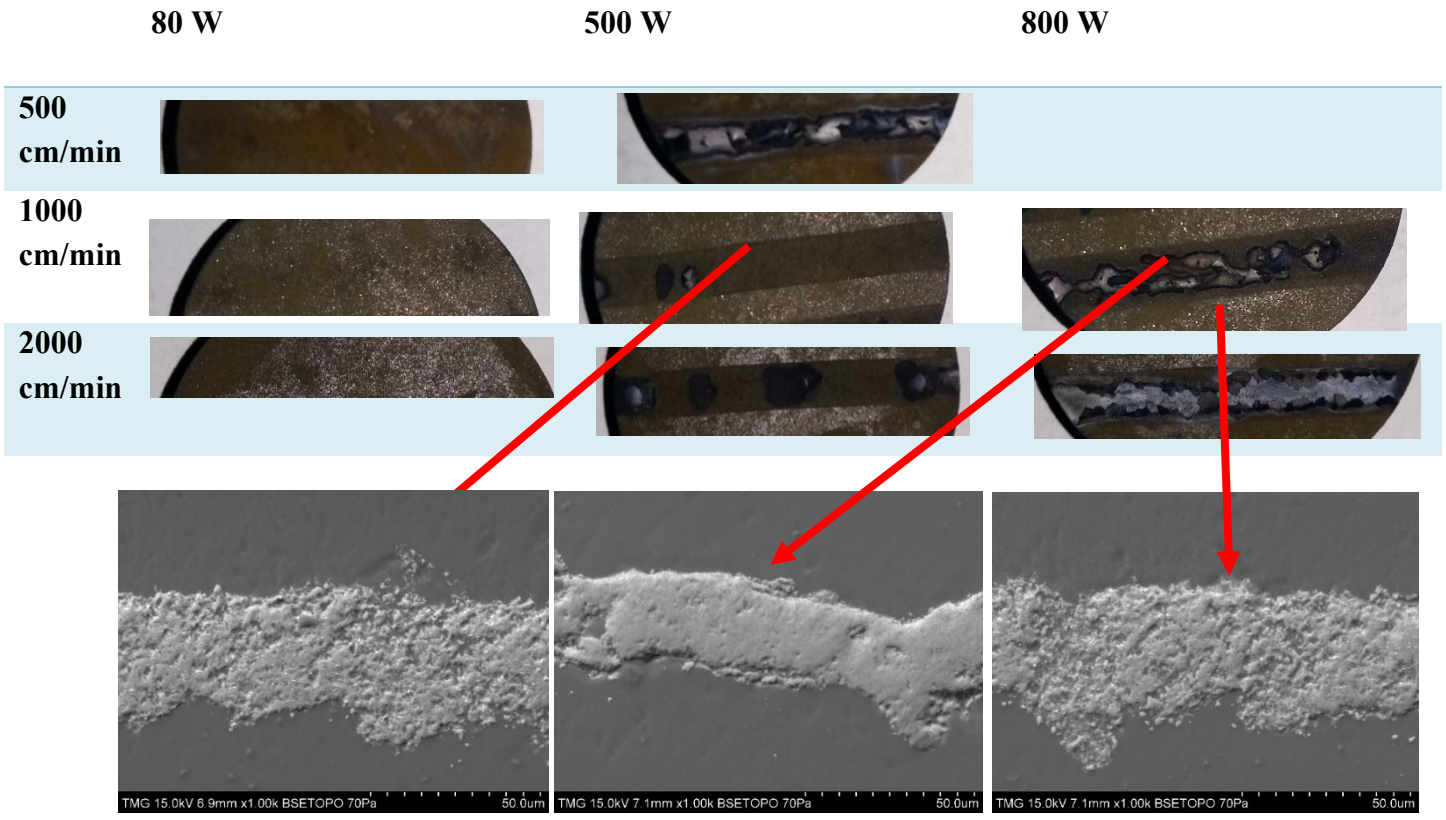

Figure 5-4 Photos of TiB_2 SPS coatings post-treated by laser, along with micrographs of the main observable features.

As can be observed in Figure 5-4 above, when the power density is too low (which come from a low laser output of 80 W), no significant change is observed, macroscopically or microscopically. Upon increasing the power density, a macroscopic observation can be made in that the laser-treated part is not as shiny as the non-laser-treated parts. However, this doesn't translate to a change in microstructure. This is attributed to the fact that this shiny aspect comes from the Boron trioxide flakes observed in sections 4.3.4. It is inferred that the laser might vaporize those flakes or remelt them, causing them to lose this optical aspect through a phase change. Upon increasing the energy and power density further, some full remelting of the coating is observed in Figure 5-4, middle micrograph. However, this comes at the cost of a catastrophic failure of the coating, just as in Figure 5-3.

In the micrographs below in Figure 5-5, one can observe the progression of remelting of the particles. Quantitatively, it translates into a decrease in porosity from 34%(a) to 19%(b) to 13%(c). When the laser power is increased further than 1.2 kW, all other parameters kept at the same value, a failure of the material happens, with delamination as can be observed in Figure 5-5d. The whiter small areas are difficult to analyze with EDS due to their size, but according to our research developed in the previous chapter, they are likely to be oxides, mainly based on the YSZ contamination of the original powder, as well as the low amount of oxidation happening in-flight.

The most promising conditions, as shown in Figure 5-2. When observed under SEM, they show a significant increase in density with full remelting of the coating. However, this is a preliminary study involving simple line scans on the coating, and a pattern must be determined for further research to fully remelt the entire coating.

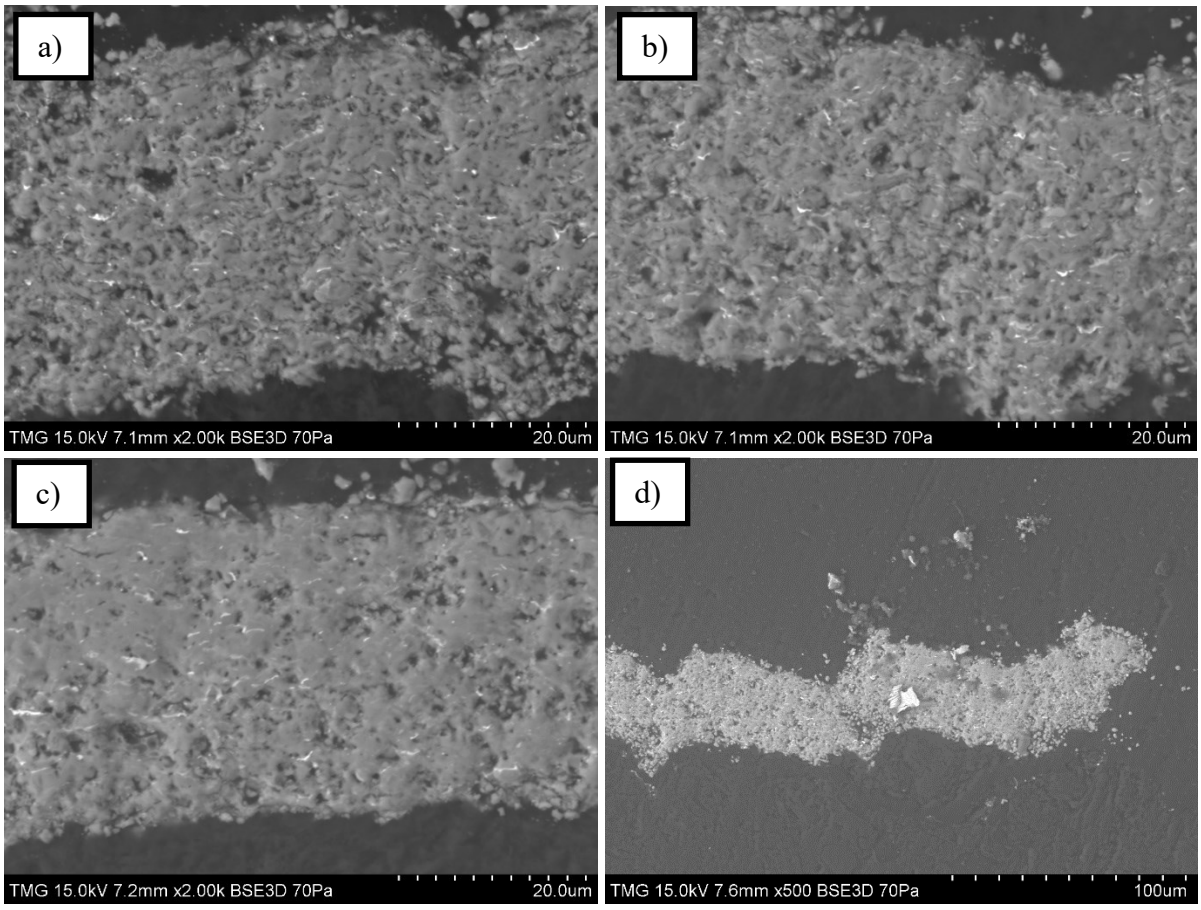

Figure 5-5 Cross-section SEM micrographs of laser-treated SPS TiB_2 coatings with a robot speed of 20 m/min and laser power of 1.0 kW (a), 1.1 kW (b), 1.2 kW (c), and delaminated 1.3 kW (d).

From Figure 5-6, one can observe macroscopic changes in the various laser-treated coatings. Obviously, the edge effect causes fractures and delamination at the edges of the samples. There is also a small inhomogeneity across the line scan: the top and bottom extremities of the laser spot seem to have received less energy, as they is less affected by it, which is clearest on the sample the furthest to the right in Figure 5-6.

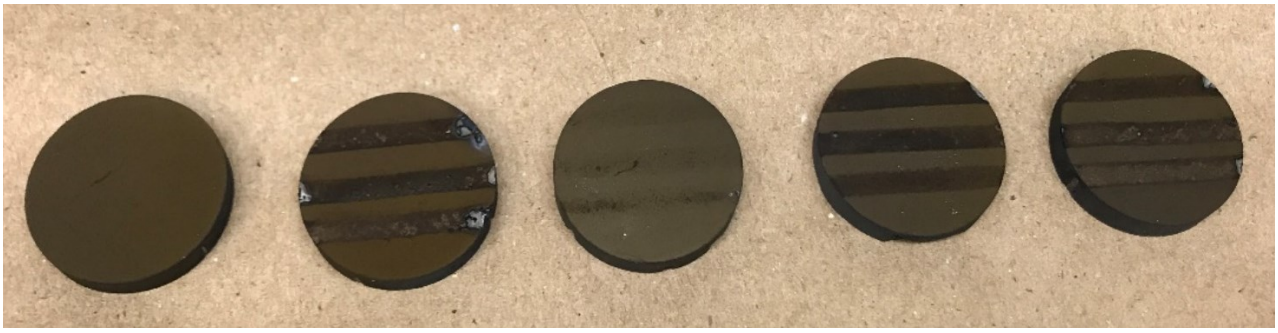

Figure 5-6 Photos of various 2SLD coatings deposited with the conditions specified in Figure 5-2.

As can be observed in the micrograph below in Figure 5-7, macrocracks are visible on the surface of the laser-treated coatings, which is in accordance with the literature showing cracking of laser-treated ceramics [116]. In the cross-section, we can observe a delamination. The part that appears white on the macroscopic level corresponds to a fully dense layer delamination.

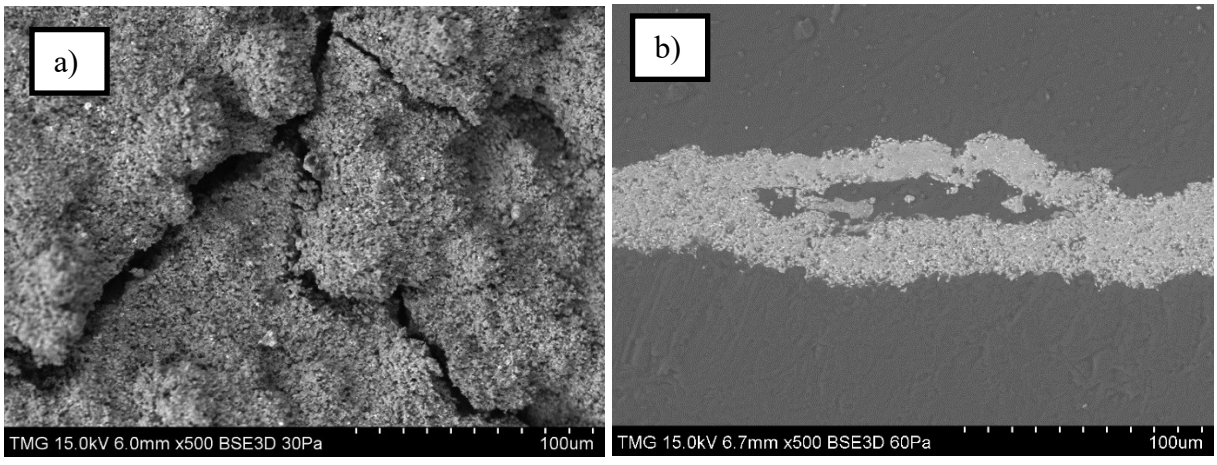

Figure 5-7 SEM micrograph of the top surface of a laser-treated coating, with visible cracks, top surface (left-x500) and cross-section (right-x500).

From Figure 5-8, we can observe that at constant energy density, increasing the power density does not result in a significant change in the microstructure of the coatings. On Figure 5-9, we can observe a catastrophic failure at low energy density, and a slight increase in density at higher energy density without catastrophic failure.

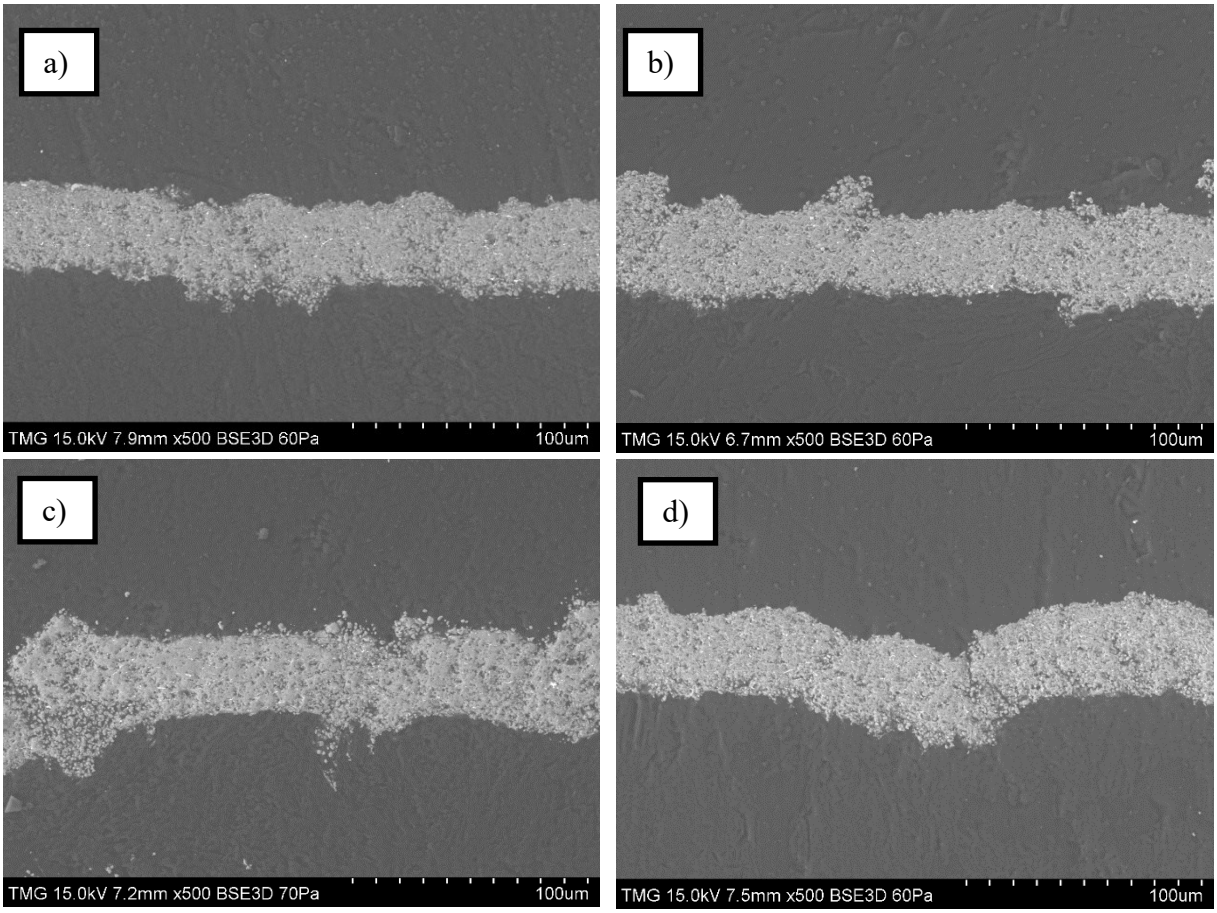

Figure 5-8 SEM cross-section micrographs of 2SLD coatings with corresponding photo, at constant Energy density of 2.33 J/mm ^{2}, and with increasing power density of 111.9 (a), 130.6 (b), 149.2 (c) and 167.9 (d) kW/mm ^{2}.

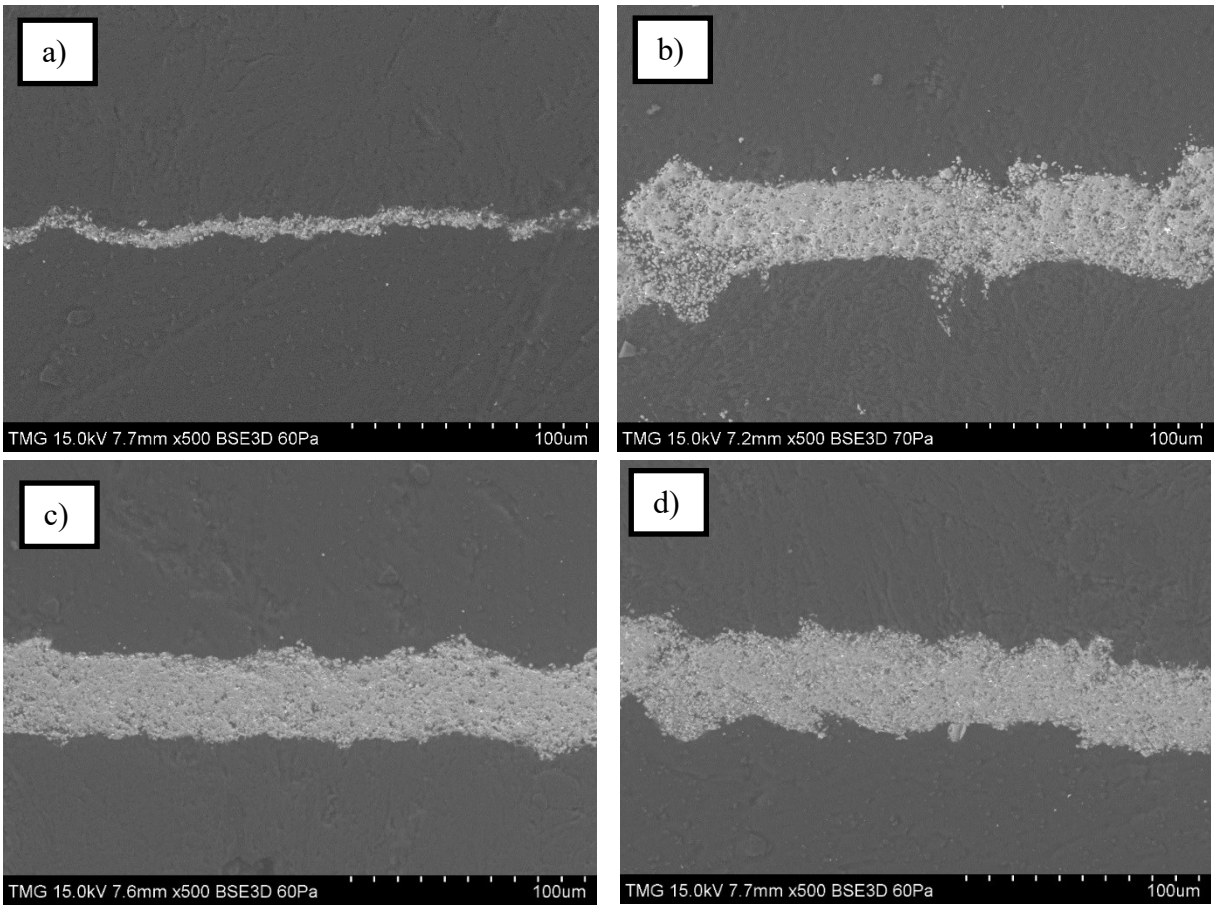

Figure 5-9 SEM cross-section micrographs of 2SLD coatings with corresponding photo, at constant power density of 149.2 kW/ mm ^{2}, and with increasing energy density of 1.87 (a), 2.33 (b), 2.74 (c) and 3.11 (d) J/ mm^2.

As can be observed in the graph in Figure 5-10 below, the use of a laser post-treatment has proven to be successful in reducing the porosity of the coating, by approximately 10%, from a value close to 25% to one closer to 14%. Yet, the main change proves to be structural, as shown in the micrograph below: the as-sprayed coating exhibits a local microstructure characteristic of the SPS technique, with distinct layers corresponding to each pass. Whereas the laser-treated coating exhibits a re-molten microstructure, where this distinction has disappeared. This is likely to improve the impermeability of the coating to the electrolyte, as well as the mechanical cohesion of the coating itself, as it is an external manifestation of a stronger local physical bonding.

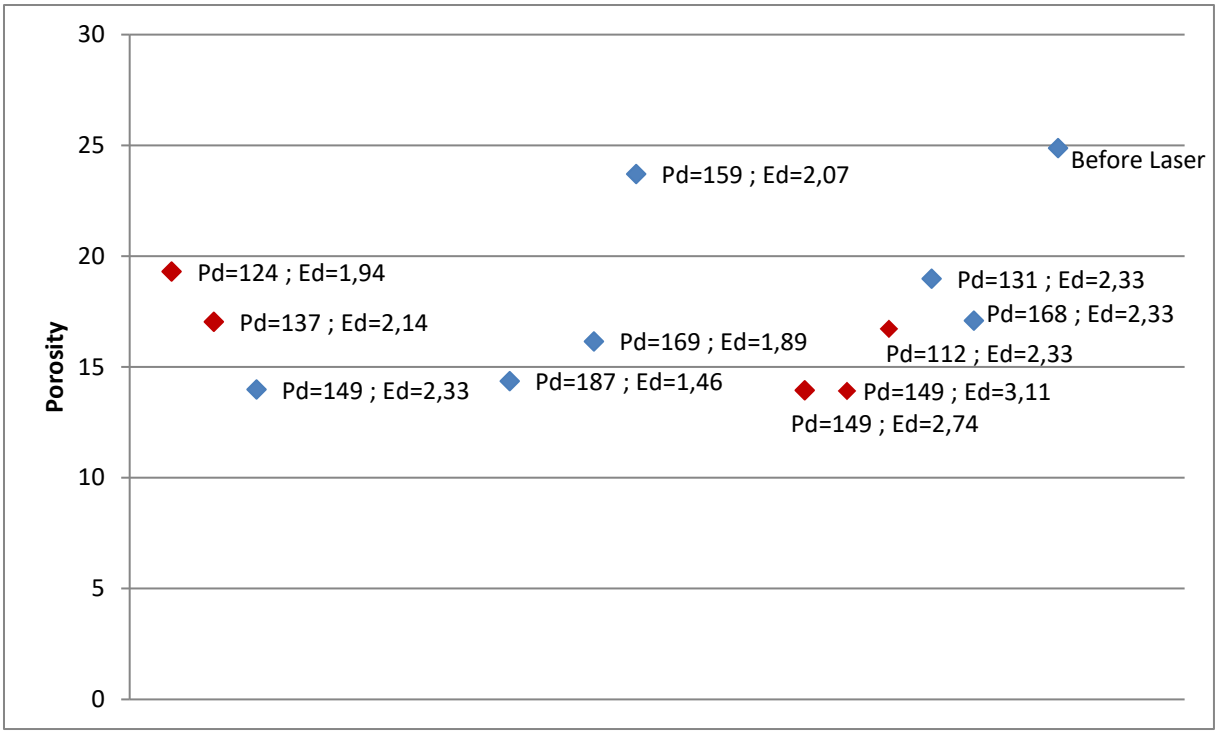

Figure 5-10 Porosity of various 2SLD coatings, with corresponding Pd and Ed.

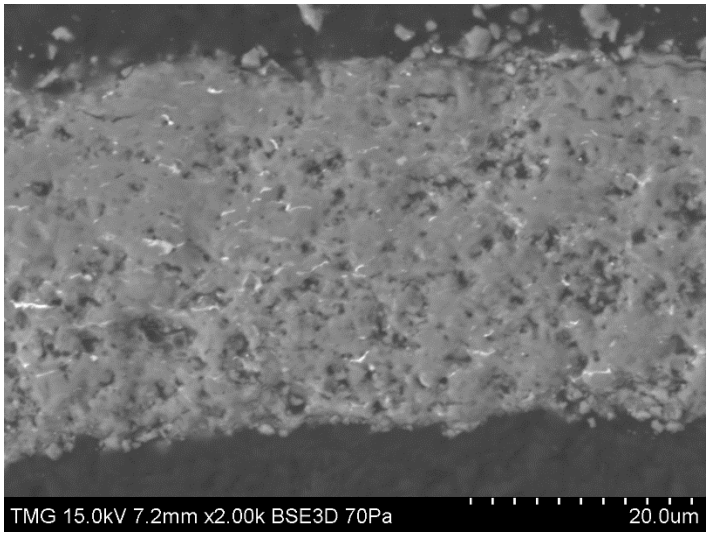

Figure 5-11 SEM cross-section micrograph of a 2SLD coating, exhibiting local change in microstructure related to laser-induced densification.

5.2. Conclusion

In conclusion, in this chapter, a laser post-treatment was studied to be able to control the density of the coating and to assess the feasibility of 2SLD of TiB_2 coatings. Our conclusions are as follows:

- The process was developed to avoid catastrophic failure and showed some promising results. The window of energy and power density to remelt the coating while avoiding delamination is rather small, and the best results were obtained with the following parameters: robots speed of 250 mm/s, plasma power of 1200 W, to maintain a power density close to 150 kW/mm².
- The increase in density is significant and acieved with an easy-to-use process. However, the inhomogeneities in the original coating (in terms of roughness, for instance) are reflected in the densified layer. Also, the densification comes with cracks that must be controlled.
- As this is a preliminary line scan study, further research must be led by developing a pattern of 2SLD to fully remelt the entire coating without causing too much stress, which could lead to cracking. The influence of the spot size could also be assessed.

Chapter 6 Conclusions, Contributions, and Recommendations

6.1. Summary and general conclusions

The main objective of this work was to develop a titanium diboride coating by suspension plasma spray that would exhibit the desired properties for a wettable cathode in Hall-Héroult cells, thereby improving their energy efficiency and the industrial process of aluminum production. Despite being a research topic for over 60 years, the development of such cathodes has encountered many technical challenges, requiring further research if it is to be implemented at an industrial scale.

Suspension plasma spray with the use of a gas shroud was the technique proposed to overcome the issues encountered in the literature. Previous studies showed a significant in-flight oxidation of the titanium diboride particles when deposited by Atmospheric Plasma Spray. However, Vacuum Plasma Spray demonstrated promising results, but its scalability to large-scale industrial coating needs remained a concern. The plasma spray approach offered the advantage of operating under atmospheric conditions, scalability, and applicability to large surfaces.

The coatings generated using SPS to deposit an ethanol-based TiB_2 suspension demonstrated limited oxidation, which was further reduced with the use of an Argon gas shroud. The coatings exhibited a range of microstructures, from highly porous and columnar (cauliflower type) to dense microstructures. Extensive parametric studies were conducted to assess the influence of key parameters on the coating's microstructure, such as stand-off distance, plasma power, plasma gas composition, substrate temperature, suspension feed rate, and suspension load. However, obtaining dense TiB_2 proved challenging, primarily due to the low residence time of droplets in the plasma plume, which is the hottest part of the plasma, owing to the high melting point of 2970 °C and medium density of 4.52 g/cm^3 of titanium diboride. The dense coatings by themselves were prone to cracking due to the build-up of stresses, especially during cooldown after deposition. To overcome these mechanical fragilities, a multilayer approach was adopted. A limited oxidation would sometimes lead to a surface boron oxide layer, but it was done away with by dissolving it into hot water.

In the multilayer approach, a porous coating is first deposited, and then conditions are adjusted during deposition to obtain a denser coating on top. The porous layer acted as a stress-relieving mechanism, ensuring good mechanical cohesion of the coating, and preventing fractures. This multilayer approach proved successful, resulting in non-oxidized, mechanically stable, and dense TiB_2 using. The ability to control and tune porosity across the coating opens the door to obtaining thick, mechanically and chemically stable titanium diboride coatings suitable for use in electrolysis cells.

In addition to the structural properties, the wetting behaviour of the coatings by molten aluminum was also measured and analyzed. It was observed that when oxidation occurred during the coating process, molten aluminum had to first reduce the boron and titanium oxides before wetting the material properly. This slower wetting kinetic was observed for un-shrouded SPS coatings compared to shrouded ones. Moreover, when deposited on porous coatings, molten aluminum permeated the coating and formed species such as Al_4C_3 at the coating-substrate interface, leading to delamination. The YSZ contamination originating from the raw powder was also segregated upon the percolation of molten aluminum throughout the coating, creating YSZ-rich phases at the coating-substrate interface, which could be detrimental to the application. However, when deposited on dense coatings, such as the multi-layered ones, there was no penetration of molten aluminum into the coating. The contact angle for the coatings was significantly better than that on graphite, the material currently used in the industry, with contact angles below 10° for the coatings compared to over 70° for uncoated graphite.

Finally, a high-power laser was considered as an approach to remelt and densify the top layers of the coating. The window for properly remelting these layers without causing complete destruction of the coatings proved to be narrow, yet it remains a possibility, leading to even bulkier and denser coatings. The laser-treated coatings exhibited densification but also cracking.

In conclusion, the results presented in this work suggest that SPS TiB_2 coatings could be a highly efficient and less energy-consuming candidate for wettable cathodes in Hall-Héroult cells, offering a commercial alternative for coating solutions. This research has led to the filing of one patent and the publication of two scientific articles [144] and [158]. Recently published articles by other authors also show enthusiasm for plasma-sprayed TiB_2 coatings [162].

6.2. Recommendations for Future Work

To further develop the coatings obtained in this thesis, we recommend the following actions. The developed SPS titanium diboride coating has shown great promise as a candidate for wettable cathodes.

- Further development of the multilayer approach is essential to enhance the mechanical cohesion of the coating and its longevity as a cathode. By repeating the porous/dense alternance several times, it would be possible to obtain millimetre-thick coatings. Investigating related patents on titanium diboride wettable cathodes [163], this appears to be a requirement to address typical wear caused by the solubility of TiB_2 in the electrolyte,e which is in the range of 0.98 kg/m^2/year [164].

- Further analysis of the mechanical bonding between the coating and the substrate is crucial in estimating the main fracture mechanisms and, therefore, the viability of the coating's industrial use. Precisely evaluating the mechanical bonding between the layers of the coating and between the coating and its substrate will provide insights into the lifetime of these coatings.

- Evaluating the chemical stability of the developed material in situ, in contact with molten cryolite, is essential to assess its resistance to sodium penetration. This is a critical requirement for the use of the material as a wettable cathode, as sodium penetration is one of the main wear mechanisms leading to its deterioration.

- A mathematical model could be developed to predict the Aluminum penetration into the coating. Such an algorithm could take into account the number of pores and their distribution, the oxide content, the presence of cracks.

- The influence of the substrate's surface roughness, as demonstrated in this work, affects the coating's microstructure and its inhomogeneity. While grit-blasting was used in this study, it may be more suitable for steel than graphite due to graphite's soft nature. Therefore, considering softer substrate preparation techniques, such as chemical treatments or pattern-inducing lithography-like techniques could be beneficial to improve repeatability and substrate-coating cohesion.

- To develop 2SLD TiB_2 coatings, conducting a parametric study to vary the spot size, as well as developing a laser pattern to treat an entire surface, are necessary requirements.

In conclusion, through this thesis, significant progress has been made towards the development of titanium diboride coatings for wettable cathodes in Hall-Héroult cells. Nevertheless, further research and optimization are needed to fully exploit the potential of

these coatings for large-scale industrial applications. The results achieved so far hold promise and open avenues for continued research and innovation in the field of aluminium production and electrolysis cell technology.

Bibliography

[1] C. M. Hall, "Process of Reducing Aluminium from its Fluoride Salts by Electrolysis". USA Patent 400664, 02 04 1889.

[2] P. Héroult, "Procédé électrolytique pour la préparation de l'aluminium". France Patent 175711, 01 09 1886.

[3] Aluminium Association of Canada, "The Industry," [Online]. Available: https://aluminium.ca/en/industry. [Accessed 22 09 2021].

[4] Aluminium Association of Canada, "Portrait of the Canadian Primary Aluminium Industry," [Online]. Available: https://aluminium.ca/pdf/portrait_alu_cdn_en_17_08_21.pdf. [Accessed 22 09 2021].

[5] F. M. Mayer, "Availability of Bauxite Reserves," *Natural Resources Research,* vol. 13, no. 3, pp. 161-172, 2004.

[6] F. Habashi, "Extractive metallurgy of aluminum," in *Handbook of aluminum*, CRC Press, 2003, pp. 1-46.

[7] D. Richerson, "Aluminum industry," in *Opportunities for advanced ceramics to meet the needs of the industries of the fture*, US Office of Energy, 1998.

[8] W. Choqte and J. Green, "US energy requirements for aluminium production," in *Energy efficient manufacturing processes symposium*, San Diego, CA, TMS, 2003, pp. 99-113.

[9] J. Keniry, "The economics of inert anodes and wettable cathodes for aluminium reduction cells," *JOM,* vol. 53, pp. 43-47, 2001.

[10] International Aluminium Institute, "Aluminium Carbon Footprint - Technical Support Document," International Aluminium Institute, 2018.

[11] The Aluminum Association, "Aluminum: The Element of Sustainability," The Aluminum Association, 2011.

[12] IPCC, "Primary Aluminium Production," in *Guidelines for National Greenhouse gas inventories Vol.3 - Industrial Processes and product use*, 2006, pp. 443-458.

[13] N. Tyabji and W. Nelson, "The GNCS factsheets: Mitigating Emmisions from Aluminum," Global Network for Climate Solutions, 2011.

[14] E. Alsema, "A database of energy reduction options for the Netherlands, 1995-2020 - Sector study for the Non-Ferrous Metals Industry," Utrecht, 2000.

[15] T. Beck and e. al., "Metal anode performance in low-temeprature electrolytes for aluminum production," *Metall. Mat. Trans. B,* vol. 42, p. 807, 2011.

[16] R. Pawlek, Inert Anode for Aluminium Electrolysis, Dussledorf: Aluminium-Verlag, 2007.

[17] S. Mohammadkhani, V. Jalilvand, B. Davis, F. Ben Ettouil, A. Dolatabadi, L. Roué, C. Moreau and D. Guay, "Suspension plasma spray deposition of CoxNi1-xO coatings," *Surface and Coatings Technology,* vol. 399, 2020.

[18] S. Mohammadkhani, V. Jalilvand, B. Davis, G. Gauthier, A. Dolatabadi, C. Moreau, L. Roué and D. Guay, "High-temperature behaviour of HVOF (Co,Ni)O coated Cu-Ni-Fe anodes," *Corrosion Science,* vol. 189, 2021.

[19] Alcoa, " ELYSIS - Start of Construction of Commercial-Scale Inert Anode Cells," Alcoa corporation, 29 June 2021. [Online]. Available: https://news.alcoa.com/media-center/alcoa-in-the-headlines/alcoa-in-the-headlines-details/2021/ELYSIS-Additional-20-million-in-federal-funding/default.aspx. [Accessed 14 February 2022].

[20] A. Svendsen, "Elysis moves toward commercialization of inert anodes," *Light Metal Age,* pp. 32-33, 2022.

[21] I. Galasiu and R. Galasiu, "Aluminium Electrolysis with Inert Anodes and Wettable Cathodes and with Low Energy Consumption," in *Molten Salts Chemistry and Technology*, John Wiley & Sons, Ltd., 2014, pp. 27-37.

[22] G. Strahs, "Ultrahigh-efficiency aluminum production cells," US Department of Energy, Argonne, 2011.

[23] H. A. Oye and B. J. Welch, "Cathode Performance: The Influence of Design, Operations, and Operating Conditions," *JOM,* vol. 50, pp. 18-23, 1998.

[24] A. P. Ratvik, R. Mollaabbasi and H. Alamdari, "Aluminium production process : from Hall-Heroult to modern smelters," *ChemTexts,* vol. 8, no. 10, p. 19, 2022.

[25] The Aluminium Story, "The Aluminium Story," in *TMS2019*, San Antonio, 2019.

[26] D. Picard, W. Bouzemmi, B. Allard and M. Fafard, "Thermo-mechanical characterization of carbon cathode material used in aluminium electrolysis cells," in *Carbon'09 : The Annual world conference on carbon*, Biarritz, 2009.

[27] L. Rivoaland, "Development of a new type of cathode for Aluminium Electrolysis," International Committee for Study of Bauxite, Alumina & Aluminium, Québec, 2016.

[28] V. Y. Bazhin and A. Saitov, "Improvement of physical and performance characteristics of carbon graphite lining by lithium additives," *Refractories and Industrial Ceramics,* vol. 59, no. 1, pp. 48-53, 2018.

[29] M. B. Djurdevic, Z. Odanovic and J. Pavlovic-Krstic, "Melt quality control at aluminum casting plants," *Metallurgical and Materials Engineering (MJoM),* vol. 16, no. 1, pp. 63-76, 2010.

[30] J. Antille, R. Von Kaenel and L. Bugnion, "Hall-Héroult cell simulator : a tool for the operation and process control," in *Light Metals*, Springer, 2016, pp. 617-622.

[31] F. Habashi, "Extractive metallurgy of aluminum," in *Handbook of aluminium*, CRC Press, 2003, pp. 1-46.

[32] W. Choate and J. Green, "US energy requirements for aluminum production," in *Energy efficient manufacturing processes symposium TMS*, San Diego, 2003.

[33] B. J. Welch, "Aluminum Production paths in the new millenium," *JOM,* pp. 24-28, 1999.

[34] W. Herreman, C. Nore, J.-L. Guermond, L. Cappanera, N. Weber and G. Horstmann, "Metal pad roll instability in cylindrical reduction cells," *Journal of Fluid Mechanics,* vol. 878, pp. 598-646, 2019.

[35] W. Liu, D. Zhou and Z. Zhao, "Progress in Application of Energy-Saving Measures in Aluminum Reduction Cells," *JOM,* vol. 71, no. 7, pp. 2420-2429, 2019.

[36] T. Young, "An essay on the cohesion of fluids," *Philosophical Transactions of the Royal Society of London,* pp. 65-87, 1805.

[37] R. Wenzel, "Resistance of solid surfaces to wetting by water," *Industrial & Engineering Chemistry,* vol. 28, pp. 988-994, 1936.

[38] A. Cassie and S. Baxter, "Wettability of porous surfaces," *Transactions of the Faraday society,* vol. 40, pp. 546-551, 1944.

[39] M. Yan and Z. Fan, "Review of durability of materials in molten aluminium alloys," *Journal of Materials Science,* vol. 36, pp. 285-295, 2001.

[40] A. Yurkov, Refractories for aluminium : Electrolysis and the cast house, 2nd edition, 2017: Springer, Moscow.

[41] Y. Borisoglebskii, M. Vetyukov and M. Karimov, "[In Russian]," *Cvetnye Metally,* vol. 2, pp. 36-37, 1992.

[42] S. Devyqtkin and G. Kaptay, "Chemical and electrochemical behavior of titanium diboride in cryolite-alumina mlet and in molten aluminum," *Journal of Solid State Chemistry,* vol. 154, pp. 107-109, 2000.

[43] E. S. Gorlanov, "Development of inert cathode technology. Part 1. Titanium diboride-based compact products and adhesive pastes," *Mettalurgy and Materials Science,* vol.

23, no. 5, pp. 1007-1022, 2019.

[44] R. P. Pawlek, "Wettable Cathodes : an update," in *Light Metals*, John A. Johnson, 2010, pp. 1185-1190.

[45] J. Li, X.-j. Lü, Y.-q. Lai, Q.-y. Li and a. Y.-x. Liu, "Research Progress in TiB2 WettableCathode for Aluminum Reduction," *JOM,* pp. 32-37, 2008.

[46] K. Billehaug and H. Oye, "Inert cathodes for aluminum electrolysis in Hall-Héroult cells, Pt 1," *Aluminum,* vol. 56, pp. 642-648, 1980.

[47] R. G. Munro, "Material Properties of Titanium Diboride," *J. Res. Natl. Inst. Stand. Technol.,* vol. 105, pp. 709-720, 2000.

[48] D. Weirauch Jr, W. Krafick, G. Ackart and P. Ownby, "The wettability of titanium diboride by molten aluminium drops," in *Proceedings of the IV International Conference High Temperature Capillarity*, Sanremo, 2005.

[49] A. McLeod, J. Haggerty and D. Sadoway, "Electrical resistivity of monocrystalline and polycristalline TiB2," *Journal of American Ceramic Society,* vol. 67, no. 11, pp. 705-708, 1984.

[50] B. Basu, G. Raju and A. Suri, "Processing and propertis of monolithic TiB2 based materials," *International Materials Reviews,* vol. 51, no. 6, pp. 352-374, 2006.

[51] C. Subramanian, T. Murthy and A. Suri, "Synthesis and consolidation of titanium diboride," *International Journal of Refractory Metals & Hard Materials,* vol. 25, pp. 345-350, 2007.

[52] K. Efimova, G. Galevskiy and V. Rudneva, "Synthesis and properties of nanoscale titanium diboride," in *IOP Conf. Ser.: Mater. Sci. Eng.*, 2015.

[53] R. Ricceri and P. Matteazzi, "A fast and low-cost room temperature process for TiB2 formation by mechanosynthesis," *Materials Science and Engineering A,* vol. 379, pp. 341-346, 2004.

[54] Y. Hwang and J. K. Lee, "Preparation of TiB2 powders by mechanical alloying," *Materials Letters,* vol. 54, pp. 1-7, 2001.

[55] P. Fauchais and A. Vardelle, "Solution and Suspension Plasma Spraying of Nanostructure Coatings," in *Advanced Plama Spray Applications*, Dr. Hamid Jazi (Ed.), InTech, 2012, pp. 149-189.

[56] Hua Wei Material, "Preparation method of titanium diboride," Hua Wei Material, 29 March 2022. [Online]. Available: https://www.huaweimaterial.com/news/technical-articles/preparation-method-of-titanium-diboride.html. [Accessed 4 April 2022].

[57] C. Ransley, "Electrolytic cells for the production of aluminum". British 1959.

[58] H. Itoh, S. Naka, T. Matsudaira and H. Hamamoto, "Preparation of TiB2 sintered compacts by hot pressing," *Journal of Materials Science,* vol. 25, pp. 533-536, 1990.

[59] T. Cheng, "Microstructures and metastable phases produced in cold sintered blocks by mechanical alloying of NiAl-TiB2," *Journal of Materials Science,* vol. 31, pp. 4433-4442, 1996.

[60] C. Tallon and G. Franks, "Exploring inexpensive processing routes to prepare dense TiB2 components," *Advances in Applied Ceramics,* vol. 115, no. 7, pp. 403-411, 2016.

[61] M.-A. Einarsrud, E. Hagen, G. Pettersen and T. Grande, "Pressureless sintering of titanium diboride with nickel, nickel boride, and iron additives," *J. Am. Ceram. Soc.,* vol. 80, no. 12, pp. 3013-3020, 1997.

[62] C. McMinn, "Review of RHM cathode development," *Light Metals,* pp. 419-425, 1992.

[63] H. Zhang, V. Nora and J. Sekhar, "Non-carbon cathodes in the Hall-Heroult cells," in *Materials used in the Hall-Heroult cell for aluminium production*, San Diego, TMS, 1994, pp. 37-54.

[64] Z. Fang, X.-L. Wu, L.-B. Li and J. Zhu, "Penetrative and migratory behavior of alkali metal in different binder based TiB2-C composite cathodes," *Transactions of Nonferrous metals society of China,* vol. 24, pp. 1220-1230, 2013.

[65] J. Li, X.-J. Lu, Q.-y. Li, Y.-q. Lai and J.-H. Yang, "Electrical resistivity of TiB2/C composit cathode coating for aluminium electrolysis," *CSUT,* vol. 13, no. 3, pp. 209-213, 2006.

[66] J. Xue and H. A. Oye, "Investigating Carbon/TiB2 materials for alinum reduction cathodes," *JOM,* vol. 44, pp. 28-34, 1992.

[67] M. Ibrahiem, T. Foosnaes and H. Oye, "Stability of TiB2-C composite coatings," *Light Metals,* pp. 691-696, 2006.

[68] S. Kang, D. Kim, E. Kang and S. Baek, "Pressureless sintering and properties of titanium diboride ceramics containing chromium and iron," *J Am Ceram Soc,* vol. 84, pp. 893-895, 2001.

[69] I. Azkona, F. Castro and J. Sanchez, "Abnormal growth of TiB2 crystals during sintering of TiB2-Ni3(Al,Ti) cemented borides," *Metall Mater Trans A,* vol. 36, pp. 459-466, 2005.

[70] S. Baik and P. Becher, "Effect of oxygen contamination on densification of TiB2," *J Am Ceram Soc,* vol. 70, pp. 527-530, 1987.

[71] S. Torizuka, K. Sato, H. Nishio and T. Kishi, "Effect of SiC on interfacial reaction and sintering mechanism of TiB2," *J Am Ceram Soc,* vol. 78, pp. 1606-1610, 1995.

[72] H. Heidari, "Development of wettable cathodes for aluminum smelting," PhD Thesis, 2012.

[73] A. Becker and J. Blanks, "TiB2-coated cathodes for aluminium smelting cells," *Thin solid films,* pp. 241-246, 1984.

[74] N. Rybakova, "Production of titanium diboride coatings by electrolysis of high temperature molten salts," PhD Thesis, 2011.

[75] D. Simakov, S. Vassiliev, P. Tursunov, N. Khasanova, V. Ivanov, A. Abakumov, A. Alekseeva, E. Antipov and G. Tsirlina, "Electrodeposition of TiB2 from Cryolite-Alumina melts," *Light Metals,* pp. 1019-1022, 2008.

[76] G. Brown, "Proceedings of the 6th australian aluminum smelting workshop," 1998.

[77] H. Oye, "Properties of colloidal alumina bonded TiB2 coating on carbon cathode materials," *Lighte Metals,* pp. 279-286, 1997.

[78] P. Fauchais, J. Heberlein and M. Boulos, Thermal spray fundamentals : from powder to part, New York: Springer, 2014.

[79] M. Oksa, E. Turunen, T. Suhonen, T. Varis and S.-P. Hannula, "Optimization and characterization of High velocity oxy-fuel sprayed coatings : techniques, materials, and applications," *Coatings,* vol. 1, no. 1, pp. 17-52, 2011.

[80] R. Vassen, A. Stuke and D. Stover, "Recent developments in the fields of thermal barrier coatings," *J. Therm. Spray Technol.,* vol. 18, pp. 181-186, 2009.

[81] R. Jaworski, L. Pawlowski, C. Pierlot, F. Roudet, S. Kozerski and F. Petit, "Recent developments in suspension plasma sprayed titanium oxide and hydroxyapatite coatings," *J. Therm. Spray technol.,* vol. 19, pp. 240-247, 2010.

[82] L. Pawlowski, The science and engineering of thermal spray coatings : Second edition, Chichester: John Wiley & Sons, 2008.

[83] L. Leblanc and C. Moreau, "The long-term stability of plasma spraying," *Journal of thermal spray technology,* vol. 11, pp. 380-386, 2002.

[84] D. Rigot, G. Delluc, B. Pateyron, J. Coudert, P. Fauchais and J. Wigren, "Transient evolution and shift of signals emitted by a d.c. plasma gun (type PTF4)," *J High Temp mater Process,* vol. 7, pp. 175-186, 2003.

[85] J. Davis, Handbook of Thermal Spray Technology, ASM International, 2004.

[86] C.-J. Li, H.-L. Liao, P. Gougeon, G. Montavon and C. Coddet, "Experimental

Correlation between Flattening Degree and Reynolds Number of Spray Particles," in *Thermal Spray 2003: Advancing the Science & Applying the Technology*, C. Moreau and B. Marple, Eds., Materials Park, Ohio: ASM International, 2003, pp. 863-869.

[87] P. Ruzhen, X. Gang, H. Yanqing, T. Lin and Y. Xiaohua, "Microstructure and Property of Plasma Sprayed TiB2 Wettable Coatings on Carbon Cathodes," *Advanced Materials Research,* vol. 881, pp. pp. 1580-1583, 2014.

[88] V. Ivanov, I. Blokhina and S. Kirik, "High-temperature oxidation kinetics of TiB2 powders in air," *Oxid Met,* vol. 82, pp. 71-84, 2014.

[89] J. Liu, B. Blanpain and P. Wollants, "A XPS Study of Atmospheric PLasma Sprayed TiB2 Coatings," *Key Engineering Materials,* Vols. 368-372, pp. 1347-1350, 2008.

[90] K. Seitz and F. Hiltmann, "Titanium diboride plasma coating of carbon cathode materials part I : coating process and microstructure," *Light Metals,* vol. 127, pp. pp. 379-383, 1998.

[91] F. Hiltmann and K. Seitz, "Titanium diboride plasma coating of carbon cathode materials part II : characterization," *Light Metals,* vol. 127, pp. pp.385-390, 1998.

[92] B. W. Callen, M. Gindrat, J. Liu and J. Rauch, "Suspension spraying - an emerging coating technology," Sulzer, 2013.

[93] R. Vassen, H. Kassner and D. Stöver, "Suspension plasma spraying: process characteristics and applications," *JTTEE5,* vol. 19, pp. 219-225, 2009.

[94] P. Fauchais, A. Joulia, S. Goutier, C. Chazelas, M. Vardelle, A. Vardelle and S. Rossignol, "Suspension and solution plasma spraying," *J. Phys. D, Appl. Phys.,* vol. 46, pp. 1-14, 2013.

[95] I. Choquet, S. Björklund, J. Johansson and J. Wigren, "Clogging and lump formation during atmospheric plasma spraying with powder injection downstream the plasma gun," *JTTEE5,* vol. 16, no. 4, pp. 512-523, 2007.

[96] H. Kassner, R. Siegert, D. Hathiramani, R. Vassen and D. Stoever, "Application of suspension plasma spraying (SPS) for manufacture of ceramic coatings," *J. Therm. Spray Technol.,* vol. 17, pp. 115-123, 2008.

[97] S. Zimmermann, G. Mauer, K.-H. Rauwald and J. Schein, "Characterization of an Axial-Injection Plasma Spray Torch," *J Therm Spray Tech,* vol. 30, pp. 1724-1736, 2021.

[98] J.-L. Marques, G. Forster and J. Schein, "Multi-electrode plasma torches: motivation for development and current state-of-the-art," *The Open Plasma Physics Journal,* vol. 2, pp. 89-98, 2009.

[99] D. R. Lide, CRC Handbook of Chemistry and Physics, 85th edition, Washington DC: CRC Press, 2004.

[100] U.S. Secretary of Commerce, NIST Chemistry WebBook, SRD 69, Washington DC: U.S. Secretary of Commerce, 2022.

[101] A. Farrokhpanah, T. W. Coyle and J. Mostaghimi, "Numerical study of Suspension Plasma Spraying," *J Therm Spray Tech,* vol. 26, pp. 12-36, 2017.

[102] N. Sharifi, "Developing superhydrophobic coatings for mitigating aircraft icing using plasma spray processes," Concordia University, Montreal, 2018.

[103] S. Matthews, "Shrouded plasma spray of Ni-20Cr coatings utilizing internal shroud film cooling," *Surface & Coatings technology,* vol. 249, pp. 56-74, 2014.

[104] S. Kim, S. Choi, H. Han, G.-H. Kim and S.-H. Hong, "Shroud gas effects on thermal diffusivity of plasma spray coated tungsten for plasma facing components in fusion reactors," in *ISPC*, 2010.

[105] Q. Wei, Z. Yin and H. Li, "Oxidation control in plasma spraying NiCrCoAlY coating," *Applied Surface Science,* vol. 258, pp. 5094-5099, 2012.

[106] H. Zhou, C. Peng, Z. Liu, M. Al-Rawi and J. Kanna, "Titanium coatings plasma sprayed with/without a shroud," in *IOP Conf. Series; Materrials Science and Engineering*, 2020.

[107] W. Qi, Y. Zhiyong and L. Hui, "Oxidation control in plasma spraying NiCrCoAlY coating," *Applied surface science,* vol. 258, pp. 5094-5099, 2012.

[108] K. Sungwoo, C. Sooseok, H. Hyunsu, K. Gon-Ho and H. Sang Hee, "Shroud Gas effects on thermal diffusivity of plasma spray coated tungsten for plasma facing components in fusion reactors," Department of nuclear energy, Seoul, 2007.

[109] M. Planche, H. Liao and C. Coddet, "Oxidation control in atmospheric plasma spraying coating," *Surface & Coatings Technology,* vol. 202, pp. 69-76, 2007.

[110] S. Matthews, "Compositional development as a Function of spray distance in unshrouded/shrouded plasma-sprayed Cr3C2-NiCr coatings," *JTTEEE5,* vol. 24, no. 3, pp. 515-533, 2014.

[111] H. Tsai and P. Tsai, "Performance of laser-glazed plasma-sprayed (ZrO2-12wt% Y2O3)/(Ni-22wt% Cr-10wt% Al-1wt%Y) thermal barrier coatings in cyclic oxidation tests," *Surf. Coat. Technol.,* Vols. 53-59, p. 71, 1995.

[112] L. Pawlowski, H. Rapinel, F. Tourenne and M. Jeandin, "Traitement laser des depots plasma d'hydroxyapatite," *Galv. Org. Traite. Surf.,* vol. 676, pp. 433-437, 1997.

[113] S. Tondu, T. Schnick, L. Pawlowski, B. Wielage, S. Steinhauser and L. Sabatier, "Laser glazing of FeCr-TiC composite coatings," *Surf. Coat. Technol.,* vol. 123, pp. 247-251,

1998.

[114] B. Wielage, S. Steinhauser, L. Pawlowski, I. Smurov and L. Covelli, "Laser treatment of vacuum plasma sprayed CoCrAlY alloy," in *Surface modification technologies*, London, UK, The Institute of Materials, 1998, pp. 687-698.

[115] H. Ingham, "Flame spraying employing laser heating". US Patent 3310423, 1967.

[116] J. Ayers and R. Schaefer, "Consolidation of plasma sprayed coatings by laser remelting," *Proc. SPIE,* vol. 198, pp. 57-64, 1979.

[117] D. Das, "Surface roughness created by laser surface alloying of aluminium with nickel," *Surf. Coat. Technol.,* vol. 64, pp. 11-15, 1994.

[118] T. Troczynski, L. Pawlowski, N. Third, L. Covelli and I. Smurov, "Physico-chemical treatment of zirconia coatings for thermal barriers," in *International Thermal Spray Conference*, Nice, 1998.

[119] W. Aihua, Z. Beidi, T. Zengyi, M. Xianyao, D. Shijun and C. Xudong, "Thermal-shock behaviour of plasma sprayed Al2O3+13wt%TiO2 coatings on Al-Si alloy influenced by laser remelting," *Surf. Coat. Technol.,* vol. 37, pp. 169-172, 1993.

[120] K. Jasim, R. Rawlings and D. West, "Characterization of plasma-sprayed layers of fully yttria-stabilized zirconia by laser sealing," *Surf. Coat. Technol.,* vol. 53, pp. 75-86, 1992.

[121] A. Ganvir, "Microstructure and thermal conductivity of liquid feedstock plasma sprayed thermal barrier coatings," University West Bachelor Thesis, Sweden, 2016.

[122] A. Killinger, R. Gadow, G. Mauer, A. Guignard, R. Vassen and D. Stover, "Review of new developments in suspension and solution precursor thermal spray processes," *J. Therm. Spray Technol.,* vol. 20, p. 677, 2011.

[123] A. Akbarnozari, "Diagnostic methods and parameters to characterize droplets and particles in Suspension Plasma Spray," Concordia University, Montreal, 2019.

[124] S. Mohammadkhani, S. Jalilvand, B. Davis, F. Ben Ettouil, A. Dolatabadi, L. Roue, C. Moreau and D. Guay, "Suspension plasma spray deposition of CoxNi1-xO coatings," *Surface and Coatings Technology,* vol. 399, pp. 162-168, 2020.

[125] T. Marrocco, T. Hussain, M. D.G. and P. Shipway, "Corrosion performance of laser post-treated cold sprayed titanium coatings," *Journal of Thermal Spray Technology,* vol. 20, no. 4, pp. 909-917, 2011.

[126] Z. Taha-al, M. Hashmi and B. Yilbas, "Laser treatment of HVOF coating: model study and characterization," *Journal of Mechanical Science and Technology,* vol. 21, pp. 1439-1444, 2007.

[127] V. Biryukov, "Laser modification of the properties of Boride coatings," *Russian Engineering Research,* vol. 32, no. 1, pp. 58-60, 2012.

[128] P. Fauchais, M. Vardelle, S. Goutier and A. Vardelle, "Key challenges and opportunities in Suspension and Solution Plasma Spraying," *Plasma Chem. Plasma Process,* vol. 35, pp. 511-525, 2015.

[129] P. Fauchais, M. Vardelle, A. Vardelle and S. Goutier, "What do we know, what are the current limitations of suspension plasma spraying?," *J. Therm. Spray Technol.,* pp. 1-10, 2015.

[130] Tecnar Automation Ltd, "Accuraspray - One sensor for all processes - Tecnar spray sensors," Tecnar Automation Ltd, 07 October 2020. [Online]. Available: https://spraysensors.tecnar.com/thermal-spray/accuraspray-4-0/. [Accessed 15 March 2022].

[131] J. Berlin, "Analysis of Boron with energy dispersive X-ray spectrometry : advances in light element analysis with SDD technology," *Imaging and Microscopy,* vol. 13, pp. 19-21, 2011.

[132] H. Cheng, Z. Li and Y. Shi, "Microstucture and wear resistance of Al2O3-TiB2 composite coating deposited by axial plasma spraying," *Surface Engineering,* vol. 24, no. 6, pp. 452-457, 2008.

[133] P. Ananthapadmanabhan, K. Sreekumar, P. Ravindran and N. Venkatramani, "Electrical resistivity of plasma-sprayed titanium diboride coatings," *Journal of Materials Science,* vol. 28, pp. 1655-1658, 1993.

[134] F. Tarasi, M. Medraj, A. Dolatabadi, J. Oberste Berghaus and C. Moreau, "Effective parameters in axial injection suspension plasma spray process of alumina-zirconia ceramics," in *ITSC2008*, Maastricht, 2008.

[135] T. Tesar, R. Musalek, J. Medricky and J. Cizek, "On growth of suspension plasma-sprayed coatings deposited by high-enthalpy plasma torch," *Surface & Coatings Technology,* vol. 371, pp. 333-343, 2019.

[136] T. Ru, "Spray parameters influence on suspension plasma sprayed zirconia coatings properties," University West, Trollhättan, 2014.

[137] P. Fauchais, M. Vardelle and A. Vardelle, "Reliability of plasma-sprayed coatings: monitoring the plasma-sprayed process and improving the quality of coatings," *J. Phys. D: Appl/ Phys.,* vol. 46, p. 16p, 2013.

[138] Y. Wang, J.-G. Legoux, R. Neagu and S. Hui, "Suspension Plasma Spray and Performance Characterization of Half Cells with NiO/YSZ Anode and YSZ electrolyte," *Journal of Thermal Spray Technology,* vol. 21, no. 1, pp. 7-15, 2012.

[139] R. C. Seshadri, G. Dwivedi, V. Viswanathan and S. Sampath, "Characterizing suspension plasma spray coating formation dynamics through curvature measurements," *Journal of Thermal Spray Technology,* vol. 25, pp. 1666-1683, 2016.

[140] P. Fauchais and A. Vardelle, "Solution and suspension plasma spraying of nanostructure coatings," in *Advanced plasma spray applications*, Limoges, InTech, 2012, pp. 149-188.

[141] W. Fan and Y. Bai, "Review of suspension and solution precursor plasma sprayed thermal barrier coatings," *Ceramics International,* vol. 42, no. 13, pp. 14299-14312, 2016.

[142] B. Bernard, A. Quet, L. Bianchi, A. Joulia, A. Malié, V. Schick and B. Rémy, "Thermal insulation properties of YSZ coatings: suspension plasma spraying (SPS) versus electron beam physcial vapor deposition (EB-PVD)," *Surf. Coat. Technol.,* vol. 318, pp. 122-128, 2017.

[143] S. Croll, "Surface roughness profile and its effect on coating adhesion and corrosion protection: a review," *Progress in Organic coatings,* vol. 148, 2020.

[144] E. Yvenou, A. Bily, F. Ben Ettouil, A. Dolatabadi, B. Davis, D. Guay, C. Moreau and L. Roue, "TiB2 deposited on graphite by Suspension Plasma Spray as Al wettable cathode," *J Therm Spray Tech,* vol. 30, pp. 1535-1543, 2021.

[145] R. Telle, L. Sigl and K. Takagi, "Boride-based hard materials," in *Handbook of Ceramic Hard Materials, vol.2*, Weinheim, Wiley, 2000.

[146] K. Juhasz, P. Baumli, J. Sytchev and G. Kaptay, "Wettability of graphite by liquid aluminium under molten potassium halide fluxes," *Journal of Materials Science,* vol. 48, pp. 7679-7685, 2013.

[147] H. Heidari, H. Alamdari, D. Dube and R. Schulz, "Interaction of Molten Aluminum with Porous TiB2-based Ceramics Containing Ti-Fe additives," *J. Eur. Ceram. Soc.,* vol. 32, pp. 937-945, 2012.

[148] T. Etter, P. Schulz, M. Weber, J. Metz, M. Wimmler, J. Loffler and P. Uggowitzer, "Aluminium Carbide formation in interpentrating graphite/aluminium composites," *Mater. Sci. Eng. A.,* vol. 448, no. 1, pp. 1-6, 2007.

[149] T. Wang, Z. Jin and J. Zhao, "Thermodynamic assessment of the Al-Zr binary system," *J. Phase Equilibria,* vol. 22, pp. 544-551, 2001.

[150] C. Yan, R. Liu, C. Zhang, Y. Cao and X. Long, "Synthesis and formation mechanism of Zrb2-Al2O3 composite powder starting from ZrO2, Al, and BN," *Adv. Powder Technol.,* vol. 27, pp. 711-716, 2016.

[151] N. Sobczak, N. Gupta and W. Hunt, "Interaction between molten aluminum and

oxides," in *Solidification processing of metal matrix composites*, Rohatgi, 2006.

[152] T. Parthasarathy, R. Rapp, M. Opeka and R. Kerans, "A model for the oxidation of ZrB2, HfB2 and TiB2," *Acta Materialia,* vol. 55, pp. 5999-6010, 2007.

[153] V. Lavrenko and A. Alexeev, "High-temperature oxidation of boron nitride," *Ceramics International,* vol. 12, no. 1, pp. 25-31, 1986.

[154] V. Kochkodan, N. Bin Darwish and N. Hilal, "The chemistry of boron in water," in *Boron Separation Processes*, Swansea, Elsevier, 2015, p. 31.

[155] M. Boulos, P. Fauchais and E. Pfender, Thermal Plasmas: Fundamental and Applications, New York, USA: Plenum Press, 1994.

[156] C. M. Efaw, B. Lu, Y. Lin, G. M. Pawar, P. R. Chinnam, M. F. Hurley, E. J. Dufek, Y. S. Meng and B. Li, "A closed-host bi-layer dense/porous solid electrolyte interphase for enhanced lithium-metal anode stability," *MaterialsToday,* vol. 49, pp. 48-58, 2021.

[157] S. Y. Kim and J. Li, "Porous Mixed Ionic Electronic Conductor Interlayers for Solid-State Batteries," *Energy Material Advances,* vol. 2021, p. 15, 2021.

[158] S. Mohammadkheni, A. Bily, B. Davis, A. Dolatabadi, C. Moreau, L. Rouée and D. Guay, "Impact of density on the behavior of suspension plasma-sprayed TiB2 coatings in the presence of molten aluminum," *Journal of Thermal Spray Technology,* vol. 31, pp. 1499-1507, 2022.

[159] H. Chen, E. Pfender and J. Heberlein, "Improvement of plasma spraying efficiency and coating quality," *Plasma Chemistry and Plasma Processing,* vol. 17, pp. 93-105, 1997.

[160] C. Osarinmwian, A. Dutton and J. Osarinmwian, "Commercializing metal production in the modern era," Manchester, 2014.

[161] S. Aouadi, S. Rodhe and F. Namavar, "Characterization of Ti-based nanocrystalline ternary nitride films," *Journal of vacuum science and technology B,* vol. 20, no. 5, pp. 1967-1973, 2002.

[162] B. Yang, R. Peng, D. Zhao, N. Yang, Y. Hou and X. Gang, "Performance of TiB2 Wettable Cathode Coating," *Minerals,* vol. 12, no. 27, p. 11p, 2022.

[163] D. A. Weirauch, L. M. Sworts, B. J. Tielsch and R. A. DiMilia, "Composition for making wettable cathode in aluminum smelting". US Patent 20190055660A1, 28 07 2009.

[164] H. Oye, V. De Nora, J. Duruz and G. Johnson, "Aluminum reduction cell qnd system for energy - TiB2 coating on cathode carbon materials," *Light Metals,* pp. 279-286, 1997.

[165] E. H. Jordan, C. Jiang and M. Gell, "The solution precursor plasma spray (SPPS) process : a review with energy considerations," *Journal of Thermal Spray Technology,* vol. 24, pp. 1153-1165, 2015.

[166] D. Richerson, "Aluminium industry," in *Opportunities for advanced ceramics to meet the needs of the industries of the future*, US Office of Energy, 1998.